UNIVERSIDAD EAFIT

THESIS OF MASTER IN SCIENCE

COMPENDIUM OF PUBLICATIONS ON:

Computational Geometry and Numerical Simulation in Applications of Computational Mechanics

Master Student

Diego Alejandro Montoya Zapata

Supervisor

Prof. Dr. Ing. Oscar E. Ruiz Salguero

Laboratory of CAD CAM CAE

Universidad EAFIT

Dissertation

Submitted in partial fulfillment of the requirements for the degree of Master of Engineering in the College of Engineering of Universidad EAFIT

UNIVERSIDAD EAFIT
COLLEGE OF ENGINEERING
MASTER PROGRAM IN ENGINEERING
MEDELLIN, COLOMBIA
OCTOBER 2018

Dedication

To my family.

Acknowledgments

To my parents, my brother, and my girlfriend: your love, your sacrifices, and your support have guided me here.

I want to express my gratitude to my advisor Prof. Dr. Ing. Oscar Ruiz Salguero for his constant attention, compromise, and effort. His invaluable recommendations have made me not only a better engineer, but a better human being.

I am grateful to Dr. Jorge Posada, Dr. Iñigo Barandiaran, and Dr. Aitor Moreno for trusting and supporting me during my internship in Vicomtech.

I am sincerely thankful to Universidad EAFIT and Vicomtech for helping and providing the funding for my research and my studies.

I would like to acknowledge Dr. Camilo Cortés for his advices when I joined Laboratory of CAD CAM CAE. I still can remember some of your very valuable words.

I am also grateful to the whole team of Laboratory of CAD CAM CAE. Thank you for your help, your jokes... and for those unforgettable football matches. Hope you have not improved.

Finally, I want to thank our Colombian athletes, specially our cyclists. That strong way in which you stand up after falling down simply inspire me.

Contents

List of Figures

ix

x

List of Tables

Chapter 1

Introduction

Computational modeling and mechanical characterization of porous and lattice materials, and topology optimization for 3D printing are topics that attract the attention of academicians and industrialists. Design, manufacturing, medicine, biomedicine, automotive and aerospace industries are contexts in which the research on these topics is of special relevance.

The estimation of the mechanical properties (e.g. Young's modulus, Poisson's ratio) of porous and lattice materials is important for their applications as impact absorbers in the automotive and aerospace industries. However, (1) material tests are expensive, and (2) numerical simulations are intractable due to the large size of the computational representations. Therefore, the development of effective and efficient methods to estimate the mechanical properties of porous material is still an open research matter.

Additive manufacturing (or 3D printing) is revolutionizing the world of manufacturing. The materials, design techniques and software, simulation and data acquisition methods, and the manufacturing process by itself are being affected by the use of 3D printing technologies. The almost free-form design and material savings are two of the main advantages of additive manufacturing. Therefore, the use of topology optimization algorithms to find the optimum relation between material expenses and structural functionality is gaining more importance. However, current topology optimization algorithms are still very limited for the manufacturing constraints related to subtractive methods. Hence, the improvement of these algorithms is mandatory for the establishment of 3D printing at an industrial scale.

This work presents a compilation of different contributions to the problems stated in this introduction. Subsequent Sections 1.1 and 1.2 summarize the articles included in this compendium and list all the co-authors associated to each publication. Finally, Section 1.3 explains to the reader how to follow this document.

1.1 Summary of Publications

Two conference publications, a chapter in book and two articles submitted to relevant international journals are the results of the research executed during the course of the Master in Engineering

at Universidad EAFIT. In Table 1.1 are listed the published and submitted articles with their respective authorship and bibliographic information.

Table 1.1: List of published and submitted articles.

Item	Bibliographic Information	Type / Status
1	Diego Montoya-Zapata, Oscar Ruiz-Salguero, Juan Lalinde-Pulido, Juan Pareja-Corcho, and Jorge Posada. (2018). *Non-manifold modelling of lattice materials using kinematically constrained FEA*. Proceedings of the 12th International Symposium on Tools and Methods of Competitive Engineering (TMCE 2018). ISBN: 978-94-6186-910-4. Las Palmas de Gran Canaria, Spain, May 7-11, 2018.	Conference Article / Published
2	Juan M. Munoz, Oscar Ruiz-Salguero, Diego Montoya-Zapata, Camilo Cortés, and Carlos Cadavid. *Direct Scalar Field - to - Truss Representation and Stress Simulation of Open Pore Domains*. Accepted to the Conference Smart Tools and Applications in Graphics (STAG 2018), Brescia, Italy, October 18–19, 2018.	Conference Article / Accepted
3	Diego Montoya-Zapata, Diego A. Acosta, Oscar Ruiz-Salguero, and David Sanchez-Londono. (2018). *FEA Structural Optimization Based on Metagraphs*. International Joint Conference SOCO'18-CISIS'18-ICEUTE'18. Print ISBN 978-3-319-94119-6 , Online ISBN 978-3-319-94120-2, pp 209-220, vol. 771. DOI: https://doi.org/10.1007/978-3-319-94120-2_20 Book Series: Advances in Intelligent Systems and Computing. Springer International Publishing AG, part of Springer Nature 2019.	Chapter in Book / Published
4	Diego Montoya-Zapata, Diego A. Acosta, Oscar Ruiz-Salguero, Jorge Posada, and David Sanchez-Londono. (2018). *FEA Structural Optimization Based on Metagraphs*. Submitted to Journal Cybernetics and Systems. Print ISSN: 0196-9722. Online ISSN: 1087-6553. Publisher: Taylor & Francis. Indexed in Scopus: Q3, ISI (Web of Science): Q3, Publindex: B.	Journal Article / Submitted
5	Diego Montoya-Zapata, Camilo Cortés, and Oscar Ruiz-Salguero. *FE-Simulations with a Simplified Model for Open-Cell Porous Materials: A Kelvin Cell Approach*. Submitted to Journal of Computational Methods in Sciences and Engineering. Print ISSN: 1472-7978. Online ISSN: 1875-8983. Publisher: IOS Press. Indexed in Scopus: Q3, Publindex: B.	Journal Article / 2nd Round Revision

1.2 List of Co-authors of this Compendium of Publications

The names and affiliations of the co-author of the articles presented in this compendium are listed in Table 1.2.

Table 1.2: Co-authors of this compendium of publications.

Name	Affiliation
Diego Andrés Acosta Maya	Process Development and Design Research Group (DDP), Universidad EAFIT, Colombia
Carlos Cadavid Moreno	Functional Analysis Group, Universidad EAFIT, Colombia
Camilo Cortés Acosta	eHealth and Biomedical Applications, Vicomtech, Spain
Juan Guillermo Lalinde Pulido	High Performance Computing Facility APOLO, Universidad EAFIT, Colombia
Diego Alejandro Montoya Zapata	Laboratory of CAD CAM CAE, Universidad EAFIT, Colombia Industry and Advanced Manufacturing, Vicomtech, Spain
Juan Manuel Muñoz Betancur	Laboratory of CAD CAM CAE, Universidad EAFIT, Colombia
Juan Pareja Corcho	Laboratory of CAD CAM CAE, Universidad EAFIT, Colombia
Jorge Posada	Vicomtech, Spain
Oscar Ruiz Salguero	Laboratory of CAD CAM CAE, Universidad EAFIT, Colombia
David Sánchez Londoño	Laboratory of CAD CAM CAE, Universidad EAFIT, Colombia

1.3 How to Read this Document

This document presents the developments of a research executed at the Laboratory of CAD CAM CAE at Universidad EAFIT (Colombia), and Vicomtech (Spain). The obtained results are a combination of computational geometry, data structures and algorithms, and mathematics. Numerical simulation plays an important role to test the accuracy and to evaluate the impact of the developed approaches.

All the articles included in this compendium have been submitted to peer-reviewed journals or conferences. Chapter 2 shows the observations of the Referees with the corresponding responses given by the authors. As stated previously, the article *A General Meta-graph Strategy for Shape Evolution under Mechanical Stress* has only been submitted and the first communication from the Editors of the journal is still pending.

Chapter 3 presents a work-flow to model and simulate efficiently large 2.5D lattice domains. To ease the study of these 2.5D lattice domain, a data structure to support non-2-manifold topology is developed and kinematic constraints are added into the executed FEA analyses.

Chapter 4 proposes an alternative to model open-cell porous materials in which the 1.5D representation of the porous domain is directly obtained from the voxel scalar field of the Computer Tomography of the domain, thus avoiding the explicit calculation of the domain boundary. Shear

and tension numerical simulations, conducted on the obtained 1.5D model, show the suitability of the approach to characterize open-cell porous domains.

Chapter 5 proposes a topology optimization algorithm that is based on the representation of FEA meshes as mathematical graphs. The presented algorithm uses a meta-graph based technique integrated into the Evolutionary Structural Optimization algorithm. By considering this meta-graph connectivity approach, the optimization process is not interrupted by disconnections generated during the material removal stage.

Chapter 6 presents a truss-based approach to model and simulate efficiently open-cell porous materials. Estimations of macro-mechanical properties (Young's modulus and Poisson's ratio) are used to show the suitability of the truss-based approach to analyze large and complex porous domains.

Finally, relevant conclusions of this work as well as possible future improvements on this research are presented in Chapter 7.

Chapter 2

Response to Reviewers' Observations

In this chapter are presented the responses given to the Reviewers' observations that have arisen from the Revision Stages of the corresponding Peer Review Process that each article of this Compendium has followed.

2.1 Non-Manifold Modelling of Lattice Materials using Kinematically Constrained FEA

2.1.1 Responses to Referee 1

Table 2.1: Responses to Reviewers' observations of article "Non-Manifold Modelling of Lattice Materials using Kinematically Constrained FEA".

Item	Observation	Actions Taken
1	Is there any limitation of modelling shapes of arbitrary geometric shape (morphological characteristic) with Kelvin cells?	We have addressed the observation of the Reviewer. In Section 3.3 (above Fig. 7) the following paragraph was inserted: "Notice that small details of the Elephant (e.g. ear and body creases) disappear in the modelling process. Kelvin cells convey a sampling of the original shape. Therefore, high frequency features disappear, representing a limitation of the shapes modelled by Kelvin cells"

2	How the approach was validated beyond error analysis?	To abide the Reviewer's observation we have added along the manuscript text to express the need to validate our approach with laboratory experiments. We performed the following actions: 1) At the end of the Abstract, we modified the text that refers to the Future Work. We included this text: "Future research may be addressed in contrasting the numerical results with real laboratory tests." 2) We inserted in Section 5 (Conclusions and Future Work) the following text: "Future research is required in contrasting the results presented in this manuscript with laboratory experiments." 3) We added a new Section (4.3 Advantages and Disadvantages) in which the need for physical experimental verification of our approach is expressed.
3	The advantages and the shortcomings of the proposed approach should be made more explicit in Section 4 of the paper. How about computation itself?	In order to fulfil the Reviewer's requirement we have: 1) At the beginning of Section 4.1 Comparison of the 2.5D FACEs and 3D B-Rep models, we added a discussion about the computational advantages of the 2.5D model in comparison to the 3D model. 2) Added a new header in Section 4 (4.3 Advantages and Disadvantages).
4	In the Abstract overuse of dashes should be reduced, for instance in "In silico simulations of non trivial 3D slender shapes do not terminate, usually not passing the 3D meshing stage. Slender plates can be practically finite - element analysed with 2D FACE plus thickness elements, but such 2D elements accept no Boolean union as they produce non manifold situations".	The Reviewer is right. We have supressed the unnecessary dashes from the Abstract. We highlighted in the Abstract the words from which we removed the dashes.
5	The image and caption of Figure 1 are separated by part of the running text. Please correct.	We have addressed the observation of the Reviewer. In the original version, the captions (a) and (b) were too close, giving the impression of intruding running text. We have corrected them by adding horizontal space between the two subfigures.
6	Table captions should be placed above the tables.	We have addressed the observation of the Reviewer. All the captions of the tables have been placed above.

7	Continuity of text in 2.3 should be checked.	We have corrected this typo error. In Section 2.3, a spurious line break was supressed.
8	Width of Table 5 should be adjusted to page margins.	Table 5 has been adjusted according to the TMCE 2018 template.
9	Figures 13 and 14 are to be inserted to where they are referred to in the text.	We have moved Figures 13 and 14 to Section 4, as per the Referee's request.
10	Footer inserts should be adjusted (cut back) to single line.	1) In author footer inserts, we removed the duplication of the name "Oscar Ruiz-Salguero". 2) In title footer inserts, this observation implies changing the manuscript title. We thus refer to the Proceedings Editor to guide us in the correct protocol to change the manuscript title (or authorise us to locally shorten it in the footer).

2.2 Direct Scalar Field - to - Truss Representation and Stress Simulation of Open Pore Domains

2.2.1 Responses to Referee 1

The contribution is focused on providing simplified geometric representations for real (non-simulated) porous materials that could be suitable for finite element analysis. In particular a quite simple direct conversion from CT scans to a truss graph representation, related to medial axis skeleton extraction. Actually the results provided by the proposed technique are limited to 1D skeleton representations not supporting surface medial axis portions of the simplified material representation, as authors acknowledge.

Table 2.2: Responses to the observations of Referee 1 of article "Direct Scalar Field - to - Truss Representation and Stress Simulation of Open Pore Domains".

Item	Observation	Actions Taken
1	I found the proposed simplification quite simple and seemingly mostly based on ref [JST16]. Please better justify the difference between the proposed medial axis extraction and [JST16].	We thank the Referee for the valuable comment. To abide by the Referee's observation, we have made multiple changes to the manuscript to justify the difference between our approach and the one in [JST16]: (1) We have added the following text in the final paragraph of Sec. 2.1: "However, the mass of the whole domain cannot be retrieved from the final skeleton." (2) In Sec. 2.3 we have added the item 2(c): "Our algorithm avoids possible disconnections in the curve skeletons that may occur in [JST16]". (3) We have modified the second paragraph of Sec. 3.1. The modified piece now reads: "This is an important difference with previous methods (e.g. [JST16]), where 1-manifold wires are considered only if they have received a large amount of mass from the boundary voxels."
2	Once medial axis representation is extracted its simplification involves very simple operations that are however too coarsely described (e.g. are there parameters to be set by the user? which ones?).	We thank the Referee for the valuable comment. To address the observation of the Referee, we have specified in Sec. 3.2 two parameters (L, P) that must be set by the user.

3	I found many similarities in terms of addressed problem and proposed solutions with ref [COU*18] with the exception of the direct derivation of the truss graph from 3D scalar fields (voxel representation from CT scan) instead of passing for BRep description. This is good but unfortunately no comparison has been provided to show that this shortcut is still able to guarantee good approximations for the intended usages (FEA). I think this is the main problem with this work and I would see possible acceptance of this contribution as subject to some quantitative results that actually demonstrate if not the equivalence, at least the fact that not having to compute Bref representation to extract the truss graph entail a reasonable performance degradation tradeoff.	We thank the Referee for the valuable comment. To address this observation we have: (1) Improved the shear simulation, so that the results of the Voxel and Truss models can be compared. (2) Run a tension test to get more experimental data. (3) Calculated and reported some error measurements of the Truss model in comparison with the Voxel model (see Comment 5 below). (4) Presented in a clearer way the computational (memory and time) efficiency of the Truss model (see Comment 6 below).
4	Quantitative results are not even given in terms of approximation quality parameters between voxel set and truss graph representations.	We thank the Referee for the valuable comment. To abide by the observation of the Referee, we have included in Sec. 4.1 a quantitative comparison of the porosity parameter between our truss simplification and the voxel set.
5	Even if I do not have enough expertise to go into detailed judgment of the application part regarding stress-strain computation, I appreciate the declared application value but the comparison still seems to me quite qualitative and scarcely commented.	We thank the Referee for the valuable comment. To address this observation we have calculated and reported in Sec. 4.2 some error measurements of the Truss model in comparison with the Voxel model: "Taking the maximum displacements of the Voxel model as reference values, the error of the Truss model in the estimation of X displacements in the shear test is 12.5%. In a similar fashion, the error in the estimation of Z displacements in the tension test is 15.1%."

6	Moreover Table 2 does not report any timings comparisons while it seems to me they should be relevant as well.	The Referee is right. We have included a comparison of the computing time expenses between the two models in Section 4.2: "The saving factor in all categories (FE nodes, elements, equations and memory) in favor of Truss graph data is in the order of 10^2. To determine how such saving factor impacts the computing time, we recur to the order of growth O of the execution time in terms of the number of nodes. In the worst-case scenario, the bandwidth of the stiffness matrix is $O(N^2)$, where N is the number of nodes. Hence, the time complexity of a FEA simulation is given by the term $O(N^3)$ ([FSSC11]). Then, a difference of 10^2 in the number of elements, implies a difference in the order of 10^6 in the number of operations that need to be performed to simulate the models."
7	Minor issues to be fixed: What's the difference between skeleton and truss graph. Is the truss graph a denoised skeleton? Please give a more formal definition of truss graph.	We thank the Referee for the valuable comment. To abide by the Referee's observation, we have added the definition of Truss Graph: "Truss Graph. The bar + node representation of SK(B), with the radii and dimensions of bars and nodes being determined by the mass information present in SK(B). The Truss graph includes kinematic and torque restrictions required to mimic joints of the physical equivalent frame."
8	On page two the following part is written twice: "Given a 2-manifold.4 points"	We thank the Referee for the comment. We have corrected this error. The repeated paragraph has been removed.
9	On page 2: "surface skeleton (2D) surface" I think there is a "surface" too many.	We thank the Referee for the comment. We have corrected this typo error. The repeated word has been suppressed.

10	In sec. 2.3 differences and possible advantages of the proposed approach with respect to [COU*18] should be clearly stated.	We thank the Referee for the valuable comment. To abide by the Referee comment, we have modified the item 1 of the list in Sec. 2.3 as follows: "1. Synthesis of the Truss graph directly from the Voxel scalar field B, without passing by the computing- and labor - expensive skin B. Notice that this is an important advantage with respect to [COU*18], where a smooth, water-tight, manifold, high-quality triangular mesh is required to obtain the medial-axis using the Mean Curvature Flow approach reported in [TAOS12]."
11	Figure 4 should be referenced as Algorithm 1.	We appreciate the Referee's comment. Figure 4 is now referenced as Algorithm 1.
12	Page 5. "The high level of noise in Fig.4" sure that is Fig.4?	We appreciate the Referee's comment. We have corrected this typo error. The paragraph now reads: "The high level of noise in Fig. 5 is removed by replacing quasi linear paths with a straight edge."
13	Unreferenced Fig.8 (which should be Algorithm 2).	We appreciate the Referee's comment. To abide by the Referee's observation, we have: (1) Changed the reference from Figure 8 to Algorithm 2. (2) Added in the first paragraph of Sec. 3.2 the following text: "Algorithm 2 presents a description of the procedure to obtain the Truss graph from the Medial Axis."
14	It seems to me that Fig.9 (a) and Fig.10 (a) are different rendering of the same structure. Fig. 9 and 10 should be fused in a single clearer figure.	The Referee is right. We have merged former Figures 9 and 10 into current Figure 7. We also have added new results to the current Figure 7, in concordance with Comment 6 of Referee 2.
15	Fig.11d and 11c should be switched in position.	We thank the Referee for the comment. We have switched Figures 11c and 11d, as per the Referee's request.

2.2.2 Responses to Referee 2

The paper describes a method to extract a truss representation starting from a scalar field (voxels) with no need to explicitly calculate an intermediate BRep representation. As far I understand, their proposal is based on the idea of extracting the medial axis by contraction, removing defects, and finally convert the clean medial axis to a truss representation. This pipeline sounds good, but

from my point of view, the paper needs some major revision to make the reader follow the pipeline and be convinced of the results.

Table 2.3: Responses to the observations of Referee 2 of article "Direct Scalar Field - to - Truss Representation and Stress Simulation of Open Pore Domains".

Item	Observation	Actions Taken
1	The paper needs some major revision to make the reader follow the pipeline and be convinced of the results.	We thank the Referee for the comment. We have improved the pipeline explanation and added new results to improve the quality of our contribution. We report in this table the details of the mentioned improvements.
2	Section 3 starts with the first step of the pipeline. A global overview of the method is missing. I would add it just before Section 3.1 to help the reader follow the paper.	To abide by the Referee's observation we have added the following text at the beginning of Sect. 3: "In this section we present the implemented method to estimate a truss graph simplification from the skeleton SK(B). We use as input the CT of the sample, expressed as a scalar field f in the form of voxels. In Section 3.1, we calculate the medial axis of B (MA(B)), which contains information about the mass of B. Then, in Section 3.2, we use MA(B) with the mass information to find a truss graph simplification of B, which is well suited to model bar pore materials."
3	Also, Section 3.2 titles "truss graph from medial axis" but it actually describes the cleaning operations. I would suggest to re-title section 3.2 as "Cleaning medial axis" (or similar) and to move the truss representation (described in 4.1) in an additional Section 3.3	The Referee is right. Sect. 3.2 only presented the cleaning operations and not the whole process to obtain the truss graph from the medial axis. Therefore, we have extended Sect. 3.2 so that it presents all the steps in Algorithm 2 to obtain the truss graph. The added text at the end of Sect. 3.2 reads: "Wire connectivity in SK(B) is used in conjunction with the mass information to produce a truss graph [V,E] (e.g. Figs. 11(c), 11(g)). Elements in V and E are assumed to be spheres and cylinders, respectively. Finally, we estimate the radius of each element in V and E by using its geometric and mass data, as shown in step 5 of algorithm 2."

4	Also, check the usage of the terms "medial axis" and "skeleton". In some parts of the description, they are used as synonyms, but they are not, as underlined in the formal definitions and in figure 3.	We thank the Referee for the comment. We have reviewed all the text and have changed the wrong instances of both terms medial axis and skeleton.
5	Looking at the result section, a single result is shown. I would appreciate some more results (2-3 at least) and some comparison with previous works. Is the proposed method more efficient than previous methods based on the extraction the intermediate Brep? What about the quality of the generated truss wrt the previous methods?	We thank the Referee for the comment. We now present two results of the computation of the Truss structure from voxel-based domains. Besides, we have added a quantitative evaluation of the approximation quality of the Truss representations with respect to the original voxel-based samples. A comparison of the presented voxel-to-truss method with respect to other related approaches is left for future work, since it is out of the scope of the present article.
6	Minor changes: - The Glossary at the beginning of the paper is redundant. The same definitions are in the Introduction section and after, thus it can be removed.	We appreciate the Reviewer's observation. We have removed the Glossary to avoid the repetitive definitions.
7	- Figure 1b is incomplete. The rectangular window is empty. Also, add to the caption the meaning of symbols in figure 1b.	In order to address the Referee's observation we have: (1) Modified the rectangle in Figure 1(b) so that it shows an empty space. (2) Specified in Sec. 1 (just before the definition of k-manifold) that the subset of the domain in the rectangle is not processed. (3) Added to the caption the meaning of the symbols in Figure 1(b): "Skeleton from Solid in Fig. 1(a). Limbs are formed by curves (e.g. $c_i(u), c_w(u), 0u1$) and local radius r_i."
8	- The definition of a k-manifold refers to a B(p,r). Please, clarify that it is a ball centered in p and having radius r. Be aware that the B symbol represents the surface in the following paragraphs. Please, disambiguate the symbol.	The Referee is right. We have changed the symbol B(p, r) to Ball(p, r) and have added the following text to the definition of k-manifold: "() where Ball(p,r) is an open ball centered at p with radius r."
9	- Just after the definition of a skeleton, a non-titled paragraph repeats the definition of medial axis. Please, remove it.	Please see comment 15 of Referee 1.

10	- I would add the definition of Truss graph in the list of formal definitions.	Please see comment 7 of Referee 1.
11	- Section 3.2, at the end of the left column, refers to Fig. 4 ("the high level of noise in Fig. 4 ..."), but figure 4 shows an algorithm and not an example of noisy medial axis. Please, check and correct.	Please see comment 12 of Referee 1.
12	- Figure 5: Is there any reason why the boundary of the noisy medial axis is curved, while it is straight when hair is removed? I would integrate figure 5 with the recursive subdivision applied to fig 5a to obtain 5b, instead of using the additional figure 6.	In order to address the Referee's observation we have: (1) The boundary of the medial axis of Fig. 5(a) has been changed, so that now it is straight. (2)We have added the following text in the third paragraph of Section 3.2 to clarify to the reader that the hair removal and linearization are two independent processes: Once the hairs have been suppressed, it is necessary to execute a linearization of the resultant medial axis to eliminate oscillations and high curvatures in the node - to - node paths."
13	- Figure 9b shows an intermediate skeleton, while the caption says it is the medial axis. Please, check. Additionally, the text says that solid lamps are present. Please, underline solid lamps in the figure.	The Referee is right. We have placed a new caption that corresponds to what is presented in the former Figure 9 (current Figure 7). We have also marked some zones in the figure to ease the visualization of the solid lumps.
14	Also, add an additional subfigure (9c) to show the final result.	Please see comment 14 of Referee 1 and its respective response.
15	- It would be better to use the LA-TEX construct for algorithms instead of using figures showing pseudocode.	We have addressed the observation of the Referee. We have used Latex code instead of figures to show the algorithms.

2.3 FEA Structural Optimization Based on Metagraphs

2.3.1 Responses to Referee 1

Table 2.4: Responses to the observations of Referee 1 of article "FEA Structural Optimization Based on Metragraphs".

Item	Observation	Actions Taken
1	This is very interesting paper aimed to improve structural optimization of 2D shapes. Paper is well structured and has only minor suggestions: 1. Abstract must not exceed 150 words.	The Abstract has been rewritten to fulfill the Reviewer's requirement.
2	2. The total number of pages must be no more than 10.	The manuscript has been on one hand shortened, but on the other hand additional material has been added to abide by the Referees' observations. At this time, the manuscript has 12 pages. We are, obviously, ready to assume the extra pages fee, as per the SOCO2018 regulations.

2.3.2 Responses to Referee 2

Table 2.5: Responses to the observations of Referee 2 of article
"FEA Structural Optimization Based on Metragraphs".

Item	Observation	Actions Taken
1	The paper presents interesting initial results for a practical problem, it looks like a good paper, but the results are compared only qualitatively, there is no discussion of computational time demands against the quality of the solution in comparison to competing approaches.	To abide by the Referee's observation, we have inserted Section 4.3 (Computational Demands of the Proposed Algorithm). In this section we added: a- Table 1, which presents the computational expenses of our algorithm. b- The following text: "Due to the material removal procedure associated to the presented algorithm, given the mesh $M_i = (N_i, E_i)$ at iteration i we can say: $|N_0| > |N_i|$ and $|E_0| > |E_i|$, where $M_0 = (N_0, E_0)$ is the initial mesh. In addition, $|N_0| > |E_0|$. Therefore, the computational demands of one iteration of the algorithm can be expressed as a function of N_0 and the bandwidth W of the stiffness matrix calculated during the FEA simulation [5]. Table 1 presents the computational expenses of our algorithm. Notice that the time complexity and memory complexity of an iteration of our algorithm is dictated by the term $O(N_0^2)$. This term corresponds to the dominant generation of the graph and the metagraph associated to the FEA mesh. A comparison of the computational resources used vs. the efficiency of evolution is beyond our capabilities. One reason for this limitation is that the measure of the quality or efficiency of an evolution is itself an open research question at this time."

| 2 | Also, while the algorithm compares results in principle with evolutionary based approaches, there is very little of evolutionary approach in it (no crossover, no mutation, just basically iterative greedy approach). | To abide by the observation of the Referee, we have 1- Added the following text to the Section 2.4 of the manuscript: "The present manuscript intends to illustrate a methodology to use graphs to administrate the information of neighborhood and static connectedness to support an independent shape evolutionary strategy. We do not try in the present status of our manuscript to evaluate or apply alternative evolutionary strategies (e.g. mutation and crossover operators [7,9]). Our future work seeks to widen the variety of stimuli (kinematics, abrasion, temperature) that drive evolution in the nature domain." 2- Modified the end of Abstract to: Future work addresses the implementation of such stimuli type, the integration of our algorithm with other evolutionary based techniques and the extension of the method to 3D shapes." 3- Modified Section 5.2 (Future Work) to mention the need of further research in the integration of our algorithm with other evolutionary based techniques. |

2.3.3 Responses to Referee 3

Table 2.6: Responses to the observations of Referee 3 of article "FEA Structural Optimization Based on Metragraphs".

Item	Observation	Actions Taken
1	This paper presents and alternative design for FEA Structural Optimization. The paper is generally well written, with a good structure and adequately referenced. It proposes a different approach to deal with non-valid FEA configurations. The paper could give more emphasis to the evolutionary component.	Please see responses to Observation 2 of Referee 2.

2.3.4   Responses to Referee 4

Table 2.7: Responses to the observations of Referee 4 of article "FEA Structural Optimization Based on Metragraphs".

Item	Observation	Actions Taken
1	The title of the paper is very illustrative of its contents. I found the subject relevant and the approach worth pursuing. The manuscript is completed with a set of simulation results illustrating the merit of the contribution. Introduction could be rewritten to appeal to a wider audience. As it is written, it is very hard to understand what is the problem, the approached followed and how it related to the existing approaches. This can only be appreciated after reading most of the paper.	We have added a paragraph to the Introduction, offering a justification for the meta-graph approach. This paragraph had to, however, be very concise, not to extend our already outsized manuscript. This additional paragraph reads: "Shape evolution, in nature, demands that the shape continue to execute the function while evolving. This circumstance obliges each evolution individual to transmit force, torque, motion, etc. as per the constraints imposed to it by the stimuli and demands that it receives. This stability in function designates neighborhoods of the shape as "indispensable", while others are "expendable". This manuscript focuses on the synthesis, classification and administration of indispensable vs. expendable shape neighborhoods of a given shape, via graph modeling" In addition, some grammar errors of the Introduction and general manuscript have been corrected.

2.4 FE-Simulations with a Simplified Model for Open-Cell Porous Materials: A Kelvin Cell Approach

2.4.1 Responses to Referee 1

The paper proposes a new approach in dealing with FEA of foam like structures which is known as a difficult subject to tackle in modeling of porous materials.

It seems to be enough evidence in the open literature that such a cell model is suitable for modeling porous materials in this case rigid metallic porous materials. A specific type of constraints as well as boundary conditions is used in the modeling along with a simpler type of element which enables the analysis of up to 1000 cells. The literature presents models based on complex elements solid 3D elements with multiple degrees of freedom which it is known that is not suitable for large models.

Table 2.8: Responses to Reviewers' observations of article "FE-Simulations with a Simplified Model for Open-Cell Porous Materials: A Kelvin Cell Approach".

Item	Observation	Actions Taken
1	The domain characterization needs to be determined as the result is sought using numerical approach so specific size of nodes, links is assumed based on some undisclosed source (in the paper the density of the porous material is called for this assumption but other configurations will provide same density. I believe that the authors need to provide the reasons for their size selection. A slight change may significantly influence the results so this aspect needs to be set.	To abide by the observation of the Referee, we have effected these changes in the manuscript: 1. We moved misplaced former "Table 1. Relative density of the analyzed domains" from Section "3. Methodology" to Section "4. Results", because it is a result (not an input) of our work. This table is now Table 2. 2. We added in Section "3. Methodology" this text: "The specification of the Kelvin Cell properties (material and statistical dimensions) corresponds to an existing physical sample with height 100 μm and average ligament radius 5 μm [8]." 3. We added the size of the Kelvin Cell "(current) Table 1. Simulation Set Up" 4. We have clarified and ordered "(current) Table 1. Simulation Set Up".

2	Further the model is built automatically built by generation of nodes, beams and joining base on a pre-set algorithm. However, little explanation is provided with respect to selection of the solid element 182. Same issue needs to be addressed in 3.3.1 for BEAM 188. There are few options which should be discussed and eventually, the selection may come clear.	We have addressed the observation of the Referee. A discussion about the selection of elements has been added in Section "3.2 Generation of BREP and Truss Models": 1) Solid Case: In Section 3.2.1: "For full 3D FEA simulation we use elements SOLID185 [1]. These elements are first order ones (2 nodes/edge) and accept linear and non-linear analysis. Other ANSYS elements (SOLID186, SOLID187) have higher order, thus demanding more computational resources. Elements SOLID186 and SOLID187 are not needed for elastic compression loads." 2) Truss Case: In Section 3.2.2: "We use BEAM188 for the FE analysis. This is a first order element and serves linear elastic loads (our simulation domain). ANSYS element BEAM189 was not selected since it has higher order (not essential in our case) and thus demands larger computational resources [1]."
3	Further, a compression test is simulated on both solid model and the truss-based model. Young modulus and Poisson ration are evaluated for the results of the two simulations while the reference is assumed in the BREP model. Further, the computation resources are discussed. The results are presented in a string-like format. There are 10 table that are difficult to follow. I suggest to attempt to set all results in a sole table where all the information is available at one glance.	We thank the Referee's observation. We attempted to reduce all tables to one. This reduction was not possible, because some tables were incompatible with others. Therefore, we: (a) Reduced from 10 to 3 Tables, merging the compatible material. (b) We introduced XY plots which display the information in the tables, for the benefit of the reader.

4	There are 21 figures presented in the paper. I find many as not necessary. For moduli estimation there are used 6 figures which I find not all relevant. I suggest reducing the number of figure to a minimum necessary as, the way the figures are presented bring no information to the value of the paper.	We have addressed the observation of the Referee. Multiple editorial changes have been made: 1) We have reduced the number of figures from 21 to 10. 2) In Sections 1 (Introduction) and Section 2 (Literature Review), we have also effected multiple local changes to improve the readability of our manuscript. 3) In Section 3 (Methodology), we have suppressed unnecessary tables, figures and non-relevant implementation details, to present our approach in a clearer way. 4) In Section 4 (Results and Discussion), we have: (i) deleted non - relevant tables and figures, (ii) re-written the text to clarify the advantages and disadvantages of our approach. 5) In Section 3 (Methodology), we have added a paragraph discussing the difference between "Torque enabled" vs. "Torque disabled" Trusses. We have correspondingly used these terms in the text and in the reduced set of Tables and Figures.
5	The approach is interesting although the errors for small number of cells is relative large for even once cell. I assume that introduction of some anisotropic terms may improve the matching of the results provided for small number of cells by the two approaches: solid modeling vs. truss.	We thank the Referee observations. 1) Considering the Reviewer comment about the accuracy of the Truss approach, we have added the following text in section 4.2 (Mechanical Moduli Estimation): "For few (less than 8) Kelvin cells, the Truss model does not correctly mimic the BREP model. However, notice that the computational cost of the BREP model is so large that only 12 Kelvin Cells can be modeled in total. It is worth remarking that for larger domains (8 or more cells), the Torque-enabled Truss model almost halves the error of the Torque-disabled model in the estimation of the Young's modulus, being indeed a stiffer model than the one used in [8]." 2) Regarding the Referee comment about the introduction of anisotropic terms, we have included this text in Section 5.1 (Future Work): "The Kelvin cell considered in this article is isotropic (i.e., both geometric and lattice manufacturing conditions). On the other hand, in spite of geometrical symmetry, anisotropy may be also introduced by construction orientation (e.g. additive methods). This fact shows that anisotropy in lattice materials is a very extensive and complex research area, which we do not intend to undertake in the present work."

Chapter 3

Non-Manifold Modelling of Lattice Materials using Kinematically Constrained FEA

Diego Montoya-Zapata[1], Oscar Ruiz-Salguero[1], Juan Lalinde-Pulido[2], Juan Pareja-Corcho[1], Jorge Posada[3]
[1] Laboratory of CAD CAM CAE, Universidad EAFIT, Medellín, Colombia.
[2] High Performance Computing Facility APOLO, Universidad EAFIT, Medellín, Colombia
[3] Vicomtech, Spain.

3.1 Context

3.1.1 Proof of Publishing

This publication presents the results of a collaborative work between the following institutions: (1) Universidad EAFIT, represented by Laboratory of CAD CAM CAE Research Group and the High Performance Computing Facility APOLO, and (2) Vicomtech.

Figures 3.1–3.3 show proofs of the publication of the article `Non-manifold modelling of lattice materials using kinematically constrained FEA` in the Proceedings of TMCE 2018. Figures 3.1 and 3.2 present the front matter and the edition notice of the Proceedings Book of TMCE 2018. In Fig. 3.3 is depicted the portion of the table of contents that references our article (pp. 657).
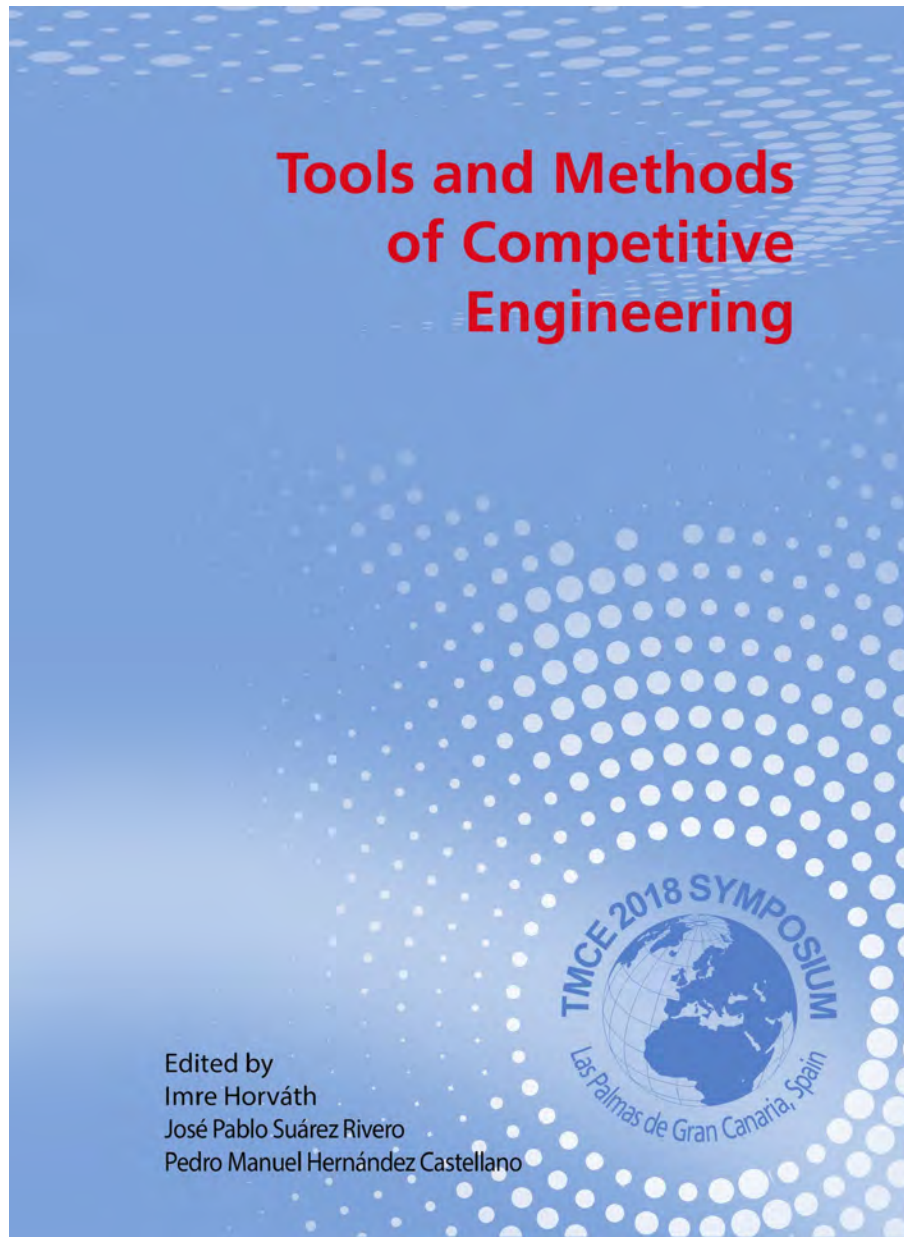
Figure 3.1: Front cover of the Proceedings Book of TMCE 2018.

II

Figure 3.2: Edition notice of the Proceedings Book of TMCE 2018.

24

Figure 3.3: Portion of the table of contents of the Proceedings Book of TMCE 2018.

3.2 Abstract

In geometric modelling and finite element analysis (FEA) of lattice materials, the datasets are usually massive, and thus intractable for even the most basic workpieces. Since slender and thin shapes are involved, the size of traditional 3D finite elements is minute, and thus the model sizes explode. 3D modelling of slender shapes is only accepted by very basic shapes, or else, through material tests. In silico simulations of nontrivial 3D slender shapes do not terminate, usually not passing the 3D meshing stage. Slender plates can be practically finite element analysed with 2D FACE + thickness elements, but such 2D elements accept no Boolean union as they produce non manifold situations. The existing alternative, of replacing the Boolean unions by node constraints, is not well studied. Responding to this void, this manuscript presents the non-manifold data structure and FEA modelling of complex lattice workpieces using 2D FACE elements assembled with several linear kinematic constraints (also called 2.5D FEA). The data structure is a variation of the 3D solid models which accommodates in natural manner the 2.5D models. We present comparisons between 2.5D vs. 3D FEA for the cases which actually terminate (i.e. for very elementary workpieces), showing a numerical result agreement which is reasonable for many early design scenarios using lattice materials. Future research may be addressed in contrasting the numerical results with real laboratory tests. Future work is required in the modelling of more complex kinematic constraints among the 2D FACEs, which would permit to simulate a broader range of materials and designs, as well as the extension and modification to this approach for emerging applications in the field of additive manufacturing.

3.2.1 Keywords

Lattice materials, non-manifold modelling, kinematic constraints, computational mechanics, additive manufacturing

Nomenclature

1-Manifold in $\mathbb{R}^3$:	A set of points in $\mathbb{R}^3$ in which all local neighbourhoods are homomorphic to the interval $(0,1)$. A curve in $\mathbb{R}^3$ which contains no self-intersections.
2-Manifold in $\mathbb{R}^3$:	A set of points in $\mathbb{R}^3$ in which all local neighborhoods can be flattened (i.e. are homeomorphic to a disk in $\mathbb{R}^2$). A surface in $\mathbb{R}^3$ which contains no self-intersections.
$2\frac{1}{2}$D:	Finite Element representing a thin wall by a 2D FACE with thickness (noted also as 2.5D).
BB	Bounding box. Smallest orthogonally oriented rectangular prism containing the workpiece.
B-Rep:	Representation of a solid in R^3 by using its boundary or skin.
CT:	Computer Tomography.
DOF:	Degree of freedom.
E:	Young's modulus of the bulk material (GPa).
FACE:	A 2-manifold in $\mathbb{R}^3$ with border.
FEA:	Finite Element Analysis.

FEM:	Finite Element Method.
V:	Poisson's ratio of the bulk material (dimensionless).
VoXel:	Volumetric PiXel or cubic cell in $\mathbb{R}^3$ located in a 3D discrete grid as dictated by Medical or Industrial Imaging.
Ω:	Subset of $\mathbb{R}^3$ that represents the workpiece.
K_i:	Kinematic Constraint involving points, straight line segments, etc.

3.3   Introduction

Computational mechanics simulations of lattice or porous materials involve massive geometry datasets. The geometries of these materials have two independently undesirable characteristics, which produce large datasets: (1) cell walls and links are usually very slender, and (2) cell sizes are very small when compared to the functional dimensions of the latticed workpiece. Together, (1) and (2) make unfeasible the 3D full geometry simulation of a latticed workpiece.

Finite element analyses with 3D elements require a 2-manifold Boundary Representation (B-Rep) of the multiple SHELLs that bound the solid or BODY. Current solid modelling techniques guarantee such manifold properties when the SHELLs are the result of Boolean Union among the boundaries of small solid pieces that compose the lattice workpiece. FEA meshing is fully understood and correctly implemented for such solids. However, the 3D elements required to mesh such BODYs must have an aspect ratio in the order of 1.0. Therefore, the 3D elements (e.g. tetrahedral, block) must be exceedingly small due to the slender aspect of the lattice walls. The result is an explosive number 3D FEA elements.

For slender shapes, FEA provides 1-manifold and 2-manifold elements, which allow representing a rod (1D) or a thin plate (2D) with large FEA Beam or Shell elements, respectively. This approximation allows posing a 1D or 2D tractable FEA problem for slender workpieces. However, a problem arises as the rod or plate is mechanically attached (welded, screwed, fastened) to other rods or plates, since the Boolean union of several 1- or 2-manifolds incident to a point violate manifoldness. Such a violation immediately impedes the FEA process.

Current FEA software provides a way (called 2.5D) to by-pass the non-manifold character of such Boolean unions by replacing the union with sets of kinematic constraints among the nodes of the Beam and Shell elements meant to be mechanically fastened. Each FACE, independently considered, is a 2-manifold with border. Its border is, as usual, modelled as a set of EDGE sequences. However, an EDGE may represent the incidence of more than 2 FACEs, which is a fundamental departure from classic manifold modelling. In this approach, kinematic constraints are enforced among the FEA nodes (belonging to several FACEs) that happen to fall onto, or be near to, a given EDGE. Such constraints replace the Boolean union of the several FACEs incident to the EDGE.

Current research does not define the type of constraints placed among nodes of the various FACEs being incident to an EDGE. For example, given element segments $\overline{ab}$ and $\overline{cd}$, one could have (i) $a = c$, $b = d$, and all interior points of $\overline{ab}$ be coincident with interior points of $\overline{cd}$, (ii) $a = c$ and $b = d$, with freedom in all intermediate points of the segments, (iii) node a being in the interior of segment $\overline{cd}$, (iv) orientation equality (enforced or waived) of the coordinate systems attached to the nodes a and c in (i) - (ii), (v) distance constraint between nodes (i.e. spherical joint), (vi) spring constraints between nodes (i.e. weighted spherical joint), etc. There is also an emerging need for simplified computational models of the material behaviour when engineered lattice materials are produced with additive manufacturing techniques. For instance, the work of [3] shows interesting experiments of compression of octet truss and Kelvin cell unit cells foams, but the simulations are

performed with classical FEM methods.

This article contributes in the following aspects: (1) compares the accuracy and feasibility using of 2.5D FEA vs. full 3D FEA for modelling thin wall lattices, (2) develops and uses a formalism (data structure) to model lattice workpieces and translate them into 2.5D FEA models, (3) implements and presents the results of constrain models (i) and (ii) above. Our investigation shows a dramatic superiority of the 2.5D FEA against 3D FEA models, as only trivial load computations of the 3D case actually terminate.

Section 2 reviews the existing literature on the topic and positions this article's contributions. Section 3 discusses the Methodology used to implement our contribution. Section 4 presents the results of the tests run to assess our method. Section 5 concludes the manuscript and informs of the improvements needed and research fields open as result of our approach.

3.4 Literature Review

3.4.1 Computational Modelling of Porous Materials

Several computational feasible models for FEA have been used to study the mechanical behaviour of porous and lattice materials with slender walls. These models can be divided in four groups: (1) VoXel based models, (2) B-Rep based models, (3) tessellation based models, and (4) unit-cell models.

VoXel Based Models

VoXel based models are derived from Computer tomography (CT) scans of the actual specimen. A VoXel is a 3D cubic PiXel. VoXel based models have been used to study the mechanical behaviour of porous materials in [4–7]. VoXel models are easily obtained from CT images. However, these models have two disadvantages: (1) they produce an intractable amount of finite elements (blocks, hexahedra) [4], and (2) geometrical inaccuracies may result from converting directly VoXels into finite elements [4]. The first drawback impedes the FEA of large domains using VoXel based models.

B-Rep Based Models

B-Rep models are also derived from CT scans of the actual workpiece. However, in contrast with VoXel based models, B-Rep based models require the smoothing of the VoXels of the CT images and a legal B-Rep of the domain must be obtained. For this reason, a precise description of the geometry of the actual domain is obtained [8]. These models are widely used to perform mechanical characterizations of porous materials [4, 8–10].

However, the main drawback of B-Rep models is the massive number of elements required to mesh the final volume [9]. This is reflected in the large amount of memory and time consumed in the generation of the model [6, 10]. Hence, as for VoXel based models, it is not possible to analyse numerically large domains represented with B-Rep based models [6, 10].

Tessellation Based Models

A 3D tessellation is a division of a finite volume into cells, so that the cells form a partition of the initial domain. In general, the cells are irregular and randomly arranged. Different tessellations are

28

used to study porous and lattice materials, mainly Voronoi [11–13] and Laguerre [14–16] tessellations. Tessellation based models for FEA are obtained by meshing the cells of the tessellation with Shell finite elements.

When a preprocessing of the domain is carried out, tessellation based models are able to mimic some morphological characteristics of the actual specimen, such as the porosity, mean cell size and mean cell wall thickness [12–14, 16]. However, they are not capable to represent faithfully the geometry of the actual domain.

Unit-Cell Models

Unit-cell models consider that the domain is composed by arrays of regular polyhedrons, with Kelvin cells being particularly popular ([17–21]). Other structures addressed include cubic spherical or cruciform-pyramidal cells [18].

Unit cell domains allow addressing domains larger to the ones simulated with B-Rep or VoXels [13]. However, the simplification itself and constraint networks must be modelled and constructed. Such endeavours are central to the present article. Unit cells are also very relevant in additive manufacturing techniques, especially when micron scale mesoscopic structures are produced for the design of specific properties of materials (as for instance Kelvin foams) [3].

3.4.2   Kinematic Constraints in FEA of Lattice Materials

Addition of kinematic constraints has been considered to study different materials. For example in [22, 23] a variational multiscale method is used to study multiple-point constraints on composite beams of two or more shear deformable layers stacked together.

Incidence of elements having different dimensions (e.g. beam-to-shell, shell-to-solid) is addressed in [24]. Ref. [25] uses kinematic constraint for the non-linear analysis of fan blades. We have not found usage of kinematic constraints for lattice materials.

3.4.3   Non-Manifold Data Structures for Applied Mechanics

Non-manifold modelling is relevant when different dimensionality structural members (e.g. 1D Beams, 2D Shells, 3D Blocks) are connected. Ref. [26] presents the Radial Edge structure and Ref. [27] discusses a faster improvement of it (Partial Entity structure). Lately, renewed interest has appeared in non-manifold structures: [28] and [29] are improvements of Radial Edge, in the data structure domain, without application. Refs. [30] and [31] address non-manifold meshes in Computer Aided Design, without particular application domain.

3.4.4   Conclusions of the literature review

The representations used to model slender wall elements are: (1) VoXel, (2) B-Rep, (3) tessellation, and (4) unit-cells. VoXel and B-Rep based models are computationally inefficient. The use of tessellations requires a preprocessing of the domain. We also detected that FEA with kinematic constraints has not been used to analyse lattice domains.

In response to these limitations, this article assesses the accuracy of $2\frac{1}{2}$D FEA model with kinematic constraints to represent a lattice composed by Kelvin cells. We show the feasibility of this model to perform mechanical studies of large and complex-shape domains. We compare the 2.5D FEA model with constraints against the 3D FEA model.

29

We implement a data structure to treat 2-manifold violations in lattice domains, since we found that this problem has not been addressed previously in the literature. This data structure allows the manipulation of large domains and the setting of different types of kinematic constraints to study the mechanical response of lattice materials. Contributions of this article are summarized in Table 3.2. Our article does not include experiments with actual probes.

Table 3.2: Contributions of this article with respect to state of the art in the domain of in-sillico experiments.

Aspect	References	Current status	Our contribution
Computational modelling of lattice materials	[3, 4, 6, 9, 10, 12–14, 16]	(1) VoXel and B-Rep based models are computational expensive models. (2) Tessellation based models are subjected to an expensive preprocessing of the domain	(1) For tractable datasets, comparison between Full 3D B-Rep vs. 2.5D FACE + Constraints approaches. (2) Large 2.5D FACE + Constraints simulations (intractable with 3D).
FEA of lattice materials using kinematic constraints	[22, 23, 25]	Kinematic constraints are used in the study of other structures, but not for lattice materials	Illustration and taxonomy of linear constraints in 2.5D models of lattice materials.
Non-manifold data structure to manipulate 2D-Shell domains of lattice materials	[26–31]	There are plenty of non-manifold data structures, but none of these has been used in the study of lattice materials	Development of a data structure to 2.5D FACE + Constraints FEA modeling of lattices.

3.5 Methodology

3.5.1 Data Structure for Lattice Materials

Full 3D Boundary Representation

The Geometric Modelling community has standards to express solid models, which are then poured into file formats (e.g. IGES, SAT, STEP). The correspondence between the mathematical concepts and internal modeller entities is very complex. Besides the obvious data translators, Application Programming Interfaces are specified (e.g. [32]) which allow to write generic CAD-client software that runs on top of diverse actual geometric Kernels [33].

In this manuscript, we use as basis the ACIS$^{\text{TM}}$ manifoldcompliant terminology (Table 3.3, [2]), with some variations, as we intend to model non-manifold structures.

Table 3.3: Relations and hierarchy of topologic and geometric elements (informal description). Example entity names from ACIS$^{\text{TM}}$ Modeler (Spatial Corporation [2]).

Dim	Topology	Comment	Geometry	Comment
3D	BODY	Possibly disconnected compact dense point set		
3D	LUMP	Connected subset of a BODY		
2D	SHELL	2-manifold without border, subset of a LUMP boundary		
2D	FACE	Connected subset of a SHELL or 2-manifold with border	SURFACE $S(u,w)$	FACEs are mounted on Surfaces.
1D	LOOP	1-manifold without border, subset of the boundary of a FACE		
1D	EDGE	Connected subset of a LOOP or a 1-manifold with border	CURVE $C(u)$	EDGEs are mounted on Curves.
0D	VERTEX	Border (endpoint) of an EDGE	POINT (x,y,z)	A VERTEX is mounted on a Point.

Non-Manifold B-Rep

The thin walls of a lattice material can be simplified as, so called, 2.5D entities or FACE plus thickness. This name is a contradiction in terms since a FACE is a 2-manifold (i.e. has zero thickness). However, this is a useful simplification since a 2-manifold accepts much larger and fewer FEA elements. Notice that the 2.5D simplification leads to non-manifold structures, since in general more than 2 FACEs with thickness are incident onto an EDGE (Fig.3.4(a)).

Instead of conducting a Boolean union of 2.5D FACEs + thickness, $\bigcup_{i=1} F_i$, each F_i is isolated from the other F_j 2.5D FACES. The only relations among the F_is are the kinematic constraints K_j among their FACEs. Therefore, in their private modelling space, all F_i continue being legal 2-manifolds (Fig. 3.4(b)).

Fig. 3.5 displays our variation of an orthodox 3D B-Rep devoted to model slender wall (e.g. lattice) structures. The lattice does not have BODY, LUMP, SHELL objects, since it is a collection of FACE + thickness (2.5D entities). The FACEs are mounted on planes, are bounded by LOOPs, which are sequences of EDGEs. The EDGEs are mounted in straight LINEs, and have 2 bounding VERTEX objects, each mounted on a point. The kinematic constraints are enforced among finite element nodes, which appear at sub-divisions of these entities. Therefore, the kinematic constraints do not appear in this diagram.

3.5.2 Kinematic Constraints

The taxonomy and illustration of the kinematic constraints in 2.5D models of lattice materials are given in Table 3.4 and Fig. 3.6.

Table 3.4: Kinematic Constraints for FEA Modeling using FACE + Thickness Elements.

Menm.	Type	Properties
V≡V	Vertex Identity	1. EDGE $E_w = (v_k, v_m)$ in all FACEs F_i incident to E_w. 2. Unique Coord. System $S_k = [X_k, Y_k, Z_k, O_k]$ attached to VERTEX v_k in all incident FACEs F_i. 3. Position *and* Angle identity. 4. Force *and* Torque at Joint
V-on-V	Point Identity or Spherical Joint	1. Each FACE F_i incides onto its own EDGE $E_w = (v_k, v_m)$. 2. EDGES $E_w = (v_k, v_m)$ and $E_s = (v_t, v_q)$ are coincident but not identical. 3. VERTEX aliasing: $v_k \neq v_t$. 4. Systems $S_k = [X_k, Y_k, Z_k, O_k]$ and $S_t = [X_t, Y_t, Z_t, O_t]$ must be constrained to each other by either: 4.1. Position Constraint: $O_k = O_t$ (3 DOFs constrained, force constraint). 4.2. Position *and* Angle Constraint: $S_k = S_t$ (6 DOFs constrained, force *and* torque constraints).
V-on-$\overline{V_k V_m}$	Slide plus Spherical Joint	1. Constraint: Point O_6 on Segment $\overline{O_5 O_7}$. 2.1. Position Constraint: $O_k \in \overline{O_5 O_7}$ (slide joint, 3 DOF constrained, force constraint) 2.2. Position and Angle constraints: $O_k \in \overline{O_5 O_7}$ and $[X_k, Y_k, Z_k] = f(X_5, Y_5, Z_5, X_6, Y_6, Z_6)$ (slide + spherical joints, 6- DOFs constrained, force *and* torque constraint).
d(V,V)	Distance Constraint	1. Constraint: $d(O_k, O_t) = \Delta$. 2. DOFs restricted=5. 3. Highly non-linear.
F = g(V,V)	Spring (damper, etc.) Constraint	1. Constraint: $Force = g(O_k, O_t)$. 2. DOFs restricted=5. 3. $g()$: spring, damper and/or other mechanical device. 4. Highly non-linear.
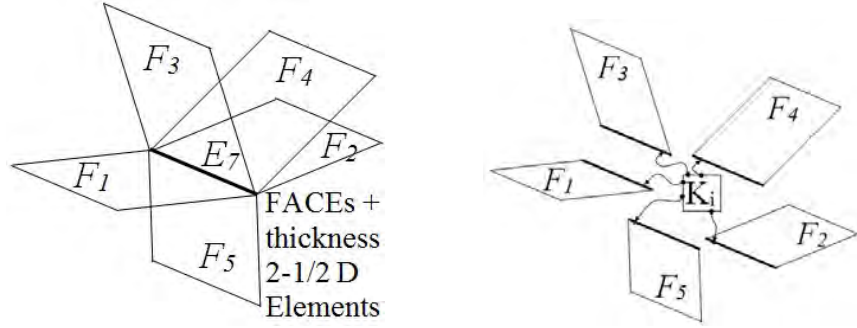
(a) Non-manifold to-pology if Boolean Union of incoming FACEs is applied.

(b) Repair of non-manifold topology by kinematic constraint application.

Figure 3.4: 2.5D Finite Element Model as alternative to full 3D FEM for slender geometries.

3.5.3 Comparison of 2.5D FACEs and 3D B-Rep Models

Let $\Omega \subset \mathbb{R}^3$ be a rectangular prismatic lattice domain. Our goal is to assess the performance of the 2.5D FACEs model to predict the mechanical response of Ω under shear, tension, and torsion tests. We consider the 3D B-Rep model for Ω as the reference values to test the accuracy of the 2.5D model.

To achieve this goal, we follow the procedure described in Fig. 3.7. First, the 2.5D FACEs and 3D B-Rep models for Ω are obtained from the CT scan of Ω. The 2.5D model is recovered using a Principal Component Analysis to extract the FACEs and their connectivity. The B-Rep for the 3D model is obtained with an IsoSurface synthesis algorithm applied to the CT scan (e.g. Marching cubes).

Finally, we test the accuracy of the 2.5D model against the 3D model. We assume that the lattice domain Ω is formed by Kelvin cells. A detailed discussion on the considered domains and the mechanical tests performed on each domain follows.

Domain Characterization

In order to assess the accuracy of the 2D FACEs + Constraints model, we analyse four lattice domains formed by rectangular arrays of 4, 8, 27, and 64 Kelvin cells, as can be seen in Fig. 3.8. The size and properties the Kelvin cells of the four domains are listed in Table 3.5. In Fig. 3.8(a) is depicted a section view of the Kelvin cell used for the simulations.

Mechanical Analysis

The accuracy of the 2.5D model w.r.t. the 3D B-Rep model is tested for shear, tension, and torsion simulations. In Table 3.6 is presented the procedure to carry out the comparison between both models.
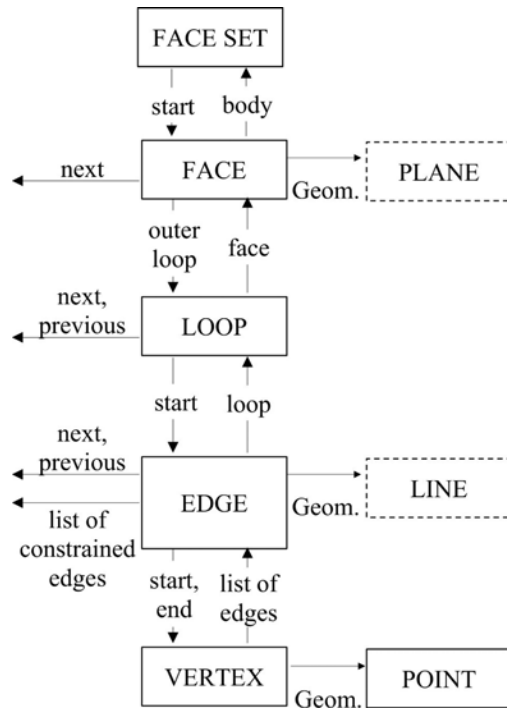
Figure 3.5: Data Structure for Geometric Modelling of Lattice Solids. The Topologies BODY, LUMP, SHELL are replaced by FACE SET.
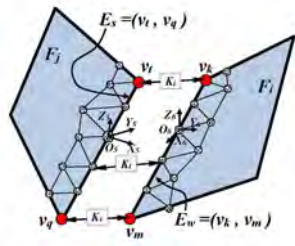
(a) Vertex-Vertex Constraint.
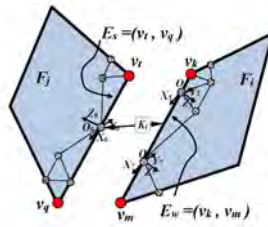
(b) Point-Point Constraint
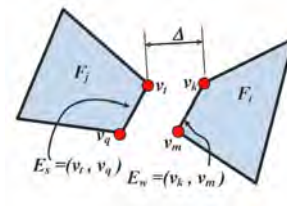
(c) Point-on-Segment Constraint.
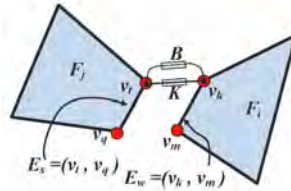
(d) Length Constraint.

Figure 3.6: Constraint types to implement FACE + Thickness modelling.

34
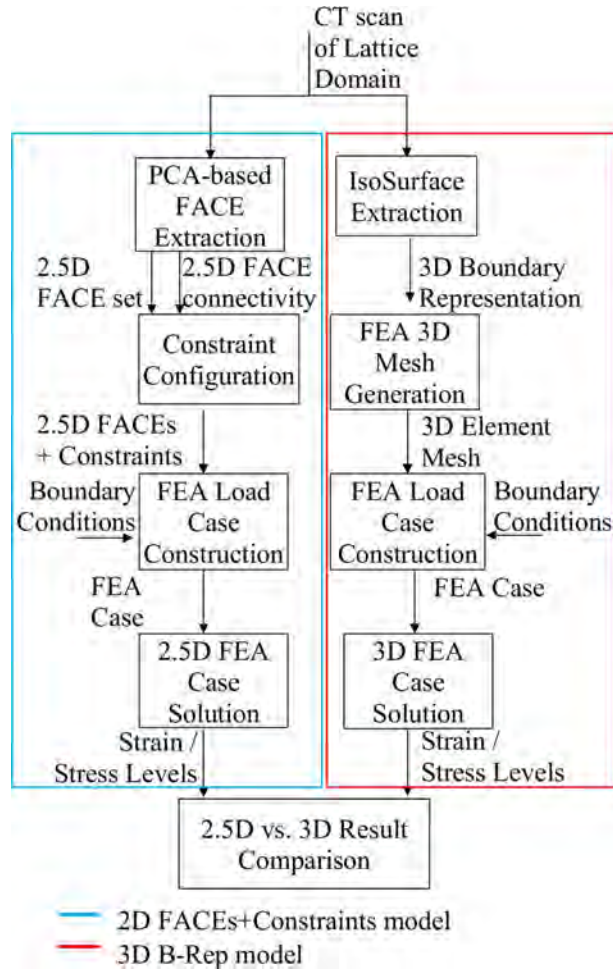
Figure 3.7: Workflow comparison between 3D Full B-Rep and 2D FACEs + Constraints modelling.

Table 3.5: Dimensions and mechanical properties of the Kelvin cell used for the comparison among 2D FACEs + Constraints vs. 3D B-Rep models.

Property	Value
Bulk material	Aluminum (AA5182) [19]
Bulk material Young's Modulus (GPa)	$E_z = 71$ GPa
Bulk material Poisson's Ratio	$V = 0.3$
Kelvin cell size (mm per side)	1.9 mm x 1.9 mm x 1.9 mm
Kelvin cell thickness (mm)	0.1 mm

Table 3.6: Description of the mechanical simulations with the 2.5D FACEs and 3D B-Rep models.

		2D FACEs + Constraints model	3D Full B-Rep model
Given		2D FACEs and Point-Point kinematic constraints between FACEs that represent the lattice domain.	3D Boundary Representation of the lattice domain.
Mesh		2.5D FACEs are meshed with the element Shell-181 in ANSYS. Very little elements are generated for comparing accurately the 2.5D and 3D models on the analysed domains.	B-Rep is meshed with Solid-285 in ANSYS. Elements are small to assure an aspect ratio close to 1.0.
Boundary conditions	Shear test	The setup of the shear test can be seen in Fig. 3.9(a). At the bottom of the domain, all DOF are constrained to 0. Loads in X direction are applied at the top of the domain. The total loads applied to each domain are listed in Table 3.7.	
	Tension test	The setup of the tension test is displayed in Fig. 3.9(c). At the bottom of the domain: (1) Z displacement is set to 0, and (2) nodes at the centre are embedded (all DOF are constrained to 0). Loads in Z direction are applied at the top of the domain. The total loads applied to each domain are listed in Table 3.7.	
	Torsion test	In Fig. 3.9(b) is described the boundary conditions of the torsion test. All DOF are set to 0 at the bottom of the domain. Loads in X and -X are applied at two opposite sides of the bounding box (BB) of the domain. Magnitudes of the loads are given in Table 3.7.	
Solution		All the simulations are carried out in ANSYS using the Sparse Direct Solver. Resultant X, Y, and Z nodal displacements are collected for subsequent comparison among 2.5D and 3D approaches.	

Table 3.7: Load magnitudes on each domain for tension, shear, and torsion tests.

Number of cells	Tension test		Shear test		Torsion test	
	Force (N)	Dir.	Force (N)	Dir.	Force (N)	Dir.
4	0.112	+Z	0.112	+X	0.112	+X, -X
8	0.112	+Z	0.112	+X	0.112	+X, -X
27	0.252	+Z	0.252	+X	0.168	+X, -X
64	0.448	+Z	0.448	+X	0.224	+X, -X

(a) Section view of the Kelvin cell.

(b) 4 and 8 Kelvin cells

(c) 27 Kelvin cells

(d) 64 Kelvin cells
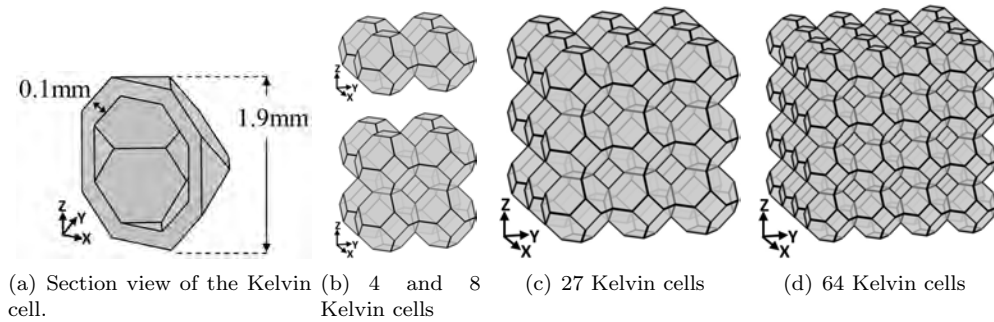
Figure 3.8: Tested domains for the comparison among 2.5D FACEs and 3D B-Rep models.

(a) Shear load case description

(b) Torsion load case description

(c) Tension load case description
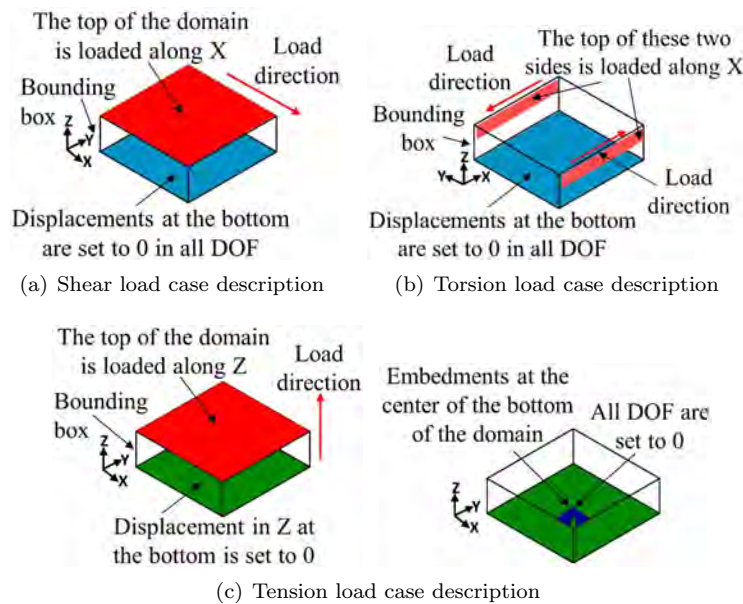
Figure 3.9: Boundary conditions of the shear, tension, and torsion tests.

3.5.4 2.5D FACEs Multi-Lattice

Let $\Omega \subset \mathbb{R}^3$ be the Elephant shown in Fig. 3.10(a). Our goals are (1) to represent Ω with Kelvin cells and (2) to show the feasibility of the 2D FACEs + Constraints abstraction to carry out FEA of large and complex-shape domains. We depict the procedure to achieve these goals in Fig. 3.11.

Model of the Elephant with Kelvin Cells

Given the B-Rep of the Elephant shown in Fig. 3.10(a), a grid of 28 x 50 x 50 Kelvin cells is generated. The size of the grid is the same of the BB of the Elephant. The size of each Kelvin cell is 4.0 mm x 4.0 mm x 4.0 mm. The other properties are the same of the Kelvin cell used

37

(a) 3D triangular B-Rep.   (b) 2.5D (lattice) representation.
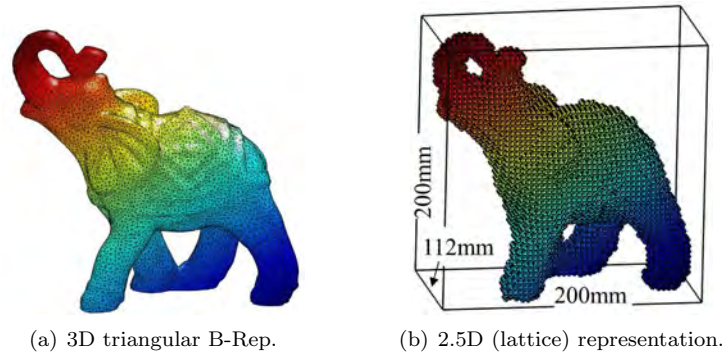
Figure 3.10: Elephant dataset.
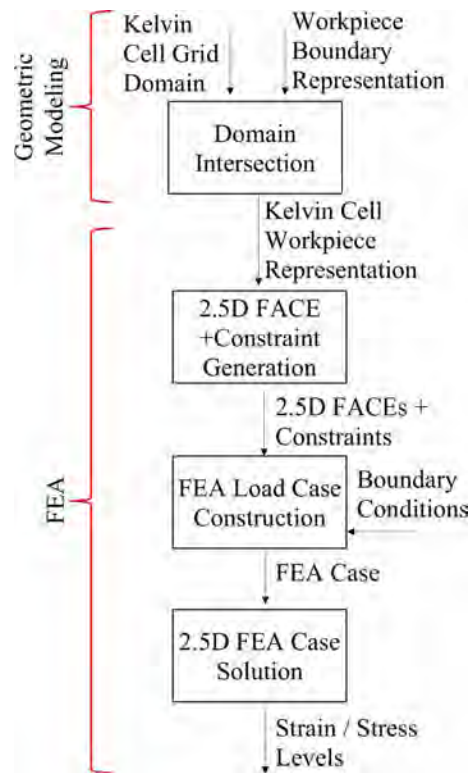
Figure 3.11: Data flow for the simulation with the Elephant dataset.

38

for the comparison of the 2.5D and 3D models (see Table 3.5). Finally, to obtain a Kelvin cell representation of the Elephant, we intersect the B-Rep of the Elephant with the Kelvin cell grid. A cell is considered to be in the intersection if at least one of its VERTEXes lies inside the Elephant B-Rep. The result of this operation can be seen in Fig. 3.10(b).

Notice that small details of the Elephant (e.g. ear and body creases) disappear in the modelling process. Kelvin cells convey a sampling of the original shape. Therefore, high frequency features disappear, representing a limitation of the shapes modelled by Kelvin cells.

FEA of the Elephant

In order to carry out a FEA of the Elephant, we execute the following steps:

1. 2.5D FACEs model generation: the 2.5D FACEs representation of the Elephant is obtained by adding Point-Point kinematic constraints are added to the FACEs of the resultant Kelvin cell model.

2. Meshing: the 2.5D FACEs of the Kelvin cells are meshed with the ANSYS element Shell-181. Since the main goal is to show the feasibility of the 2.5D model to perform FEA with large and complex-shape domains, this mesh is coarser than the mesh of the Kelvin cells for the comparison of the 2.5D and 3D models.

3. FEA load case: the 2.5D model is used to simulate shear, tension, and torsion load cases. Boundary conditions of shear and torsion simulations are shown in Fig. 3.12. Load magnitudes for each test are presented in Table 3.8.

4. FEA solution: all load cases are simulated with the Sparse Direct Solver of ANSYS.

(a) Shear test   (b) Torsion test
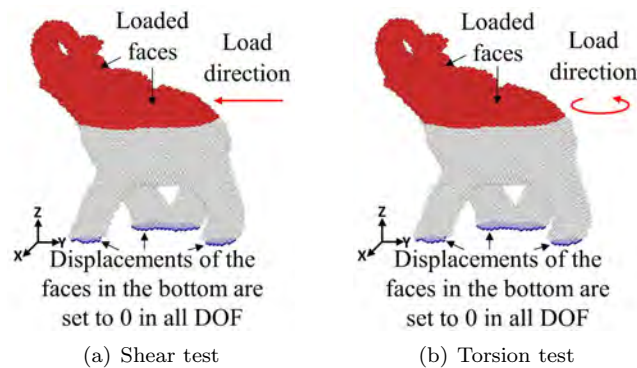
Figure 3.12: Boundary conditions for the FEA of the Elephant.

3.6 Results

Section 4.1 reports cases in which 3D and 2.5D computations are feasible and thus, comparable. Section 4.2 reports cases in which 3D computations are intractable while only 2.5D computations are feasible. In those cases, no comparison is possible.

Table 3.8: Load magnitudes for tension, shear, and torsion tests with the Elephant.

Tension test		Shear test		Torsion test	
Force (N)	Dir.	Force (N)	Dir.	Torque (N)	Dir.
21.629	+Z	21.629	-Y	21.629	+Z

3.6.1 Comparison of the 2.5D FACEs and 3D B-Rep Models

The ratio r of 3D vs. 2.5D finite elements needed to mesh a slender plate is $r \sim K(a/l)^2$, where a and l are the side lengths of the 2.5D and 3D elements, respectively, and $K = 3\sqrt{6}$. This estimation assumes: (a) the 3D domain is meshed with tetrahedra of edge length l, (b) the 2.5D domain is meshed with triangles of size length a, (c) l is at least half of the plate thickness, so that two layers of 3D tetrahedra are used to mesh.

A conservative approach, in which the side of the 2.5D elements a has the same order of magnitude as l, results in $r \sim 10$. This means that approximately 10 times more 3D elements than 2.5D elements are required to mesh a slender plate. In such conservative conditions, Figs. 3.13(a), 3.13(b) and 3.13(c) show that the saving of 2.5D models with respect to 3D ones is very high in terms of (i) number of elements, (ii) number of nodes and (iii) memory allocated by the ANSYS solver. In practice [14, 15], the side a of the 2.5D elements is significantly larger than the thickness (and therefore, larger than the edge l of the 3D elements). In such conditions, the computing resource savings of the 2.5D approach would be larger.

In Figs. 3.14 and 3.15 are presented the results of the shear and torsion simulations of the domain of 64 Kelvin cells. These figures exhibit the deformed domain and the resultant nodal displacements for the 2.5D FACEs and 3D B-Rep approaches.

The similarity in the colour distribution in Figs. 3.14 and 3.15 shows that the deformation along the whole domain obtained with the 2.5D model resembles the deformation produced by the 3D model. This assertion holds for the three types of simulations carried out: shear, tension, and torsion.

To test the quality of the results given by the 2.5D model, we calculate the relative error of the nodal displacements estimated with the 2.5D model taking as reference values the nodal displacements of the 3D model. The error is calculated using the maximum nodal displacement in each case since 1) the minimum nodal displacement is zero or the negative of the maximum nodal displacement and 2) the deformation along the whole domain is similar for both the 2.5D and 3D models.

In Fig. 3.16 can be seen the relative error of the 2.5D model w.r.t. the 3D model for the estimation of the X, Y, and Z nodal displacements in shear, tension, and torsion tests for the domains of 4, 8, 27, and 64 Kelvin cells. The dotted line represents a relative error of 16%. Notice that for the shear and torsion tests, the relative error is lower than 16% in all cases. Likewise, the error in the estimation of X and Y nodal displacements in the tension test is also lower than 16%. The error in the Z nodal displacement of the tension test is greater than 16% but it tends to decrease while the number of cells increases.

3.6.2 2.5D FACEs Multi-Lattice

The 2.5D model for the Elephant has 14K Kelvin cells. The mesh contains 906K elements and 689K nodes. In Fig. 3.17 are displayed the deformed shapes and nodal displacements of the Elephant for

40

(a) Number of elements vs. Number of kelvin cells.

(b) Number of nodes vs. Number of kelvin cells.

(c) Memory allocated by the ANSYS solver vs. Number of kelvin cells.
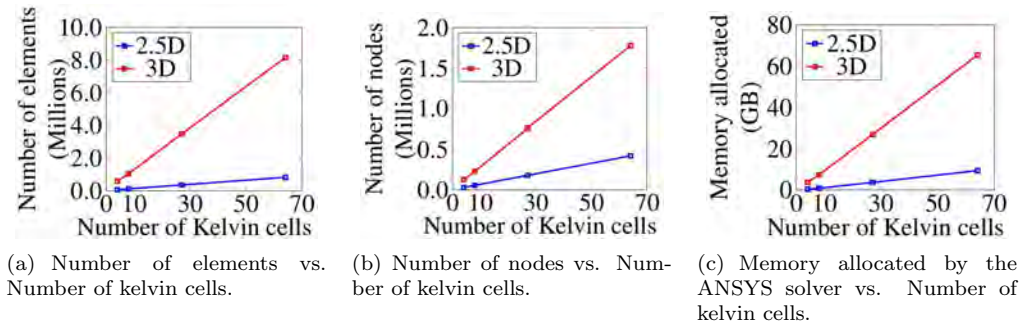
Figure 3.13: Comparison of the computational cost of the 2.5D FACEs and 3D B-Rep approaches.

(a) Shear test. X displacement (mm)

(b) Torsion test. Y displacement (mm)
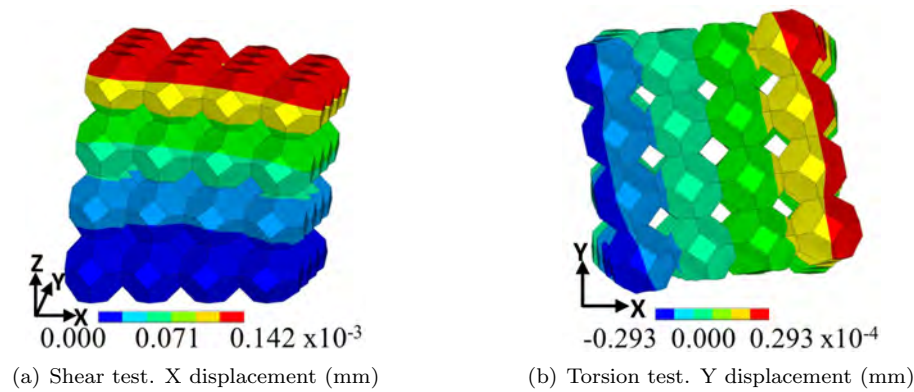
Figure 3.14: 2D FACEs + Constraints model. Domain of 64 Kelvin cells. Nodal displacements (mm) of shear and torsion tests.

the shear and tension simulations. These results demonstrate the feasibility of the 2.5D FACE + Constraints model to study large and complex domains.

3.6.3   Advantages and Disadvantages

Advantages

The results obtained in the comparison between the 2.5D and 3D approaches show that the 2.5D model is not only an efficient, but an accurate alternative for modelling and simulating lattice domains. In addition, the 2.5D approach allows the efficient computation of models composed by thousands of Kelvin cells.

The formulation of 2.5D FEA models allows for assignment of material properties reflecting anisotropy. Future research efforts include the generation of 2.5D FEA equations parameterized by such local and directional variations.

(a) Shear test. X displacement (mm)

(b) Torsion test. Y displacement (mm)
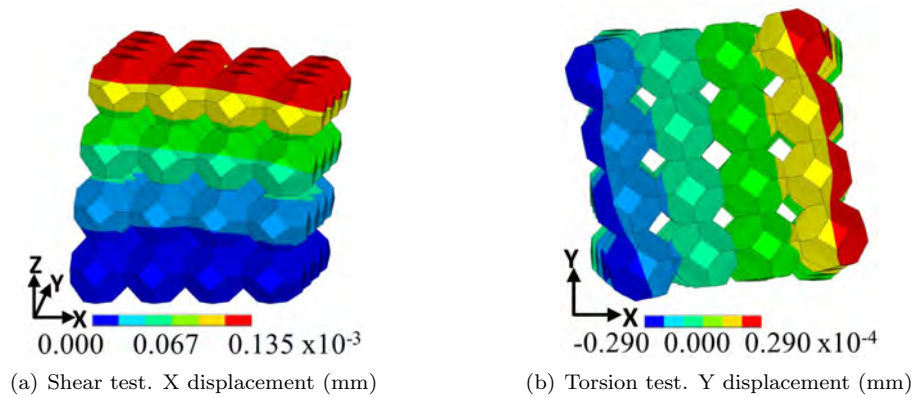
Figure 3.15: 3D B-Rep model. Domain of 64 Kelvin cells. Nodal displacements of shear and torsion tests.

(a) Shear test. Relative error (%).

(b) Tension test. Relative error (%).

(c) Torsion test. Relative error (%).
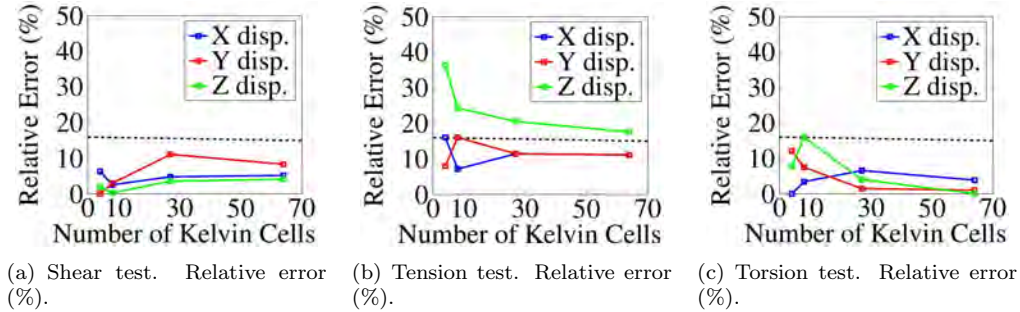
Figure 3.16: Relative error of the 2.5D FACEs model w.r.t. 3D B-Rep model.

Disadvantages

The 2.5D FACE + Constraints approach is not appropriate to model domains with small details and high frequency regions. The usage of 2.5D simplifications requires the validations against physical test results, in addition to comparison against 3D FEA model results.

3.7 Conclusions and Future Work

This article presents a methodology to model and simulate large and complex lattice domains. The presented model uses a 2.5D approach in which FACEs are joined by means of sets of kinematic constraints. The 2.5D model is found to be more computationally efficient than the 3D B-Rep model. Likewise, for shear, tension, and torsion simulations, the 2.5D model is able to reproduce the resultant nodal displacements of the 3D model with errors under 16% in the vast majority of the cases. The 2.5D model has shown to be a feasible alternative to analyse large and complex-shape domains.

This work describes the type of kinematic constraints that can be placed for lattice domains.

(a) Shear test. Y displacement (mm).   (b) Tension test. Z displacement (mm)
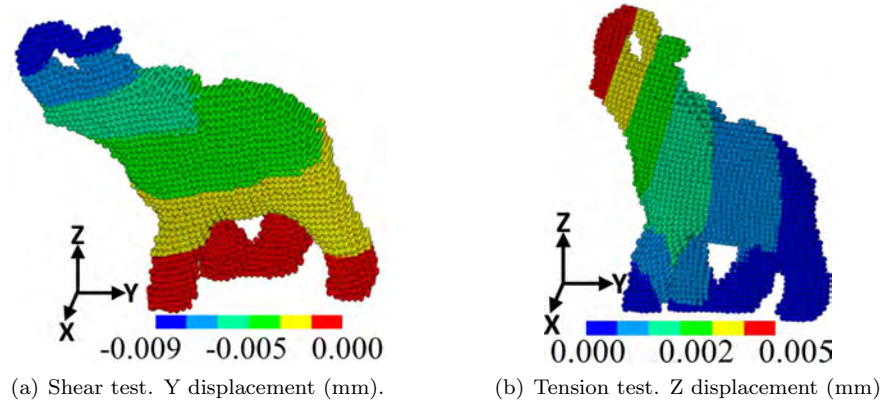
Figure 3.17: Shear and tension tests with the Elephant dataset. Nodal displacements (mm).

This article presents the development and use of a data structure to model lattice domains and translate them into 2.5D FEA models.

Future work is required in the implementation of more complex kinematic constraints, such as distance or spring constraints. In this manner, a broader range of materials and designs would be analysed. Future research is required in contrasting the results presented in this manuscript with laboratory experiments. The model presented in this manuscript could be extended to model not only lattice, but more complex thin-walled porous materials by including other geometrical and morphological characteristics (e.g. anisotropy). That would be the case for instance in the extension of this approach for Additive Manufacturing techniques.

Chapter 4

Direct Scalar Field - to - Truss Representation and Stress Simulation of Open Pore Domains

Juan Manual Munoz[1], Oscar Ruiz-Salguero[1], Diego Montoya-Zapata[1,2], Camilo Cortes[2] and Carlos Cadavid[3]

[1] Laboratory of CAD CAM CAE, Universidad EAFIT, Medellín, Colombia.
[2] Vicomtech, Spain.
[3] Functional Analysis Group, Universidad EAFIT, Medellín, Colombia

4.1 Context

4.1.1 Proof of Submission

This publication presents the results of a collaborative work between the following institutions: (1) Universidad EAFIT, represented by Laboratory of CAD CAM CAE Research Group and the Functional Analysis Group, and (2) Vicomtech.

Figure 4.1 shows a proof of the submission of the article `Direct Scalar Field - to - Truss Representation and Stress Simulation of Open Pore Domains` to the International Conference STAG 2018.

Figure 4.1: Proof of Submission to STAG 2018.

4.2 Abstract

In the domain of lattice and porous material geometric modeling, the problem of data size is central. When using full 3D manifold Boundary Representations (BRep), even the smallest domains engender staggering amounts of 3D finite elements. A partial solution has been implemented, which represents slender solid neighborhoods with non-manifold Boolean union of 1-manifolds (curves) and/or 2-manifolds (surfaces), added with thickness information, called 1.5D and 2.5D models, respectively. Automatic applications of these techniques requires the estimation of the medial axis of the porous media, to produce a truss or frame FEA. Previous works require explicit synthesis of

the skin of the porous domain. This manuscript presents an alternative in which the medial axis and thus the 1.5D (truss) representation of the porous domain is directly obtained from the scalar field (i.e., Computer Tomography -CT-) of the domain, thus avoiding the explicit calculation of the domain skin. The manuscript also presents the noise removal and linearization of the medial axis data, to obtain the skeleton truss graph (including bar radii), that represents the porous domain. Shear and tension load simulations are conducted with the Truss model, showing that the generated model can be used in FEA software. Future work is required in extending this concept to lattice materials, where the medial axis includes surfaces and not only curves, as in this manuscript.

4.3   Introduction

Porous and lattice materials (e.g. foams) are particularly important in aerospace, medicine, additive manufacturing, etc. The geometric modeling of such materials presents intractably large data sets. This circumstance, in turn, hinders computations, behavior assessments, and design. In the particular domain of open pore materials, it is possible to use a Truss or Frame modeling (called 1.5D modeling) to study reasonable sized domains, which would be expensive to model and simulate, in terms of human manual work time and computational cost, by using full Boundary Representation (3D BReps).

Computer Tomography (CT) is a common method to sample foam or reticular materials. CTs basically produce a discrete scalar function $f : \mathbb{R}^3 \to \mathbb{R}$ that characterize the space occupancy of the open pore material. In CTs, f is presented in form of voxel (Volumetric Pixel) sets. Previous mechanical truss modeling of open pore materials ([34]) takes CT as input, and explicitly produces the iso-surface $\partial B \ f(p) = c$ which bounds the solid material B. Then, the skeleton of $\partial B \ (SK(B))$ is computed. Finally, $SK(B)$ is used to define the Truss graph, which is the input to FEA methods to compute stress - strain models of B.

The present manuscript presents a method to avoid the explicit calculation of the skin ∂B to compute the skeleton $SK(B)$. Our method estimates $SK(B)$ directly from the scalar field f. An intermediate step is to estimate the Medial Axis of B, $MA(B)$. This medial axis $MA(B)$ presents a number of degeneracies which must be corrected before $SK(B)$ can be estimated in the form of a truss graph and used to model the material. This manuscript presents such a cleaning process.

This manuscript also presents an application of the direct f - to - $SK(B)$ skeleton extraction, in the particular area of strain - stress computation. The Truss model of an open pore material is then used for a FEA mechanical simulation, showing that the simplified truss representation obtained from the scalar field is a viable alternative to 3D Brep - based FE models.

Fig. 4.2(a) shows a portion of a porous material which in a large extent accepts a characterization in the form of a truss or frame, built with fastened struts or limbs.

Fig. 4.2(b) conveys the fact that the limbs have skeletons, which are curves c_i and have a local radius at each point of the curves. The curves meet in general in non-manifold nodes, as more than 2 curves are incident to them. Nodes with n curves incident to them are loci of the *Star-n (Sn)* type.

However, this example contains a non-processed subset (marked with a rectangular window), whose skeleton is a surface, and not a curve. In this manuscript, we assume that the foam material contains no such wall - like portions. A formalization of this discussion follows.

k-manifold. A set M in $\mathbb{R}^n$ is said to be k-manifold if for every point $p \in M$, there exists $\delta > 0$ such that for all radius $0 < r < \delta$, the set $M \cap Ball(p, r)$ is homeomorphic to an open disk in $\mathbb{R}^k$

([35]), where $Ball(p, r)$ is an open ball centered at p with radius r. Informally speaking, 1-manifolds are curves and 2-manifolds are surfaces, with no self-intersections in both cases.

Open Pore Materials. These structures contain spaces empty of material, or cavities, which are all connected.
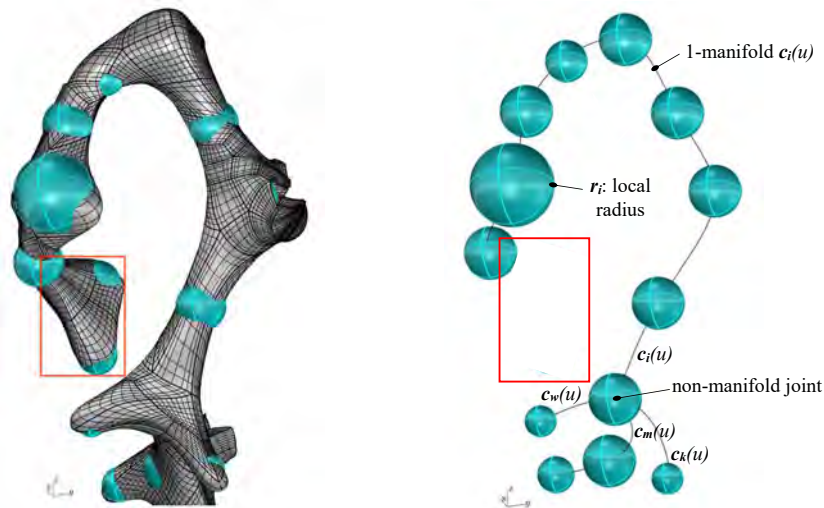
(a) Point set Skin ∂B and Tangent Balls.

(b) Skeleton from Solid in Fig. 4.2(a). Limbs are formed by curves (e.g. $c_i(u), c_w(u), 0 \leq u \leq 1$) and local radius r_i.

Figure 4.2: Porous Material with mostly 1D skeleton. Materials containing a 2D skeleton (see rectangular window) are not in the scope of this work.

Medial Axis. Given a 2-manifold smooth closed surface ∂B which bounds a solid B, the medial axis of ∂B, $MA(B)$ (Fig. 4.2(b)), is the set of all voxels v that are centers of balls $Ball(v, r)$, centered in v with some radius $r > 0$ such that each ball $Ball(v, r)$ is tangent to ∂B in exactly 4 points.

Skeleton. Is the graph of voxel centers with the same connectivity as $MA(B)$. It may be considered as the wire version of $MA(B)$. Each point of $SK(B)$ contains the mass transferred to it by the mass conservation strategy in the iterative thinning of B.

Truss Graph. The bar + node representation of $SK(B)$, with the radii and dimensions of bars and nodes being determined by the mass information present in $SK(B)$. The Truss graph includes kinematic and torque restrictions required to mimic joints of the physical equivalent frame.

Star-n sets in $\mathbb{R}^2$. A *star-n* (Fig. 4.3) in this manuscript refers to an open set of points $p \in \mathbb{R}^2$, which is the Boolean union of $n = 2, 3, 4, ...$ straight line segments. Each segment contains the origin in one end, and is open in the other end (Fig. 4.4).

Bar Pore Material. A *bar pore material* B is the set of points $p \in \mathbb{R}^3$ whose medial axis $MA(B)$ is composed by either (a) finite points in B whose neighborhood in B is homeomorphic to a star Sn with $n > 2$, or (b) infinite points in B, whose neighborhood in B is homeomorphic to $S2$.

The point set B whose boundary ∂B is shown in Fig. 4.2(a) is not a bar pore material because

47
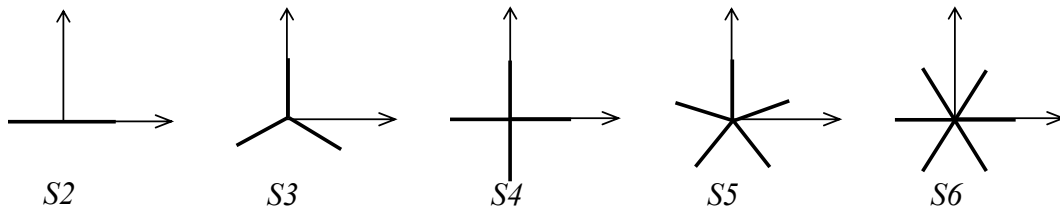
S2 *S3* *S4* *S5* *S6*

Figure 4.3: Open point sets Star-n, $S2$, $S3$, $S4$, $S5$, $S6$ in $\mathbb{R}^2$. Note: Sn sets are open as they exclude the branch ends. The term *open* set star has no relation with *open* pore.

the portion in the rectangular window has medial axis which is 2-manifold (surface) and not 1-manifold (curve).

This manuscript refers to Bar Pore Materials and it is organized as follows: Section 2 reviews the relevant State of the Art. Section 3 explains the applied methodology. Section 4 presents the results of the implementation used and its application. Section 5 concludes the manuscript and suggests domains for future work.
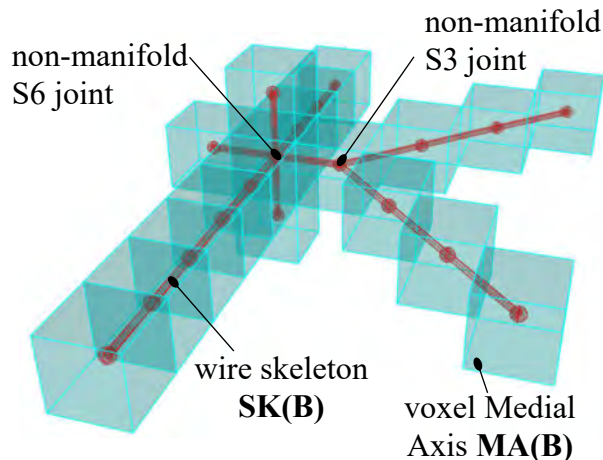
Figure 4.4: Voxel Medial Axis $MA(B)$, wire skeleton $SK(B)$, S3 and S6 non-manifold star joints.

4.4 Literature Review

First, a recent survey on the state of the art in skeletonization by [36] is discussed. Then, focus is made on (a) contraction and (b) thinning methods. Finally, skeletonization of foams is discussed.

4.4.1 Skeletonization algorithms

Skeletonization provides an effective and compact representation of an object by reducing its dimensionality to a *medial axis* or *skeleton* while preserving the topological and geometrical properties of the object [37]. For a 3D solid, a skeleton could be a surface skeleton (2D) or a curve skeleton (1D).

We are interested in objects with 1D skeletons because they allow simplification and acceleration [36] of the FEA problems.

The most common methods for computing analytical curve skeletons are: (a) Medial Surface - based, (b) Contraction methods, and (c) mesh decimation methods. The Medial Surface - based methods consist of identifying curves on the surface skeletons. Such methods are highly expensive [36] as they require accurate computation of geodesics between all points in a surface skeleton [38].

Contraction methods establish a shape evolution from the shape boundary to the curve skeleton [39]. Another contraction method is the discretization of the mean curvature flow in differential geometry. This method traces the surface-area loss through time steps [40].

Mesh decimation methods use iterative edge collapse on a triangle mesh [41] to converge towards the skeleton. However, the result is not necessarily smooth or centered, according to [36].

Curve skeletons from CT. For Computer Tomography scalar fields, contraction methods are directly applicable since they work on voxels. Refs. [42, 43] present algorithms where voxels are removed from the object boundary (skin) while preserving connectivity. A method to classify voxels that can be removed is described in [44, 45]. It must be noticed that, in contraction methods, the order of voxel removal (thinning order) severely affects the final result [46]. Ref. [47] presents a divergence - driven thinning that uses a sorted heap to ensure the correct processing order. Ref. [46] uses a voxel density order to prevent the jagging in the curve medial axes. This reference also presents a scalar attribute of the surviving voxels. At each evolution step, the scalar represents the mass of the voxels that have been removed, being this mass transferred to the surviving voxels. However, the mass of the whole domain cannot be retrieved from the final skeleton.

4.4.2 Models from Porous Materials

The generation of geometric models of foam microstructure and properties can be classified into (a) statistically generated models and (b) models from physical samples, as in [34].

Statistically generated models. They characterize complex solid geometry by using its morphological parameters[48]. The approaches generate typical structures, with statistical variations, spanning a large domain by using pre - defined local arrangements. Used methods are: (a) arrays of identical cells (e.g. kelvin cells [49]) or (b) stochastic approaches such as Voronoi tessellations, ellipsoid overlapping, etc [50]. In any case, all methods aim to generate a geometry and topology that mimics typical physical specimens. It is difficult for these methods to grasp the large variation in cell sizes and shapes [51] and manufacturing defects of physical samples. If 3D full Breps are generated, the 3D meshing and simulation processes may not converge due to factors such as data size, data quality, and even software license constraints (as reported in [34]). In this case, the relevance of the present manuscript (direct skeletonization from CT data) is evident.

Table 4.1: Literature Review summary.

Approach	Refs.	Advantages	Disadvantages
Foam models from physical specimens.	[10, 34, 52–54]	- Preservation of geometry and topology of the original sample. - Efficient computing of stress - strain models of foams using Truss graphs [34].	- Computing- and labor-expensive Breps required. - Expensive Full 3D FEA required.
3D characterization of simple points for thinning algorithms.	[44, 45]	- Calculation of the number of holes or genus not required.	- The proposition given to classify a simple voxel is correct, but the proposed pseudo-code in Ref. [44] may misclassify a simple voxel v as non-simple.
Volume contraction using thinning orderings.	[46, 47]	- Thinning orderings for diverse applications. - [46] keeps track of the mass of voxels in the surface. - Surface or curve skeleton available through additional computation.	- Portion of initial mass of B missing in skeletonization [46]. - Disconnection in the curve skeleton topology [46]. - Boundary of the contracting shape not explicitly available in Ref. [47].

Models from Physical Specimens. Physical specimens from foams, porous or reticular materials are usually sampled using micro-computed tomography (mCT). The 3D scalar field of such scans is expressed in voxel arrays with resolutions around 0.5 microns and domain sizes in the cm range [55]. Full 3D modeling from these samples may be conducted by either keeping the voxel set B, or computing a smooth boundary (skin) of B, ∂B. FEA simulations and visualizations are then conducted [10,52–54]. The full 3D modeling is very precise and faithful to the physical sample. However, it is intractable for even the smallest cm-range samples, due to the staggering amount of data and labor required. Computing of smooth BReps from scalar fields is typically achieved by variations of the Marching Cubes algorithm [56], followed by intensive human labor in correcting the violations to 2-manifold properties that are common in triangle meshing. After the BRep is obtained, the FEA 3D meshing and computing may not converge even with small domains.

Ref. [34] uses as input a correct BRep, ∂B of the porous domain. It produces a Truss graph representation of the strut frame implicit in ∂B. The Truss representation is then analyzed with finite elements, taking advantage of the so called *1.5D* finite elements, which are 1-dimensional ones equipped with local diameter (i.e. rods). This work shows important advantages from the Truss (i.e. 1.5D) over the full 3D models, showing that the truss model is less computationally expensive to simulate and that it can render reasonable strain - stress results. The method also has shown a good preservation of the porosity (ratio of empty to total volume) of the real sample with the Truss model.

4.4.3 Conclusions of the Literature Review

The main advantages and disadvantages of the surveyed methods are summarized in Table 4.1.
The contributions of this manuscript, with respect to the existing methods are:

1. Synthesis of the Truss graph directly from the Voxel scalar field B, without passing by the computing- and labor - expensive skin ∂B. Notice that this is an important advantage with respect to [34], where a smooth, watertight, manifold, high-quality triangular mesh is required to obtain the medial-axis using the Mean Curvature Flow approach reported in [57].

2. To achieve (1), we use and improve on [46] in the following aspects:

   (a) Our algorithm keeps precise track of the mass of the initial solid B. Each voxel of the final Medial Axis $MA(B)$ accounts for representing a quantified contribution to keep the initial mass. This feature permits a precise estimation of the local radii along the struts of the Truss graph.

   (b) Our algorithm conserves hanging branches of B for the purpose of representing their medial axis.

   (c) Our algorithm avoids possible disconnections in the curve skeletons that may occur in [46].

3. We illustrate an application of the synthesized Truss graph in mechanical (stress - strain) computations.

4.5 Methodology

In this section we present the implemented method to estimate a truss graph simplification from the skeleton $SK(B)$. We use as input the CT of the sample, expressed as a scalar field f in the form of voxels. In Section 4.5.1, we calculate the medial axis of B ($MA(B)$), which contains information about the mass of B. Then, in Section 4.5.2, we use $MA(B)$ with the mass information to find a truss graph simplification of B, which is well suited to model bar pore materials.

4.5.1 Medial Axis from Scalar Field Extraction

Algorithm 1 displays the main features of the extraction of the voxel Medial Axis from the domain B (voxels from the CT scan). Our algorithm is inspired in the boundary density transport approach of [46].
In the line 3, the `superfluous` set is chosen, which is composed of voxels in the boundary ∂B which (a) do not change the voxel set connectivity when missing (i.e. *simple voxels* [44, 45]), and (b) participate of a 1-manifold violation. We add the condition (b) to avoid that the medial axes of hanging branches disappear. Voxels which do not change connectivity but belong to a hanging branch are not `superfluous`. This is an important difference with previous methods (e.g. [46]), where 1-manifold wires are considered only if they have received a large amount of mass from the boundary voxels. Since, by definition, every voxel of a hanging or dead-end branch does not change connectivity of the set, using only connectivity as elimination criterion would lead to the whole dead-end branch to be eliminated. Condition (b) above forces to eliminate only voxels of such branches which additionally violate 1-manifoldness. Line 4 indicates that the iteration stops when

---

Algorithm 1: Extraction of Medial Axis from Scalar Field (CT).

1: **procedure** MA = FIELD_TO_MEDIAL_AXIS(B : voxel set)
2:     ∂B = boundary(B)
3:     superfluous = find_simple(∂B)
4:     **while** superfluous $\neq$ [ ] **do**
5:         v = first(superfluous)
6:         n = inner_normal(∂B, v)
7:         N(v) = neighbors(∂B, v, n)
8:         mass(N(v)) = mass(N(v)) + mass(v)
9:         superfluous = superfluous $-$ {v}
10:        ∂B = update(∂B, v)
11:        superfluous = update(superfluous, ∂B, v)
12:    **end while**
13:    MA = ∂B
14: **end procedure**

---

only essential voxels remain in B. Line 5 chooses for elimination a voxel in the `superfluous` set which has a minimal value of accumulated mass in it. Line 6 computes the inner pointing vector normal n to the skin ∂B at v using a gradient estimation (Neumann et al [58]). Line 7 identifies the 26-neighborhood N_{26} [44] associated with the voxel v to delete.

(a) Medial Axis with Noise (hairs).   (b) Medial Axis without Noise.
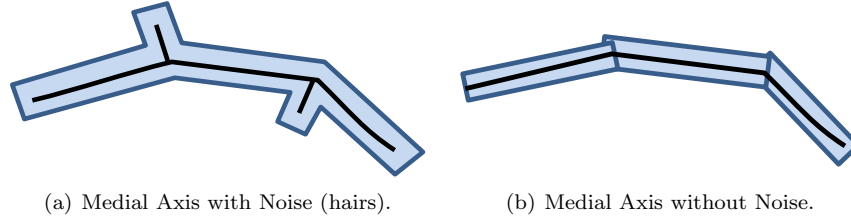
Figure 4.5: Hair removal from the Medial Axis $MA(B)$.

(a) Large Linearization Error.   (b) Small Linearization Error.
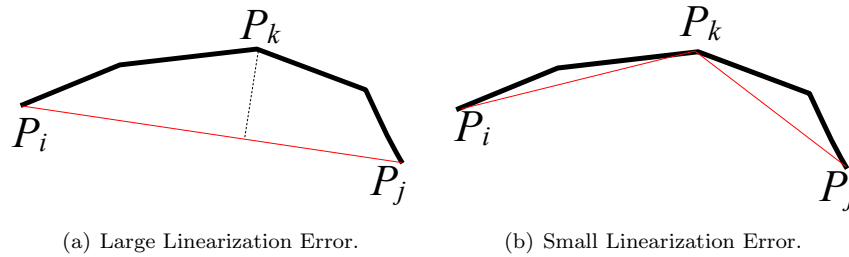
Figure 4.6: Recursive subdivision to obtain a small linearization error from $MA(B)$.

Line 8 transfers the mass of voxel v to its neighbors in direction n, using diffusive advection

(Jalba et al. [46]). In this approach, the major receptor of mass is the voxel in the neighborhood of v that occupies the n direction. The other voxels in the neighborhood of v also receive minor proportions of the v mass. At this time the mass associated to v is null (fully transferred to its neighbors). In lines 9 and 10, voxel v is eliminated from the **superfluous**, B and ∂B sets. Now, the boundary ∂B is updated around v. Line 11 recomputes the B connectivity since the absence of v changes it. Thus, the **superfluous** voxel set must be updated.

When the **superfluous** voxel set is empty, $B = \partial B = MA(B)$. Line 13 recognizes this fact.

(a) 3 - cycle in Medial Axis.   (b) 3 - cycle eliminated from Medial Axis.
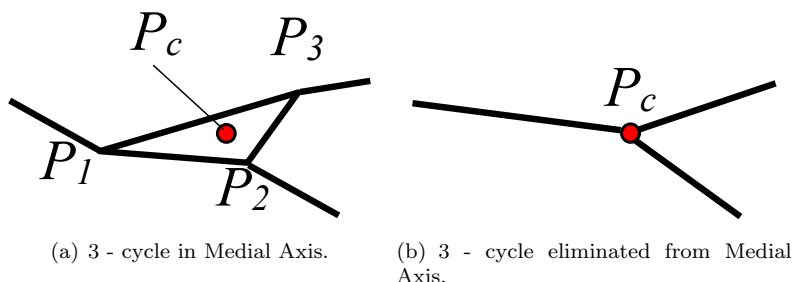
Figure 4.7: Elimination of 3-cycles from $MA(B)$.

Algorithm 2: Conversion from the Medial Axis $MA(B)$ into the Truss Graph (V, E)

1: **procedure** [V, E] = MEDIAL_AXIS_TO_TRUSS(MA : Medial Axis Graph)
2:     MA = hair_removal(MA)
3:     MA = edge_linearization(MA)
4:     SK = cycles_removal(MA)
5:     [V, E] = radii_estimation(SK)
6: **end procedure**

4.5.2   Truss Graph from Medial Axis

The Medial Axis $MA(B)$ obtained from the thinning algorithm in Algorithm 1 contains several characteristics, which make it useless as skeleton for a Truss graph (Fig. 4.9(a)). These features are: (1) high level of noise that manifests in small dead-end paths (hairs), (2) oscillations and high curvatures in the node - to - node paths, and (3) irreducible cycles of 3 edges (3-cycles). Algorithm 2 presents a description of the procedure to obtain the Truss graph from the Medial Axis. Steps 2-4 outline the cleaning of $MA(B)$ by removing features (1)-(3). Then, the mass information is used to produce the truss graph.

To advance towards a Truss graph, noise in the form of hairs must be removed (Fig. 4.5). The short excursions or short dead-end paths are removed. An excursion is classified as *short* if its length is smaller than a given parameter L. In this work, L is equivalent to the biggest value of the Transform of Euclidean Distance [59] from $MA(B)$ to the original skin of B (∂B).

Once the hairs have been suppressed, it is necessary to execute a linearization of the resultant medial axis to eliminate oscillations and high curvatures in the node - to - node paths. The high level of noise in Fig. 4.6(a) is removed by replacing quasi linear paths with a straight edge. If the path

53
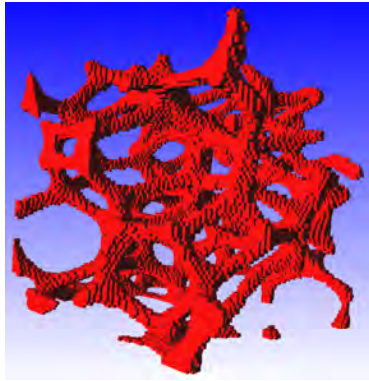
(a) Domain 1. Scalar Field Expressed in Voxels.
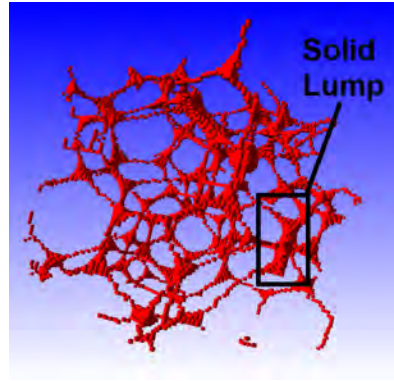
(b) Domain 1. Intermediate Medial Axis.
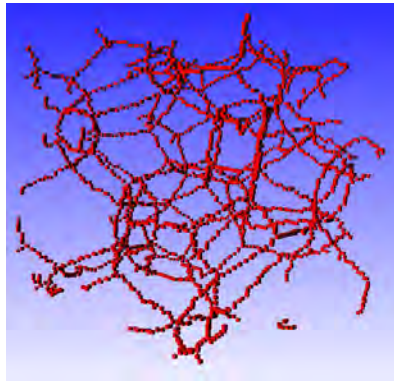
(c) Domain 1. Medial Axis Expressed in Voxels.
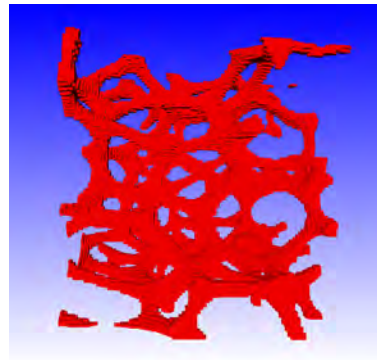
(d) Domain 2. Scalar Field Expressed in Voxels.
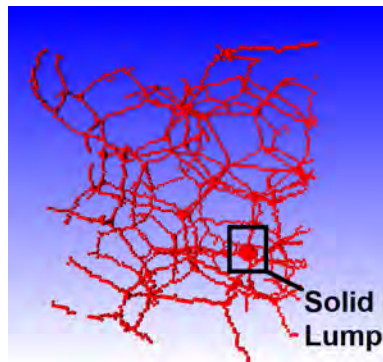
(e) Domain 2. Intermediate Medial Axis.
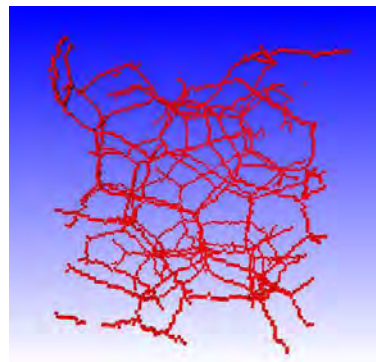
(f) Domain 2. Medial Axis Expressed in Voxels.

Figure 4.8: Voxel - based Scalar Field and its Medial Axis. Data Sets 1 and 2

deviates in significant manner (Fig. 4.6) from a straight one, a recursive subdivision is conducted until each linear edge does not deviate more than a threshold P from its curved equivalent. We have taken $P = 0.2$, which means that the polyline can deviate at most 20% from the straight line.

Irreducible cycles of 3 edges (3-cycles) appear in the wireframe Medial Axis $MA(B)$ (Fig. 4.7). They are removed by replacing vertex points p_1, p_2 and p_3 in Fig. 4.7(a) by the barycenter of the triangle p_c in all relevant graph topology. After the 3-cycles are suppressed, the skeleton $SK(B)$ is obtained.

Wire connectivity in $SK(B)$ is used in conjunction with the mass information to produce a truss graph $[V, E]$ (e.g. Figs. 4.9(c), 4.9(g)). Elements in V and E are assumed to be spheres and cylinders, respectively. Finally, we estimate the radius of each element in V and E by using its geometric and mass data, as shown in step 5 of algorithm 2.

4.6 Results

Section 4.6.1 shows the result of the application of Algorithms 1 and 2 to two different samples, and gives a comparison of the porosity (a characteristic parameter for porous media) between the Truss graph and the initial shape. Section 4.6.2 shows an example in which the Truss graph approximation can be used to generate relevant mechanical simulations.

4.6.1 Truss Representation of Voxel Sets

Fig. 4.8 presents an initial voxel - based scalar field and an intermediate result of the Medial Axis extraction (Algorithm 1). It is relatively simple to detect that the thinning has not finished since Figs. 4.8(b) and 4.8(e) show solid lumps of voxels still present. These lumps are in violation of 1-manifold or Sn (Fig. 4.3) conditions. Figs. 4.8(c) and 4.8(f) show the final medial axis representation, which in all neighborhoods presents 1-manifold or Sn conditions.

Fig. 4.9 presents aspects of the processing of a medial axis $MA(B)$ to convert it into a usable skeleton $SK(B)$ and then into a Truss graph representation of B (Algorithm 2). The medial axis is usually very noisy (Fig. 4.9(a)), containing hairs, irreducible triangular cycles, and strongly curved struts. Figs. 4.5, 4.6 and 4.7 intuitively explain the hair removal, recursive linearization and 3-cycle elimination, respectively. The result is a clean linearized skeleton $SK(B)$, as presented in Fig. 4.9(b).

Fig. 4.9(c) presents the equivalent Truss Graph (V, E). In this graph, the nodes in V contain information about their (x, y, z) position in $\mathbb{R}^3$ and the equivalent radius of an envelope sphere that represents the material accumulated in the Sn joints. The edges in E contain information of their end vertices as well as the equivalent cylinder radius, as per the accumulated mass $m(v)$ of the surviving voxels in $MA(B)$. The radii associated with the Sn joints are not used in this manuscript, but are relevant to the void vs. full space ratio (i.e. porosity) of the material. Fig. 4.9(d) contrasts the initial (voxel) scalar field against its Truss graph approximation.

In order to get a measure of the quality of the truss graph approximation, the porosity (or void fraction) of the initial samples is compared with the porosity of their respective truss approximations (Table 4.2). The reader may notice that, for both samples, the difference of the porosity between the actual and the truss approximated domain is lower than 1%.

(a) Domain 1. Wireframe Noisy Skeleton.

(b) Domain 1. Wireframe Clean Linearized Skeleton.

(c) Domain 1. Truss Graph Approximation.

(d) Domain 1. Voxel Set and its Truss Graph Approximation.

(e) Domain 2. Wireframe Noisy Skeleton.

(f) Domain 2. Wireframe Clean Linearized Skeleton.

(g) Domain 2. Truss Graph Approximation.

(h) Domain 2. Voxel Set and its Truss Graph Approximation.
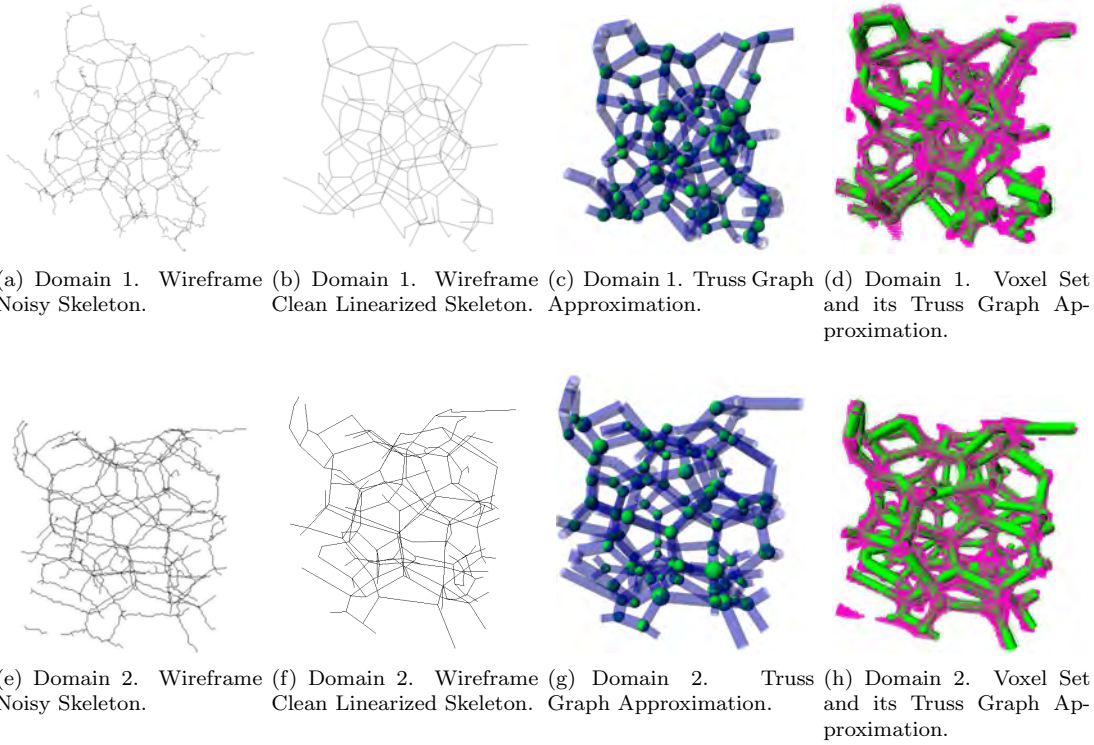
Figure 4.9: Process of Approximation of a Voxel Set by a Bar / Sphere Graph. Data Sets 1 and 2

Table 4.2: Comparison of the Porosity of the Actual Samples vs. the Porosity of the Truss Approximation.

Domain	Actual porosity	Truss graph's porosity	Relative error
Domain 1	93.90%	94.01%	0.12%
Domain 2	93.32%	93.30%	0.02%

4.6.2 Application on Open Pore Stress - Strain Calculation

This section presents a proof - of - concept in the sense of showing that the Truss graph approximation of a voxel scalar field is indeed advantageous for relevant mechanical analyses . The particular example domain chosen is the stress - strain behavior of the porous material, as computed with Finite Element Analysis (FEA).

(a) Shear Test Conditions.

(b) Tension Test Conditions.
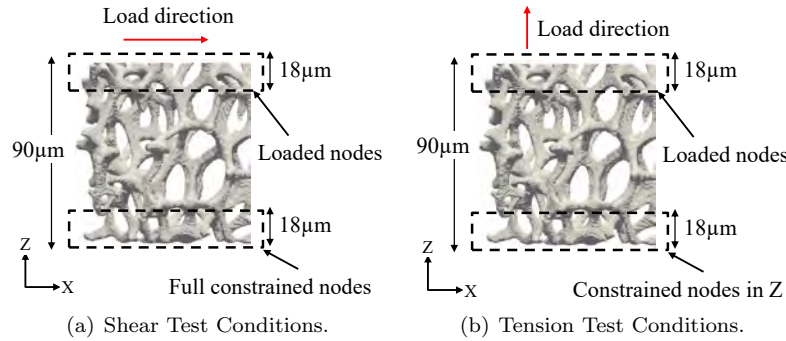
Figure 4.10: Boundary Conditions for the Mechanical Tests.

(a) Shear Deformation in X direction.

(b) Tension Deformation in Z direction.
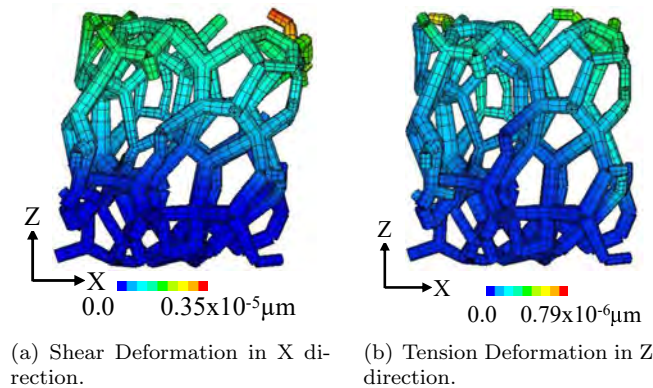
Figure 4.11: Shear and Tension FE Analyses with Truss model. Displacement scales are augmented by the FEA software for visualization.

In order to gain some insights on the computational savings of the Truss model against other traditional models, we have analyzed the Porous Domain 1 by generating two case studies of shear and tension loads (Fig. 4.10) for the corresponding (a) 3D voxel - based model and (b) Truss - based model. The 3D voxel - based model is generated by converting every Voxel into a hexahedral (cubic) element. Despite this technique does not represent the geometry of the domain with the same fidelity as a BRep model, it has been used for multiple studies of the mechanical response (estimation of apparent mechanical properties) of porous materials ([4, 60]).

The results of the simulations are shown in Figs. 4.11 and 4.12. These figures are generated using a feature of the FEA software which allows to exaggerate the deformation for visualization

(a) Shear Deformation in X direction.

(b) Tension Deformation in Z direction.
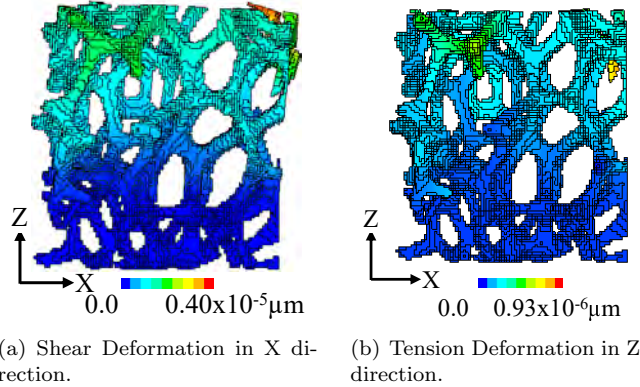
Figure 4.12: Shear and Tension FE Analyses with the Voxel Model. Displacement scales are augmented by the FEA software for visualization.

purposes. Taking the maximum displacements of the Voxel model as reference values, the error of the Truss model in the estimation of X displacements in the shear test is 12.5%. In a similar fashion, the error in the estimation of Z displacements in the tension test is 15.1%.

Table 4.3 compares the FEA resources devoted to Voxel - based model vs. Truss - based simulations. The saving factor in all categories (FE nodes, elements, equations and memory) in favor of Truss graph data is in the order of 10^2. To determine how such saving factor impacts the computing time, we recur to the order of growth O of the execution time in terms of the number of nodes. In the worst-case scenario, the bandwidth of the stiffness matrix is $O(N^2)$, where N is the number of nodes. Hence, the time complexity of a FEA simulation is given by the term $O(N^3)$ ([61]). Then, a difference of 10^2 in the number of elements, implies a difference in the order of 10^6 in the number of operations that need to be performed to simulate the models.

Table 4.3: Computing Expenses for Truss vs. Voxel - based Foam Models.

Model	Number of Nodes	Number of Elements	Number of Equations	Memory allocated by Solver
Truss	729	786	3450	1.8MB
Voxel	95390	61039	230676	628.4MB

4.7   Conclusions

This manuscript presents a method to directly synthesize a truss graph representation from the scalar field (voxel CT) of an open pore material domain B. This approach is an alternative to previous ones which first require the estimation of the skin or Boundary representation ∂B. The implemented method enforces the conservation of volume information of each original domain bar, thus allowing to estimate the radii of the equivalent truss bars. The method implemented estimates the medial axis of the domain B, removes the noise (inherent to medial axes) and linearizes the

local geometry. FEA computations are presented with the Truss model obtained from the scalar field, showing that it is a viable alternative to the 3D BRep - based models, which are much more expensive to generate and simulate.

Future work is required in porous or lattice domains whose medial axis includes surfaces (and not only curves). Additional work is needed in comparing the 1.5D Truss vs. 3D Brep simulations (considering the 3D one as ground truth). Also, experimental work is needed with actual porous material samples, to contrast the equivalent mechanical parameters estimated with the simulations vs. the laboratory values.

Acknowledgments

Chapter 5

A General Meta-graph Strategy for Shape Evolution under Mechanical Stress

Diego Montoya-Zapata[1,2], Diego A. Acosta[3], Oscar Ruiz-Salguero[1], Jorge Posada[2], David Sanchez-Londono[1]

[1] Laboratory of CAD CAM CAE, Universidad EAFIT, Medellín, Colombia.
[2] Vicomtech, Spain.
[3] Grupo de Desarrollo y Diseño de Procesos (DDP), Universidad EAFIT, Medellín, Colombia

5.1 Context

5.1.1 Proof of Publishing

The article *FEA Structural Optimization Based on Meta-graphs –Diego Montoya-Zapata, Diego A. Acosta, Oscar Ruiz-Salguero, David Sanchez-Londono* was presented in the "13th International Conference on Soft Computing Models in Industrial and Environmental Applications (SOCO 2018)". It was published as a chapter of the Springer book series Advances in Intelligent Systems and Computing (AISC) (Fig. 5.1).

The 13th International Conference on Soft Computing Models in Industrial and Environmental Applications
SOCO'18-CISIS'18-ICEUTE'18 2018: International Joint Conference SOCO'18-CISIS'18-ICEUTE'18 pp 209-220 | Cite as

FEA Structural Optimization Based on Metagraphs

Authors   Authors and affiliations

Diego Montoya-Zapata, Diego A. Acosta, Oscar Ruiz-Salguero ✉ , David Sanchez-Londono

Conference paper
First Online: 07 June 2018

153
Downloads

Part of the Advances in Intelligent Systems and Computing book series (AISC, volume 771)

Log in to check access

Buy eBook
EUR 178.49

Buy paper (PDF)
EUR 30.19

- Instant download
- Readable on all devices
- Own it forever
- Local sales tax included if applicable

Learn about institutional subscriptions

Cite paper ▾

Abstract

Evolutionary Structural Optimization (ESO) seeks to mimic the form in which nature designs shapes. This paper focuses on shape carving triggered by environmental stimuli. In this realm, existing algorithms delete under - stressed parts of a basic shape, until a reasonably efficient (under some criterion) shape emerges. In the present article, we state a generalization of such approaches in two forms: (1) We use a formalism that enables stimuli from different sources, in addition to stress ones (e.g. kinematic constraints, friction, abrasion). (2) We use metagraphs built on the Finite Element constraint graphs to eliminate the dependency of the evolution on the particular neighborhood chosen to be deleted in a given iteration. The proposed methodology emulates 2D landmark cases of ESO. Future work addresses the implementation of such stimuli type, the integration of our algorithm with evolutionary based techniques and the extension of the method to 3D shapes.

Keywords

Topology optimization   Evolutionary structural optimization   Mathematical graph

Figure 5.1: `FEA Structural Optimization Based on Metagraphs` presented in SOCO 2018. Screenshot of the AISC Book Series, Springer.

The was selected for the organizers of SOCO 2018 to be extended and submitted to an Special Issue in the Journal Cybernetics and Systems, Taylor & Francis. Figure 5.2 depicts a proof of the submission of the improved article to the Journal Cybernetics and Systems.

In order to simplify this document, only the version of the article submitted to the Journal Cybernetics and Systems is added into the text. The reader may consult the article presented in SOCO 2018 in the Springer web page. See the corresponding bibliographic information in Section 5.1.

Figure 5.2: Proof of Submission to Special Issue in Journal of Cybernetics and Systems.

5.2 Abstract

The challenges that a shape or design stands are central in its evolution. In the particular domain of stress / strain challenges, existing approaches eliminate under-demanded neighborhoods from the shape, thus producing the evolution. This strategy alone incorrectly (a) conserves disconnected parts of the shape, and (b) eliminates neighborhoods which are essential to maintain the boundary conditions (supports, loads). The existing analyses preventing (a) and (b) are conducted in an ad-hoc manner, by using graph connectivity. This manuscript presents the implementation of a

meta-graph methodology, which in systematic manner lumps together finite element subsets of the current shape. By considering this meta-graph connectivity, the method impedes situations (a) and (b), while maintaining the pruning of under-demanded neighborhoods. Research opportunities are open in the application of this methodology with other types of demand on the shape (e.g. friction, temperature, drag, abrasion).

5.2.1 Keywords

Topology optimization, Evolutionary structural optimization, Mathematical graph

Glossary

AM:	Additive manufacturing.
BESO:	Bidirectional evolutionary structural optimization.
ESO:	Evolutionary structural optimization.
FEA:	Finite element analysis.
GA:	Genetic algorithms.
Ω_0:	Compact and bounded subset of $\mathbb{R}^2$, that represents an initial material stock from which to carve the part.
Ω_i:	The part after the i-th step of the evolution.
f:	Scalar function $f : \Omega_i \to \mathbb{R}$ that expresses how much is the neighborhood of a point $x \in \Omega_i$ being demanded by the stimuli (e.g. stress) being considered.
g:	Scalar function $g : \Omega_i \to \mathbb{R}$ that expresses the permissible level of demand f that the neighborhood of a point $x \in \Omega_i$ may stand (e.g. permissible stress allowable). In mechanical design, g is usually a constant for the whole domain Ω_i.
$G = (V, A)$:	the Finite Element - based graph in which a vertex $v_i \in V$ is a finite element. An arc $(v_i, v_j) \in A$ means that finite elements v_i and v_j are neighbors.
$G_M = (V_M, A_M)$:	A meta-graph built on G, in which a meta-vertex $V_i \in V_M$ is a connected set of finite elements of V. A meta - arc $(V_i, V_j) \in A_M$ means that meta-vertices V_i and V_j are neighbors.

5.3 Introduction

As a result of the process of evolution, natural shapes lose the neighborhoods that do not affect their basic functions. This evolutionary process is influenced by the different stimuli (heat, friction, stresses) to which the shape is subjected to.

Based on the response of the shape to the different stimuli, one can classify the shape neighborhoods as (1) demanded, if they are highly used to fulfill the functional requirements, or (2) under-demanded, when they are not completely necessary.

This work presents a methodology for structural optimization in which the exact nature of

the stimulus may be generic. At the same time, the criterion of material removal may be also generic. Examples of such a criterion are low stress, high exposure to friction, maximization of wave reflection (e.g. sound), etc. In this particular article, the material removal obeys to low stressed neighborhoods when subjected to stress / strain stimuli. Notice that, once the stimuli are calculated (by specialized outsourced software), the particular criteria for material removal can be applied in a generic manner.

This article presents a meta-graph methodology, which systematically removes material neighborhoods (represented by subsets of finite elements) of the current shape. By considering this meta-graph connectivity, the method prunes under-demanded neighborhoods while impeding the (a) generation of disconnections on the shape, and (b) elimination of the essential neighborhoods that maintain the boundary conditions (supports, loads).

This manuscript is organized as follows: Section 5.4 provides a review of the related literature. Section 5.5 describes the proposed meta-graph based algorithm and Section 5.6 presents and evaluates the results obtained following the meta-graph approach. Finally, Section 5.7 contains the conclusions and some possible research lines to extend this work.

5.4   Literature Review

5.4.1   Evolutionary Structural Optimization

Xie and Steven ([62]) introduce a structural optimization method called Evolutionary Structural Optimization (ESO). ESO removes progressively the low stressed portions of a structure by carrying out iterative FEA simulations. Therefore, the weight of the structure is reduced without affecting its functionality. Bidirectional ESO (BESO) [63] is an extension of ESO in which new material can be added in high-stressed zones. One of the main drawbacks of ESO and BESO is the formation of non-valid configurations as a result of material removal, which cause the end of the optimization process.

Recent publications on improvements of ESO/BESO techniques [64, 65] and on review articles focused on ESO/BESO [66–68] prove that the development of these algorithms is a matter of interest for the academic community.

One of the reasons of the popularity of ESO and BESO is the wide range of engineering problems that can be addressed with these methods. Some examples are: aeronautics [69], biomedicine [70], and materials design [71].

Likewise, much of the research efforts in topology optimization are focusing on additive manufacturing (AM) [72, 73]. The recent advances in AM allow the exploitation of the full capacities of ESO/BESO techniques. Hence, it is necessary to improve the current topology optimization algorithms so that they adapt to the manufacturing capabilities that have been gained because of AM.

5.4.2   Graphs Representations Used with ESO

Stojanov et al. ([74]) uses graphs to represent of FEA meshes, so that each graph vertex represents a FEA element. In this work, graphs are used to check the connectivity of the generated structures. Structures that do not meet the connectivity requirement are discarded. In a similar fashion, Munk, Vio, and Steven ([65]) use a graph-based connectivity checker to extend BESO.

In these two papers [65, 74] graph representations have been mainly used to find valid (or non-valid) configurations of FEA meshes while using ESO algorithms and when a non-valid configuration is found, this branch of the optimization process is not taken into account. Additionally, graphs abstractions are not integrated to the material removal process

Montoya-Zapata et al. ([75]) integrate ESO algorithm and graphs to perform 2D structural optimization. In their work, Montoya-Zapata et al. ([75]) develop a meta-graph (a graph generated from subsets of elements of the FEA mesh) strategy to be used as part of the material removal routine. However, this strategy is only used in a particular case, when the connectivity of the boundary conditions is compromised.

5.4.3 Graph Representations in Other Structural Optimization Algorithms

Graph representations have been used in conjunction with other structural optimization techniques, apart from ESO. For instance, Giger and Ermanni ([76]) focus on the topology optimization of trusses, using genetic algorithms (GA) as the basis of the algorithm to remove the useless material of the truss structure. Graph representations are mainly used to establish a criterion to test if a solution is structurally valid.

Another example of the use of GA and graph representations in structural optimization is presented by Madeira, Pina, and Rodrigues ([77]). In this work, each graph vertex represents a finite element, and a graph arc between two vertices indicates that the elements the vertices represent are neighbors. These graphs are created and modified using GA to find an optimal solution.

5.4.4 Conclusions of the Literature Review

Structural optimization and specifically ESO/BESO are topics of interest because of the multiple application fields in which they can be used. In particular, the use of topology optimization in AM is establishing as a necessity. Therefore, it is necessary to improve current topology optimization algorithms.

We have shown that the use of graph abstractions is common in structural optimization. However, graphs are mainly used to check the connectivity of the generated solutions and they are not integrated into the material removal algorithm.

This contribution intends to illustrate a methodology to use graphs to administrate the information of neighborhood and static connectedness to support the shape evolutionary strategy. The present paper proposes a generalization of the meta-graph based strategy presented by Montoya-Zapata et al. ([75]), so that it is used at every stage of the optimization process. In this way, the material removal algorithm is simplified and fully based on the meta-graph information (meta-graph connectivity and meta-nodes degree). In addition, this work presents additional examples to support and illustrate the behavior of our meta-graph based optimization approach.

We do not try in the present status of our manuscript to evaluate or apply alternative evolutionary strategies (e.g. mutation and crossover operators [76, 77]). Our future work seeks to widen the variety of stimuli (kinematics, abrasion, temperature) that drive evolution in the nature domain.

5.5   Methodology

5.5.1   Problem Statement

Given

1. Let $\Omega_0 \subset \mathbb{R}^2$ be a compact and bounded domain that represents an initial oversized domain.

2. A stimulus function S that acts over $\Omega_S \subset \Omega_0$.

3. FEA mesh $M_0 = (N_0, E_0)$ for Ω_0, where N_0 is the set of nodes and E_0 is the set of elements.

Goal

To obtain the design domain $\Omega_F \subset \Omega_0$ that solves the optimization problem:

$$\min_{\Omega} \quad A(\Omega)$$
$$s.t. \quad f(x) \leq g(x), \quad \text{for all } x \in \Omega, \Omega \subset \Omega_0$$
$$\Omega_S \subset \Omega$$

where $A(\Omega)$ is the area of Ω, $f(x)$ is the response for $x \in \Omega$ to the stimuli S and $g(x)$ expresses the permissible level of demand f that the neighborhood of a point $x \in \Omega_i$ may stand (e.g. permissible stress allowable).

5.5.2   Structural Optimization Algorithm

The implemented optimization algorithm follows the procedure described in Fig. 5.3(a). First, a FEA simulation is carried out, given the initial FEA mesh $M_0 = (N_0, E_0)$ and the stimulus function S. The FEA simulation allows to find the domain response f to the stimuli S. If f exceeds the permissible limit g, then the algorithm stops. Otherwise, the algorithm proceeds to delete the under-demanded FEA elements. The sub-algorithm that performs the deletion of the FEA elements is presented in Fig. 5.3(b). It is described in detail in Sect. 5.5.3.

Finally, another FEA simulation is performed with the resultant domain after the deletion of the under-demanded FEA elements deletion. The cycle is repeated until no more elements can be deleted.

The reader may notice that the algorithm presented in this article reduces Ω_0 by removing under-demanded material (i.e. elements from E_0) given a deletion criterion. The stimulus function S and the deletion criterion are user-defined properties and f is calculated by using FEA software. Therefore, the presented algorithm is independent to the kind of stimuli (forces, friction, abrasion, humidity, etc.) to which the domain is subjected.

(a) Work-flow of the optimization algorithm   (b) Element deletion sub-algorithm
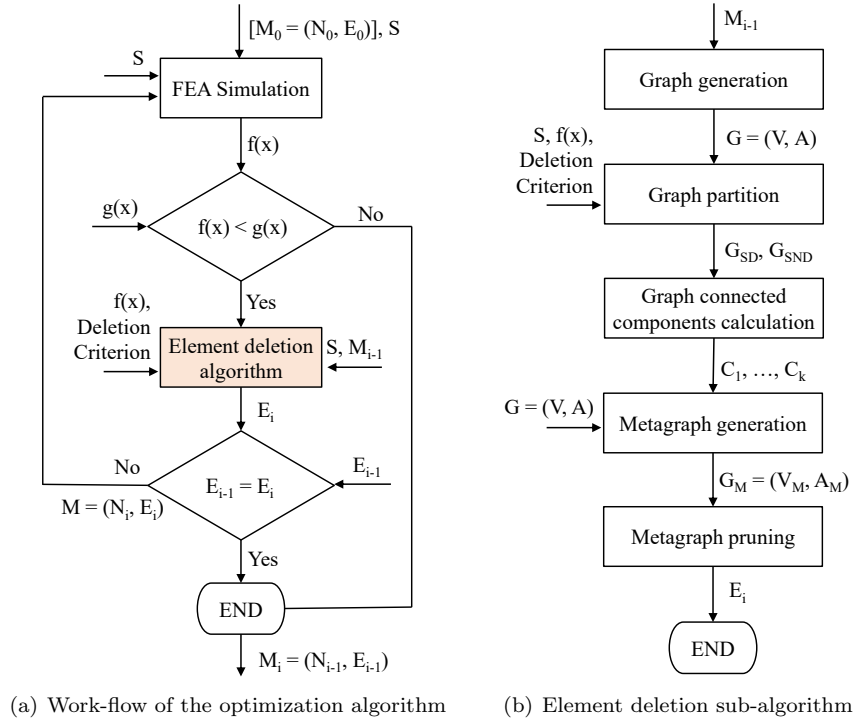
Figure 5.3: Data flow of the implemented optimization procedure.

5.5.3 Element Deletion Algorithm

The main objective of our element deletion algorithm is to assure that the resultant configuration (after removing the unnecessary FEA elements) is valid from a structural point of view. Our algorithm is based on a graph abstraction of the design domain, as presented in Fig. 5.3(b). The main stages of the algorithm are discussed in the following sections.

Graph Generation

For every FEA mesh $M = (N, E)$, a graph $G = (V, A)$ can be generated with the following procedure:

1. Assume that $E = \{e_1, e_2, \ldots, e_k\}$. Then, for every $e_i \in E$ create a graph vertex $v_i \in V$.

2. A graph arc $(v_i, v_j) \in A$ exists if and only if the corresponding FEA elements e_i, e_j are adjacent.

Different adjacency relations between elements can be defined for a 2D FEA mesh. In particular, in this article we consider two elements as adjacent if they have a common edge. In Fig. 5.4 is depicted an example of the graph associated to a FEA mesh following this FEA-edges adjacency rule.

(a) FEA mesh   (b) Graph edges produced by adjacent FEA edges
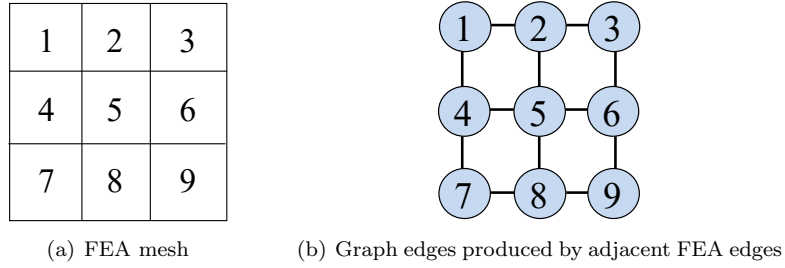
Figure 5.4: FEA mesh to graph conversion using FEA edge adjacency criteria.

Graph Partition

In order to carry out the elimination of the under-demanded material, the graph is partitioned into two sub-graphs G_{SD} and G_{SND} where: (i) G_{SD} contains the graph nodes that are candidates for elimination ($E_D \subset E$) and G_{SND} contains the rest of nodes ($E_{ND} = E - E_D$).

The set of nodes E_D are those nodes associated to the under-demanded FEA elements. These elements are selected based on the response function f and a *Deletion Criterion*. In our case, our *Deletion Criterion* is defined by an admissible limit for the Von Mises stress at each optimization stage. In addition, the FEA elements in which the stimulus function S acts cannot be eliminated, so they always belong to E_{ND}.

Connected Components Calculation and Meta-graph Generation

The procedure to generate the meta-graph G_M associated to 1) the graph $G = (V, A)$ and 2) the set of candidate elements to be deleted $E_D \subset E$ is described below. Fig. 5.5 shows a graphical representation of the given procedure.

1. Find the connected components of G_{SD} and denote them as $\{c_1, c_2, \ldots, c_p\}$ (see Fig. 5.5(a)).

2. Find the connected components of G_{SND} and denote them as $\{c_{p+1}, c_{p+2}, \ldots, c_{p+r}\}$ (see Fig. 5.5(a)).

3. Each connected component of G_{SD} and G_{SND} becomes a vertex (meta-node) of the meta-graph.

4. Two meta-nodes c_i, c_j are adjacent if and only if exist vertices $v_i, v_j \in V$ such that: (a) the arc $(v_i, v_j) \in A$ exists, (b) vertex v_i belongs to the connected component c_i, and (c) vertex v_j belongs to the connected component c_j (see Fig. 5.5(b)).

(a) Connected components in the two sub-graphs G_{SD} and G_{SND}

(b) Meta-graph connectivity
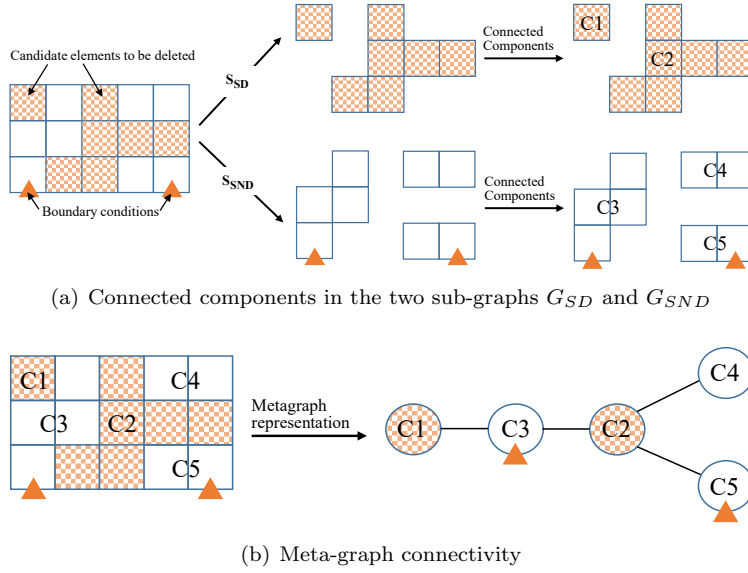
Figure 5.5: Meta-graph associated to a FEA mesh and the candidate elements to be deleted

Meta-graph Pruning

The last step of the element deletion algorithm is the elimination of the under-demanded material (meta-graph pruning). For this purpose, we consider three different scenarios:

Case 1 - Non-candidate elements for deletion are fully connected: As can be seen in Fig. 5.6(a), in this scenario all the non-candidate elements to be deleted lie in the same meta-node (C_3). In this case, all the meta-nodes that contain under-demanded elements are removed (C_1 and C_2).

Case 2 - Non-candidate elements for deletion are partially connected: In this case, the non-candidate elements for deletion are not in the same meta-node. However, all elements under the action of the stimulus S do lie in the same component. An example of this scenario is shown in Fig. 5.6(b). Since the deletion of C_1 would annul the action of C_3, in this work both C_1 and C_3 are removed. The only meta-node left after deletion would be C_2. In general, in this case all the meta-nodes but the one that contains the elements with boundary conditions are deleted.

Case 3 - Non-candidate elements for deletion are not connected: In this scenario, elements with boundary conditions are not in the same meta-node. In order to preserve the connectivity of the stimulated subdomain Ω_S, a meta-node C_i is deleted if meets these conditions: 1) C_i is a connected component of G_{SD} and 2) C_i has degree 1.

The second condition assures that deleting C_i will not affect the connectivity of the elements with boundary conditions.

For the example illustrated in Fig.5.6(c), the only meta-node that is deleted is C_1, since the deletion of C_2 would generate a disconnection between the meta-nodes with boundary conditions (C_3, C_5).

69

(a) Case 1: Non-candidate elements for deletion are fully connected.

(b) Case 2: Non-candidate elements for deletion are partially connected.

(c) Case 3: Non-candidate elements for deletion are not connected.
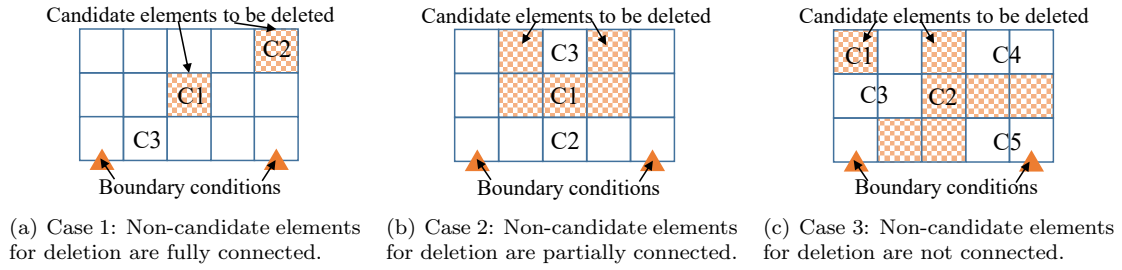
Figure 5.6: Material removal scenarios.

5.5.4 Boundary Synthesis

Since the presented algorithm works with FEA meshes, the final shapes obtained with the algorithm tend to be rough and difficult to manufacture. For this reason, the boundary of the final designs must be smoothed. In Fig. 5.7 is shown the process to obtain the smoothed boundary of a given FEA mesh.

(a) Block diagram

(b) Example
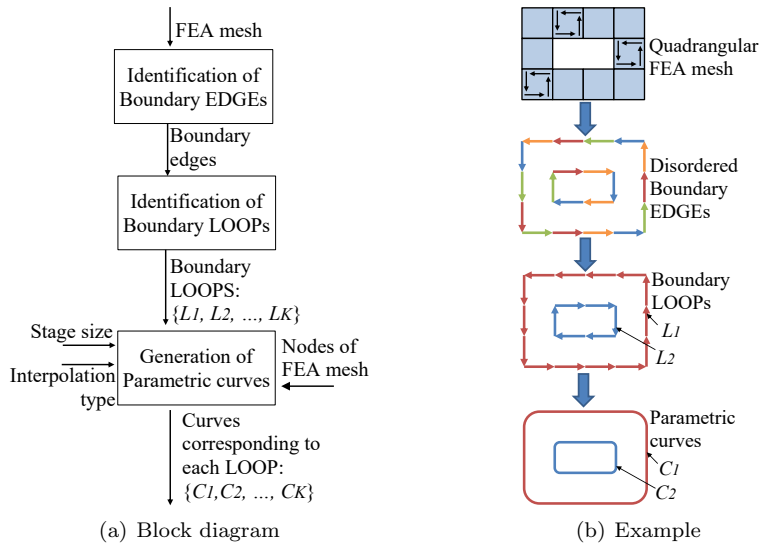
Figure 5.7: Post-processing for part boundary smoothing.

5.6 Results

Section 5.6.1 reports the accomplished results with our meta-graph based algorithm for different problems found in the literature. Section 5.6.2 reports the results for other simulations that are useful to illustrate the behavior of the presented algorithm. In all the simulations we show in a particular iteration how the meta-graph approach is applied to keep always a connected domain.

5.6.1 Benchmarking Cases

Michell Structure

The design problem and theoretical solution of a Michell structure are depicted in Figs. 5.8(a) and 5.8(b). In Figs. 5.10(a)-5.10(d) can be seen the domain at different iterations. These figures show how the shape evolved until reaching a design that resembles the theoretical solution.

Figs. 5.9(a)-5.9(d) show the action of the meta-graph strategy in an intermediate iteration of the optimization process. Fig. 5.9(a) shows the candidate elements for deletion and Fig. 5.9(b) depicts the meta-nodes associated to the configuration in Fig. 5.9(a). In Fig. 5.9(c) can be seen the meta-graph abstraction for this particular iteration. Based on the algorithm presented in Section 5.5.3, the meta-nodes C_2, C_3, C_4, and C_5 would be removed and the resultant shape after elimination is shown in Fig. 5.9(d).

(a) Michell structure conditions

(b) Theoretical optimization [78]
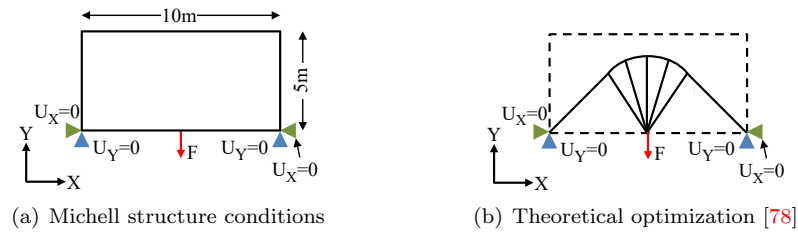
Figure 5.8: Michell structure. Deign domain and benchmarking solution.

(a) Elements candidate for elimination: red.

(b) Meta-nodes: (i) C1: green region. (ii) C2, C3: red. (iii) C4, C5: blue.

(c) Meta-graph generated from Fig. 5.9(b).

(d) Surviving meta-node C1 after elimination of meta-nodes C2, C3, C4, C5.

Figure 5.9: Michell structure. Intermediate iteration. Elimination of under-stressed meta-nodes lead to disconnection-based secondary elimination, as administered by the meta-graph strategy.

<div align="center">(a) Iteration 40   (b) Iteration 120   (c) Iteration 160   (d) Iteration 240</div>

Figure 5.10: Michell structure. Evolution dictated by the meta-graph strategy. Dotted line denotes the initial design domain.

Two Bar Frame:

The initial domain and boundary conditions for the design of a two bar frame are shown in Figs. 5.11(a). The theoretical solution is illustrated in Fig. 5.11(b). The evolution of the shape throughout the optimization is shown in Figs. 5.13(a)-5.13(d). As in the Michell structure example, it can be seen that the design obtained with the meta-graph abstraction is similar to the theoretical solution.

The role of the meta-graph modeling in the optimization process is shown in Fig. 5.12. In Fig. 5.12(a) are shown the candidate elements for deletion. This is an example of the *Case 1* described in Section 5.5.3, since all the non-candidate elements for deletion lie in the same meta-node, as shown in Fig. 5.12(b). Thus, all the meta-nodes different to C_1 can be deleted and the resultant shape is as seen in Fig. 5.12(c).

Michell Structure with Alternative Boundary Conditions

The initial domain and boundary conditions for a Michell structure are shown in Fig. 5.14(a). In comparison with the first example, the node in the lower-right corner does not have restriction of movement in X direction. Fig. 5.14(b) exhibit a solution obtained via simulation by Xie and Steven ([62]). In Figs. 5.16(a)-5.16(d) is shown the shape of the domain at different iterations. Notice that the final shape is similar to the proposed by Xie and Steven ([62]).

Fig. 5.15 show the performance of the meta-graph based algorithm in a intermediate iteration. As in the previous examples, Figs. 5.15(a), 5.15(b), and 5.15(c) show the tentative element for deletion and the meta-graph associated to the current iteration. This is an instance of the *Case 2* presented in Section 5.5.3. Fig. 5.15(d) shows the resultant domain after the application of the corresponding meta-graph pruning strategy.

(a) Boundary conditions

(b) Theoretical solution [78]
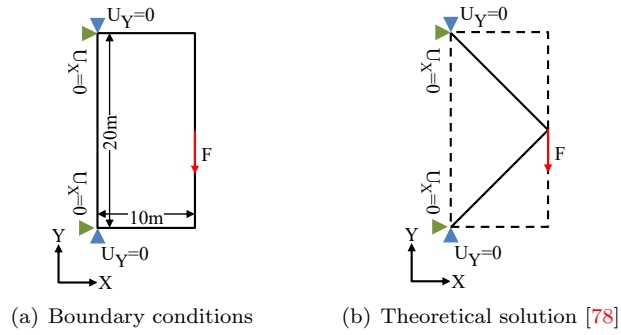
Figure 5.11: Two bar frame. Design domain and benchmarking solution.

(a) Elements candidate for elimination: red. Meta-nodes: (i) C1: green region. (ii) C2, C3, C4, C5, C6, C7, C8: red.

(b) Meta-graph generated from Fig. 5.12(a).

(c) Surviving meta-node C1 after elimination of meta-nodes C2, C3, C4, C5, C6, C7, C8.
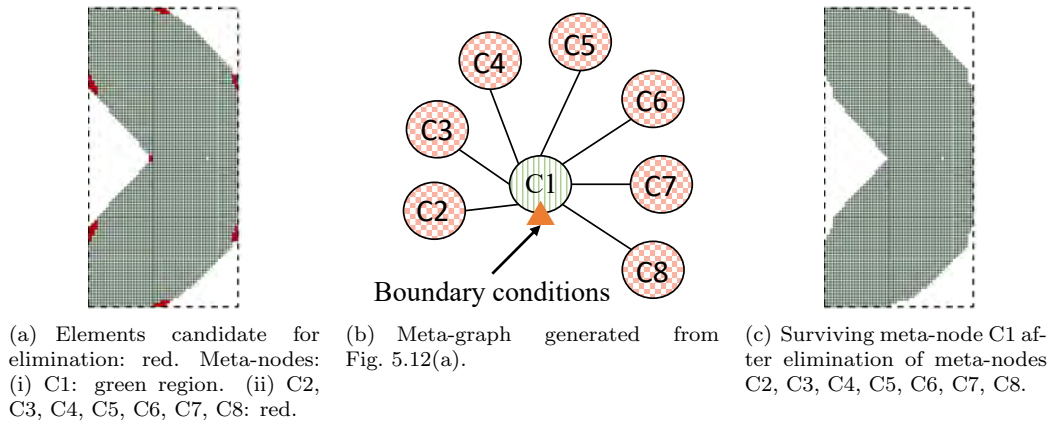
Figure 5.12: Two bar frame. Intermediate iteration. Elimination of under-stressed meta-nodes lead to connected domain.

(a) Iteration 10

(b) Iteration 50

(c) Iteration 150

(d) Iteration 300
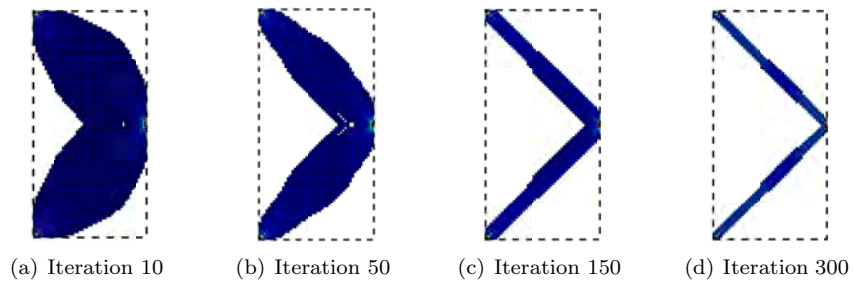
Figure 5.13: Two bar frame. Evolution dictated by the meta-graph strategy. Dotted line denotes the initial design domain.

73

(a) Boundary conditions.

(b) Proposal by Xie and Steven ([62]).
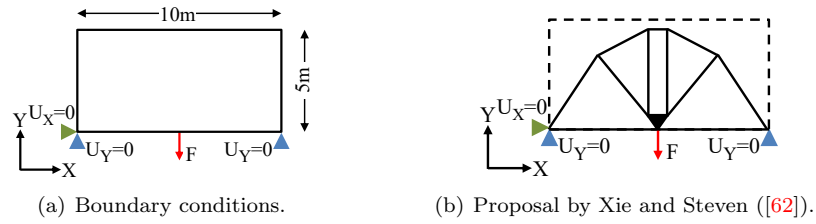
Figure 5.14: Michell structure with alternative boundary conditions. Design domain and benchmarking solution.

(a) Elements candidate for elimination: red.

(b) Meta-nodes: (i) C1: green region. (ii) C2, C3, C4, C5: red. (iii) C6: blue.

(c) Meta-graph generated from Fig. 5.15(b).

(d) Surviving meta-node C1 after elimination of meta-nodes C2, C3, C4, C5, C6.
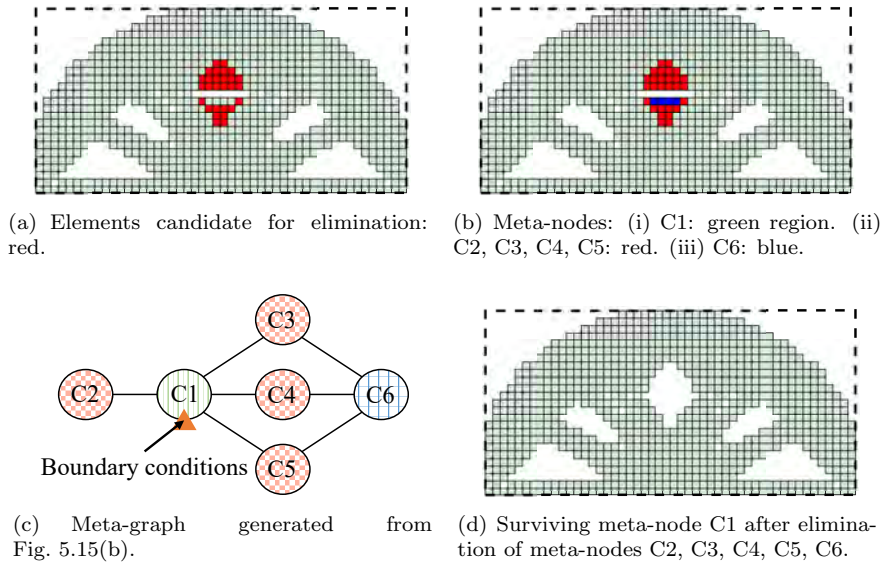
Figure 5.15: Michell structure with alternative boundary conditions. Intermediate iteration. Elimination of under-stressed meta-nodes lead to disconnection-based secondary elimination, as administered by the meta-graph strategy.

(a) Iteration 40.

(b) Iteration 70.

(c) Iteration 120.

(d) Iteration 135.
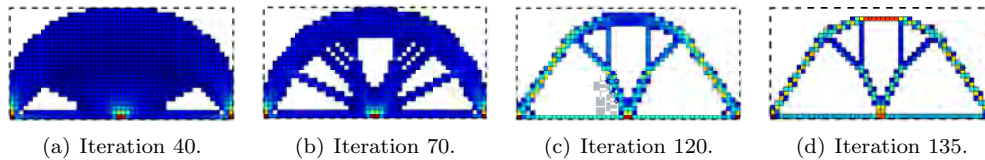
Figure 5.16: Michell structure with alternative boundary conditions. Evolution dictated by the meta-graph strategy. Dotted line denotes the initial design domain.

74

5.6.2 Other Experiments

Bar under Opposite Loads

In Fig. 5.17 are shown the design domain and the load conditions for a bar subjected to loads of the same magnitude but in opposite directions. With this simulation we aim to exhibit a clear example of the behavior of the meta-graph approach in the *Case 3* (see Section 5.5.3). Likewise, Fig. 5.19 shows the evolution of the shape during the optimization process.

In Figs. 5.18(a) and 5.18(b) are shown the tentative elements to be deleted and the corresponding meta-nodes. In Fig. 5.18(c), where the meta-graph is depicted, is clear that the elements with boundary conditions are not in the same component, and the deletion of meta-node C_3 would lead a non-connected domain. Thus, following the approach presented in Section 5.5.3, only the meta-nodes C_4 and C_5 can be removed. Fig. 5.18(d) exhibits the resultant shape.
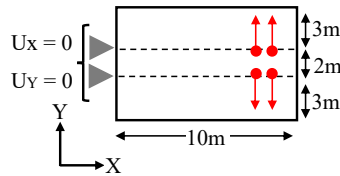
Figure 5.17: Bar under opposite loads. Design domain and load conditions.

(a) Elements candidate for elimination: red.

(b) Meta-nodes: (i) C1: magenta region. (ii) C2: green region. (iii) C3 - C5: red.

(c) Meta-graph generated from Fig. 5.18(b).

(d) Surviving meta-nodes C1, C2, C3 after elimination of meta-nodes C4, C5.
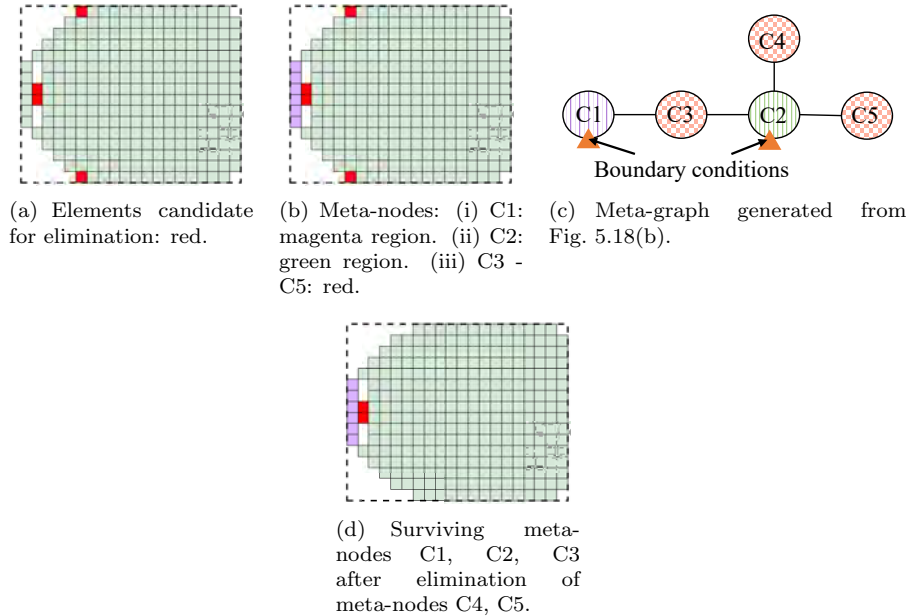
Figure 5.18: Bar under opposite loads. Intermediate iteration. Elimination of under-stressed meta-nodes lead to disconnection-based secondary elimination, as administered by the meta-graph strategy.

75

(a) Iteration 20.   (b) Iteration 30.   (c) Iteration 40.
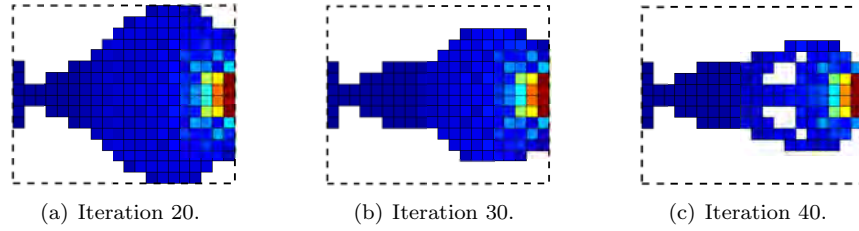
Figure 5.19: Bar under opposite loads. Evolution dictated by the meta-graph strategy. Dotted line denotes the initial design domain.

Viaduct Simulations

In order to show the capacity of our algorithm to replicate to some extent some well-known engineering structures, we carried out two different simulations to try to resemble the aspect of a viaduct. In Fig. 5.20 are shown the design domain and the load conditions for the two simulations. In both cases, a distributed load along the length of the domain is applied.

Figs. 5.22 and 5.24 the how the meta-graph abstraction was used and the resultant domain for a particular iteration in each simulation.

Figs. 5.23 and 5.25 show the evolution of the shape throughout the optimization. The obtained designs resemble to some extent the shape of a viaduct of the type of the Millau Viaduct, France. In Fig. 5.21 is shown a picture of this viaduct.

(a) Domain 1.   (b) Domain 2.
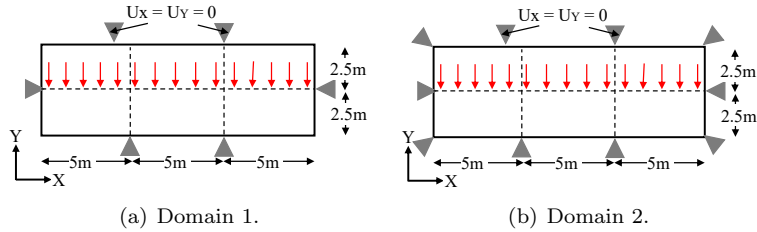
Figure 5.20: Viaduct/Bridge simulations. Design domain and load conditions.

Figure 5.21: Millau Viaduct, France. Image by `MIEL1971` ([1]). Licensed by CC0 (Creative Commons Zero).

(a) Elements candidate for elimination: red.

(b) Meta-nodes: (i) C1: green region. (ii) C2 - C9: red. (iii) C10 - C13: blue.

(c) Meta-graph generated from Fig. 5.22(b).

(d) Surviving meta-node C1 after elimination of meta-nodes C2 - C13.
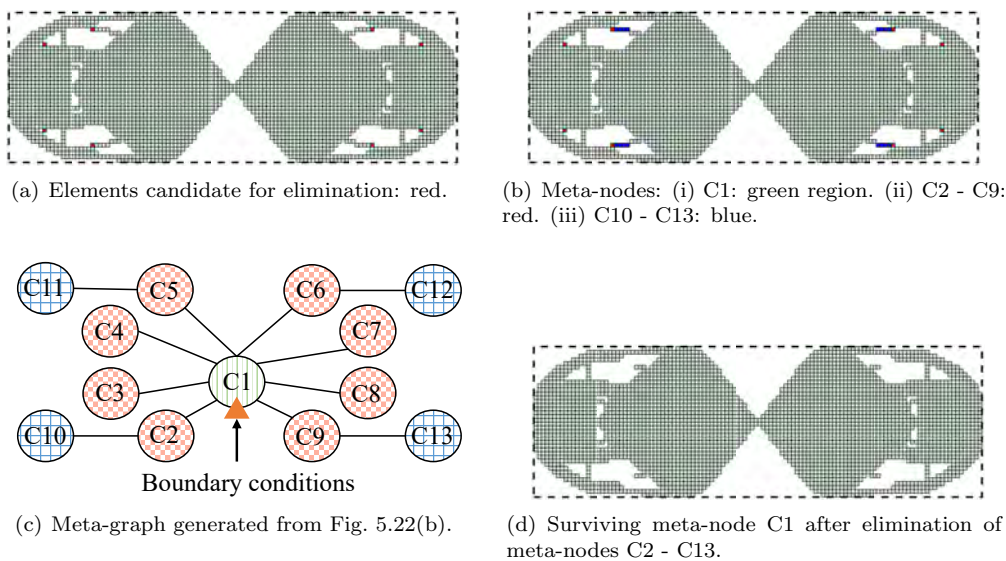
Figure 5.22: Bridge 1. Intermediate iteration. Elimination of under-stressed meta-nodes lead to disconnection-based secondary elimination, as administered by the meta-graph strategy.

(a) Iteration 30.

(b) Iteration 60.
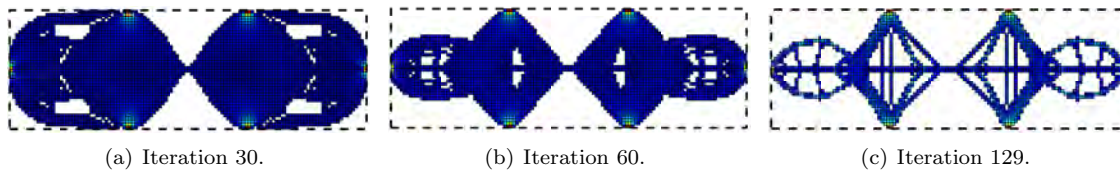
(c) Iteration 129.

Figure 5.23: Bridge 1. Evolution dictated by the meta-graph strategy. Dotted line denotes the initial design domain.

(a) Elements candidate for elimination: red.

(b) Meta-nodes: (i) C1: green region. (ii) C2 - C5: red. (iii) C6 - C9: blue.

Boundary conditions

(c) Meta-graph generated from Fig. 5.24(b).

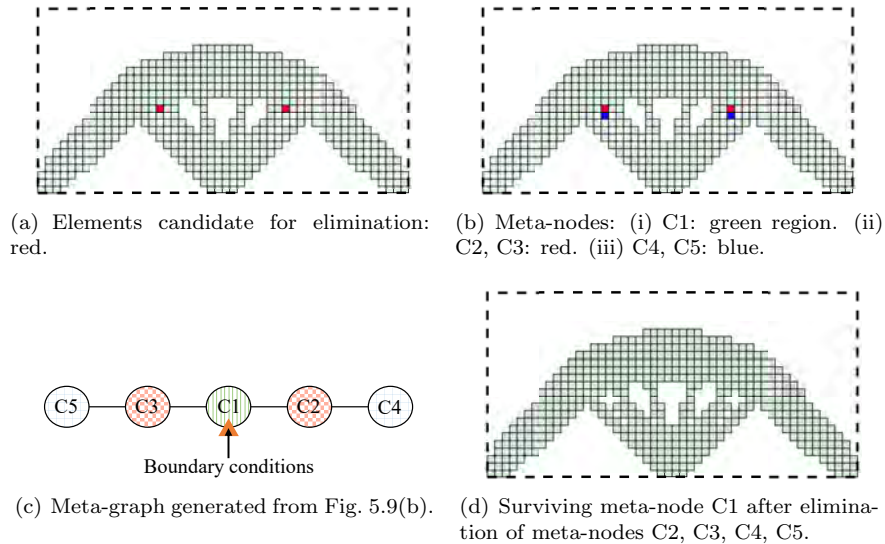(d) Surviving meta-node C1 after elimination of meta-nodes C2 - C9.
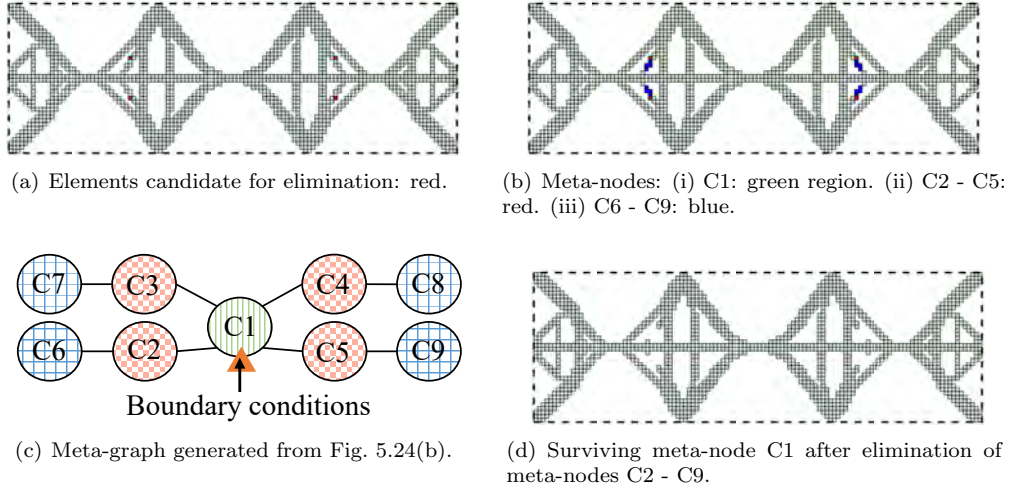
Figure 5.24: Bridge 2. Intermediate iteration. Elimination of under-stressed meta-nodes lead to disconnection-based secondary elimination, as administered by the meta-graph strategy.
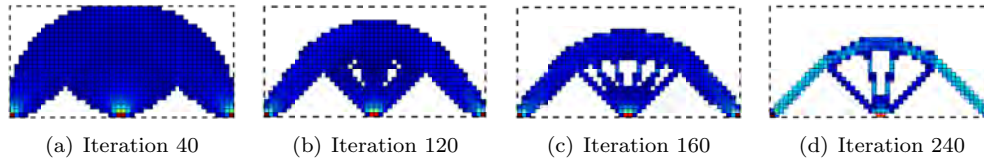

(a) Iteration 10.

(b) Iteration 60.

(c) Iteration 120.
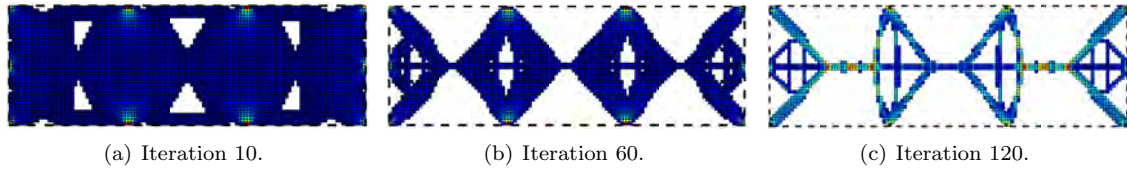
Figure 5.25: Bridge 2. Evolution dictated by the meta-graph strategy. Dotted line denotes the initial design domain.

5.6.3 Computational Demands of the Proposed Algorithm

Due to the material removal procedure associated to the presented algorithm, given the mesh $M_i = (N_i, E_i)$ at iteration i we can say: $|N_0| \geq |N_i|$ and $|E_0| \geq |E_i|$, where $M_0 = (N_0, E_0)$ is the initial mesh. In addition, $|N_0| > |E_0|$. Therefore, the computational demands of one iteration of the algorithm can be expressed as a function of N_0 and the bandwidth W of the stiffness matrix calculated during the FEA simulation [61].

Table 5.1 presents the computational expenses of our algorithm. Notice that the time complexity and memory complexity of an iteration of our algorithm is dictated by the term $O(N_0^2)$. This term corresponds to the dominant generation of the graph and the meta-graph associated to the FEA mesh.

A comparison of the computational resources used vs. the efficiency of evolution is beyond our capabilities. One reason for this limitation is that the measure of the quality or efficiency of an evolution is itself an open research question at this time.

Table 5.1: Analysis of the computational costs of an iteration of the proposed algorithm

Process	Time expenses	Memory expenses
FEA Simulation	$O(N_0 W^2)$ [61]	$O(N_0 W)$ [61]
Mesh Partition	$O(N_0)$	$O(N_0)$
Element Deletion	$O(N_0^2)$	$O(N_0^2)$
Graph Generation	$O(N_0^2)$	$O(N_0^2)$
Graph Components Calculation	$O(N_0)$	$O(N_0)$
Meta-graph Generation	$O(N_0^2)$	$O(N_0^2)$
Meta-graph Pruning	$O(N_0)$	$O(N_0)$

5.6.4 Boundary Synthesis

The simulations carried out with the meta-graph based algorithm showed that the resultant shape is very rough. Following the procedure described in Sect. 5.6.4, one of the designs obtained with the algorithm was smoothed. The results of the application of the smoothing algorithm using a mean filter of order 4 are shown in Fig. 5.26. Notice that the boundary of the shape was corrected without losing sensitive information of the design.

(a) Result of meta-graph pruning   (b) Structure boundary   (c) Smoothed boundary
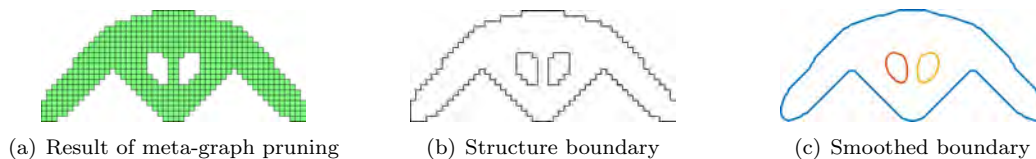
Figure 5.26: Michell structure. Post-processing for border smoothing.

5.7 Conclusions

This article presents a novel methodology for topology optimization. This methodology joints the concepts of ESO (a well-known optimization algorithm) with mathematical graph modeling of the FEA mesh. The presented methodology is able to remove progressively the under-demanded material of the structure and to produce a feasible solution at every iteration.

In comparison with previous works that use graph abstractions and ESO, this article presents a general approach in which the removal of under-demanded material is fully based on a meta-graph abstraction of the FEA mesh. In addition, this paper presents six different examples with a clear illustration of the meta-graph approach in each example. In spite of the algorithm has been developed only for 2D topology optimization, it can be extended to be applied for 3D domains.

Despite the given examples are in the field of 2D linear elasticity, the given algorithm can be adapted to interact with other stimuli sources different from forces, pressures or torques. The only requirement is that the effects of the stimuli can be described as a scalar field f acting on a set of graph nodes.

5.7.1 Limitations and Shortcomings

In the case in which elements with boundary conditions do not lie in the same meta-node, some meta-nodes of degree 2 (or more) could be deleted and the optimization process must be divided in multiple branches. However, since only meta-nodes of degree 2 are deleted, all the other branches are not considered.

5.7.2 Future Work

Future work should address the utilization of stimuli other than stress/strain: friction, abrasion, heat, humidity, etc. Future research should also address the extension of the algorithm to $\mathbb{R}^3$ and the integration of our algorithm with other evolutionary based techniques (e.g. mutation) to allow the generation of multiple feasible solutions that explore a wider region of the solution space.

Chapter 6

FE-Simulations with a Simplified Model for Open-Cell Porous Materials: A Kelvin Cell Approach

Diego Montoya-Zapata[1], Camilo Cortés[1,2], Oscar Ruiz-Salguero[1]
[1] Laboratory of CAD CAM CAE, Universidad EAFIT, Medellín, Colombia.
[2] eHealth and Biomedical Applications, Vicomtech, Spain.

6.1   Context

6.1.1 Proof of Submission

This article presents the results of a collaborative work between the following institutions: (1) Universidad EAFIT, represented by Laboratory of CAD CAM CAE Research Group, and (2) Vicomtech. The paper was submitted to the Journal of Computational Methods in Sciences and Engineering and it is now in the second stage of revision (see email of the responses for the first stage of revision in Fig. 6.1).

```
On 27 Apr 2018, at 09:54, Camilo Cortes <ccortes@vicomtech.org> wrote:

Dear Prof. Simos,

We are sending the revised version of manuscript JCMSE_1927:

FE-Simulations with a Simplified Model for Open-Cell Porous Materials:
A Kelvin Cell Approach. Diego Montoya-Zapata, Camilo Corts, Oscar
Ruiz-Salguero.

Attached you can find:

1. Our response letter to the comments of the reviewer.
2. The revised version of the manuscript.
3. The previous version of the manuscript with marks indicating the parts
   of the manuscript that were eliminated or modified in the revised
   version of the manuscript.

Please let us know of any additional actions required to continue with the
review process of the article.

Best regards,

Camilo Corts

Dr.-Ing. Camilo Andrs Corts Acosta, PhD
Researcher | Investigador

ccortes@vicomtech.org
+[34] 943 30 92 30
eHealth and Biomedical Applications | eSalud y Aplicaciones Biomdicas
```

Figure 6.1: Email of responses of 1st revision to the Journal of Computational Methods in Sciences and Engineering.

6.2 Abstract

In in-silico estimation of mechanical properties of open (Kelvin) cell porous materials, the geometrical model is intractable due to the large number of finite elements generated. Such a limitation impedes the study of reasonable domains. VoXel or Boundary representations of the porous domain result in FEA data sets which do not pass the stage of mesh generation, even for very modest domains. Our method to overcome such limitations partially replaces geometrical minutiae with kinematical constraints imposed on cylindrical bars (i.e. Truss model). Our implemented method uses node position equality constraints augmented with rotation constraints at the joints. Such a method significantly reduces the computational expense of the model, allowing the study of domains of 10^3 Kelvin cells. The results of the tests executed show the accuracy and efficiency of the Truss model in the estimation of Young's modulus and Poisson's ratio when compared with current procedures. The method allows application for materials which depart from Kelvin Cell uniformity, since the Truss model admits general configurations. As the simulation is made possible by the Truss model, new challenges appear, such as the application to anisotropic materials and the automatic generation of the Truss model from actual foam scans (e.g. tomographies).

6.2.1 Keywords

Computational efficiency, in-silico estimation, Kelvin cell, porous materials, Poisson's ratio, Truss model, Young's modulus.

Glossary

BB:	Bounding box.
BREP:	Boundary representation of a solid in R^3.
FE:	Finite element.
FEA:	Finite element analysis.
Δi:	Displacement in direction i (m).
$\Delta i^{(j)}$:	Displacement of node j in direction i (m).
ϵ_k:	Strain in direction k (m).
$\bar{\epsilon}_k$:	Average strain in direction k for a set of nodes (m).
E_k:	Young's modulus in direction k (Pa).
$i^{(j)}$:	Coordinate i of node j.
L_i:	Length of the domain in direction i (m).
ρ:	Relative density of a porous domain (%).
r:	Radius of the ligaments of the domain (m).
r_{node}:	Radius of the spheres that model the ligament joints of the domain (m).
σ:	Total stress applied in compression test (Pa).
V_{ij}:	Poisson's ratio measured from a contraction in direction j given an extension in direction (adimensional).
$\lvert \cdot \rvert$:	Cardinality of a set.

6.3   Introduction

Porous materials have a wide range of applications that cover different fields such as medicine, biotechnology, automotive industry, design and manufacturing ([79–81]). In many of these applications a mechanical characterization of the material is needed. However, (1) existing material tests are extremely expensive and (2) most of the computer simulations are intractable because of the large size of the models. Therefore, the development of an effective and efficient method for the estimation of the mechanical properties of porous material is a matter of interest.

Different authors have proposed numerical simplified models for the study of the mechanical behavior of porous materials. One of the most common approaches is to represent the complicated geometry of the material with regular arrays of Kelvin cells [49,50,81–87]. Ref. [88] presents another simplification technique (Truss model), in which the ligaments of the material are represented with beams of circular cross-section and variable radius.

In this article we aim to evaluate a variation of the Truss model using Kelvin cells. Our evaluations is purely numerical and neither experimental data nor experimental results are used for benchmarking. The results obtained allow us to confirm that the proposed variation of the Truss model is a promising technique for obtaining efficient and accurate estimations of the mechanical moduli of open-cell porous materials.

This article is structured as follows: in Section 6.4 we provide a review of the geometric models used for the representation of porous materials. In Section 6.5 we describe the employed methodology. Section 6.6 presents and evaluates the results of the simulations. Finally, Section 6.7 contains the conclusions of this work and possible future improvements on this research.

6.4   Literature Review

Multiple techniques have been used to obtain theoretical and computational models that may be used to study the properties of porous materials, such as: models of regular arrays of polyhedra (Kelvin cells [50, 81–87] and WeairePhelan cells [89]), random tessellation models [82, 90, 91], 3D image-based models [10, 52, 54, 92], and 1D image-based models ([88]). However, given the scope of this research, we will focus on reviewing (1) image-based models (1D, and 3D) and (2) models of regular arrays of Kelvin cells. A description of the other methodologies can be found in [93].

1. Image-based models: These models take a set of images (commonly from a X-ray computed tomography (CT) [10, 52, 54, 88, 92]) of an actual foam sample to obtain an accurate computational representation of the domain of study. The images are processed to retrieve a 3D representation of the foam and to generate its respective FE model [93]. Depending on the type of element used for the FE simulations, these models may be classified as 3D image-based models and 1D image-based models.

   (a) 3D or BREP models: The main goal of BREP models is to preserve with a great level of detail the geometry and topology of the original material sample. For this reason, 3D elements (cubic elements from VoXels [52] or tetrahedral elements [54]) are used for the FE meshing. The obtained model consumes significant memory and time in FEA simulations ([10, 54, 94]). Therefore, simulations are constrained to small domains.

   (b) 1D or Truss models: These models attempt to retain most of the geometry and topology of the original material sample using less computational resources when compared with

84

BREP models [88]. This is achieved by using 1D elements (beams of circular cross-section with variable radius) for approximating foam ligaments. Truss models are used for the estimation of equivalent mechanical moduli (Young, Shear, Poisson) of real foam samples. Errors in the estimations are under 16%, when compared with the respective BREP model. However, BREP model tends to be stiffer than the Truss model.

2. Models of regular arrays of Kelvin cells: This technique has been used to developed both theoretical and numerical models that allow the analysis of the mechanical properties of open-cell porous materials. The studies include the characterization of the compressive ([50, 84–86]) and tensile ([87]) responses, the description and prediction of equivalent mechanical moduli ([81, 82, 84]), and the analysis of thermal conductivity ([83]).

In what concerns to the study of the equivalent mechanical moduli of Aluminum foams, authors in [50, 82] report results considering one anisotropic Kelvin cell modeled with (a) 3D solid elements (BREP model) and (b) beams of non-uniform cross section area (Truss model). Errors of the Truss model vs. BREP model are between 14% and 17%, with the BREP model being always stiffer than the Truss model. However, they do not assess the accuracy of the estimations for a domain of more than one cell. They evaluate the results against experimental estimations, which is out of the scope of this article.

Conclusions of the Literature Review

Based on the literature review, the Truss model excels the BREP model in the efficiency of the use of computational resources. Likewise, the Truss model is able to conserve the geometry and topology of the original foam. However, it is a matter of interest to make the Truss representation stiffer so that it resembles more accurately the behavior of the BREP model.

In this article, we generate a stiffer Truss model by adding rotation constraints at the joins of the bars. We perform an evaluation of the proposed Truss abstraction using Kelvin cells, which is a widely used technique for the analysis of porous materials.

Unlike other approaches in which domains of a single Kelvin cell are considered, we study five domains formed with 1, 4, 8, 12, and 1000 Kelvin cells. The evaluation consists in the estimation of equivalent mechanical moduli (Young's modulus, Poisson's ratio) using FE mechanical simulations in compression static tests. We compare the estimations performed by the BREP and Truss modeling approaches for four domains (1, 4, 8, and 12 Kelvin cells). We also show the computational efficiency of the Truss model with respect to the BREP model.

6.5   Methodology

In order to evaluate our approach to estimate equivalent mechanical moduli of porous materials, we simulate numerical compression tests using ANSYS. Simulations are configured to appraise the models in the elastic region. In addition, to asses the performance of the proposed approach, we compare the estimations of the (a) BREP model, (b) traditional Truss model, and (c) proposed Truss model with restricted rotations, taking the BREP as Reference model to measure the error in the estimations of the other two models.

The addition of rotational constraints at the ligament junctions allows the traditional Truss model to gain torque resistance. Therefore, the traditional Truss model and its variation with

restricted rotations may be also called Torque-disabled and Torque-enabled Truss models, respectively.

In Fig. 6.3 we show the process to carry out the mechanical moduli estimations with the BREP and Truss abstractions. This process can be summarized in three main steps:

1. Generation of a suitable BREP and Truss models for FE simulations.

2. Set up and execution of the FE compression test in ANSYS.

3. Estimation of the moduli (Young's modulus, Poisson's ratio) based on the resultant nodal deformations.

6.5.1 Domain Characterization

We analyze five domains of isotropic Kelvin cells composed by 1, 4, 8, 12, and 1000 Kelvin cells. Fig. 6.2 illustrates the 5 domains. The specification of the Kelvin cell properties (material and statistical dimensions) corresponds to an existing physical sample with height 100μm and average ligament radius $r = 5.0\mu$m [88]. Ligament junctions (nodes) are modeled as spheres of radius $r_{node} = 5.42\mu$m to avoid the formation of stress concentrators (crevasses) in the zones close to the nodes.

(a) 1 Kelvin cell   (b) 4 Kelvin cells   (c) 8 Kelvin cells   (d) 12 Kelvin cells

(e) 1000 Kelvin cells
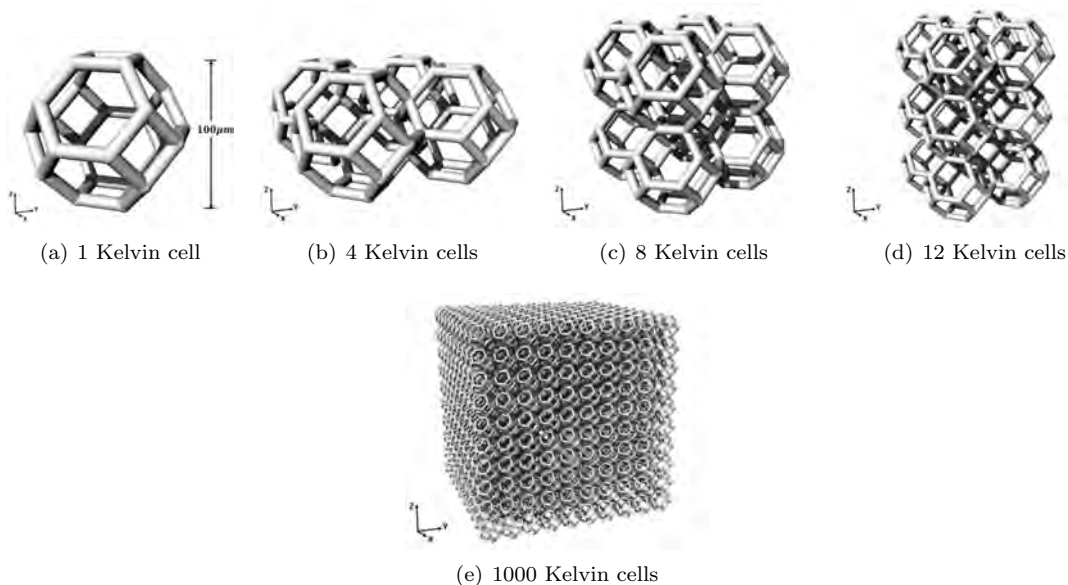
Figure 6.2: Analyzed domains.

6.5.2 Generation of BREP and Truss Models

BREP Model for FEA:

We use Rhinoceros 3D to produce a BREP of each analyzed domain. Then, we generate the corresponding 3D mesh in ANSYS. For full 3D FEA simulation we use elements SOLID185 [95].

These elements are first order ones (2 nodes/edge) and accept linear and non-linear analysis. Other ANSYS elements (SOLID186, SOLID187) have higher order, thus demanding more computational resources. Elements SOLID186 and SOLID187 are not needed for elastic compression loads. Fig. 6.4(a) presents the 3D mesh generated in ANSYS for the domain of 8 Kelvin cells.

Truss Model for FEA:

We generate a Truss abstraction of each domain of Kelvin cells using C language. Then, we generate two independent FEA cases in ANSYS that correspond to the Torque-enabled and Torque-disabled Truss models. Fig. 6.4(b) shows the mesh generated in ANSYS using beam elements. We use BEAM188 for the FE analysis. This is a first order element and serves linear elastic loads (our simulation domain). ANSYS element BEAM189 was not selected since it has higher order (not essential in our case) and thus demands larger computational resources [95].

6.5.3   Configuration of the Compression Test

The parameters used for the simulations are reported in Table 6.1. The set-up of the compression test for the domain of 8 Kelvin cells is displayed in Fig. 6.5. For the BREP and Truss models, at the bottom of each domain: (1) Z displacement is set to 0, and (2) at least two nodes at the center are embedded (all degrees of freedom are constrained to zero displacement). Compression loads in negative Z direction are applied at the top of each domain. Table 6.1 shows the magnitude of the loads.

In the case of the Torque-enabled Truss model, at the junction of the ligaments, rotations with respect to X, Y, and Z are set to 0. These rotation constraints allow us to simulate a stiffer Truss model without modeling explicitly the junctions between the struts of the porous domain, which must be modeled when the BREP abstraction is used.

Table 6.1: Simulation set-up.

| Property | Experiment conditions | |
	Truss model	BREP model
Material	Al-6101-T6 [82]	Al-6101-T6 [82]
Young's modulus of bulk material	$E = 69.0$ GPa [82]	$E = 69.0$ GPa [82]
Poisson's ratio of bulk material	$V = 0.3$ [82]	$V = 0.3$ [82]
Side length of Kelvin cell	100.0 μm [88]	100.0 μm [88]
Ligament radius	$r = 5.0$ μm [88]	$r = 5.0$ μm [88]
Nodal radius	Does not apply	$r_{node} = 5.42$ μm
Total applied stress[a]	2.50 MPa	2.0 to 2.3 MPa

[a]FEA requests Force (and not Pressure) boundary conditions. Pressure values slightly differ due to the fact that they are calculated as F/A using a bounding box side area.

6.5.4   Estimation of Young's Modulus and Poisson's Ratio

Young's modulus E_z is estimated as per Eq. 6.1:

(a) Truss model
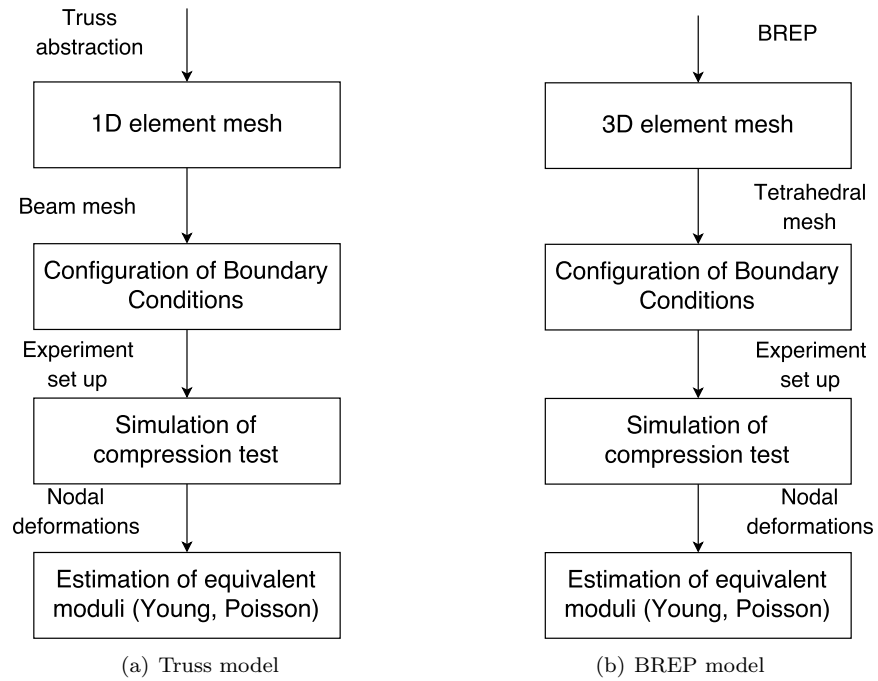
(b) BREP model

Figure 6.3: Comparison between procedures for the moduli estimation the Truss and BREP models.

(a) BREP model
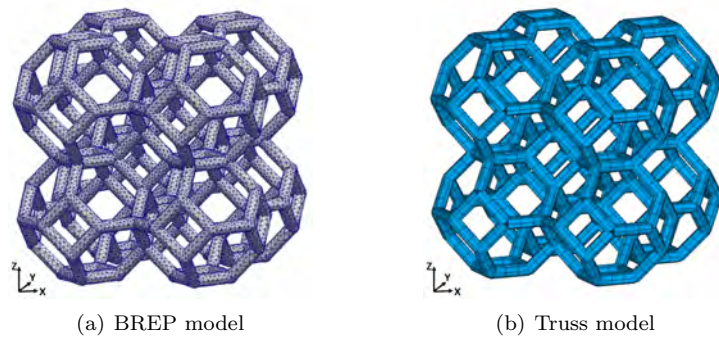
(b) Truss model

Figure 6.4: Meshes generated in ANSYS for the domain of 8 Kelvin cells.
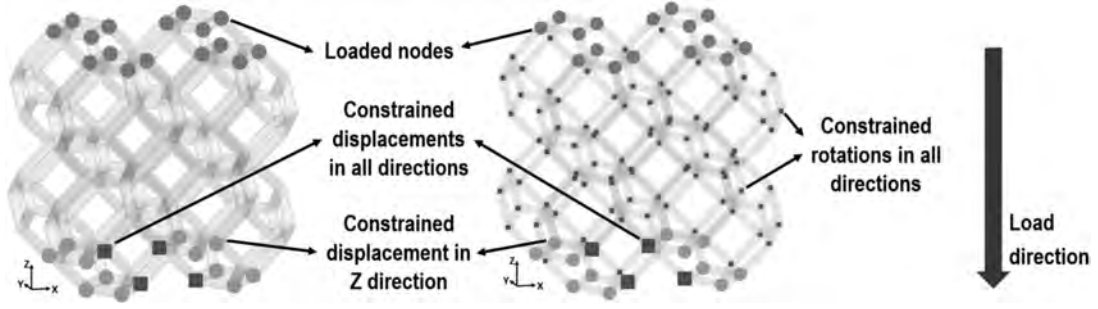
Figure 6.5: Domain of 8 Kelvin cells. Boundary conditions for the (a) BREP model (left), and (b) Truss model (right).

$$E_z = \frac{\sigma}{\epsilon_z} \qquad (6.1)$$

where σ is the total applied stress (see Table 6.1) and ϵ_z is the strain in Z direction.

On the other hand, Poisson's ratio (V_{zx}, V_{zy}) is estimated as per Eq. 6.2:

$$V_{zj} = \epsilon_j/\epsilon_z \text{ for } j = x, y \qquad (6.2)$$

where ϵ_j is the strain in j direction (j = X, Y), and ϵ_z is the strain in Z direction.

To estimate the strain in each direction, we calculate the average strain for a set of FE nodes in a selected region of the domain. Figs. 6.6 and 6.7 depict the regions selected for the estimation of X, Y, and Z strain for some of the studied domains. The thickness of each band corresponds to the 10% of the domain size length.

(a) 1 Kelvin cell   (b) 4 Kelvin cells   (c) 8 Kelvin cells   (d) 12 Kelvin cells
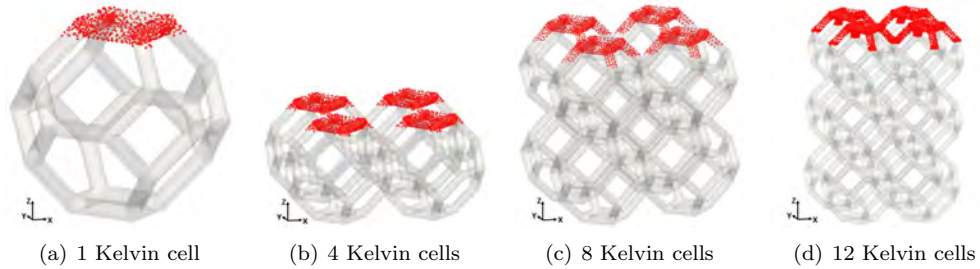
Figure 6.6: Selected region to estimate strain in Z direction.

6.6 Results and Discussion

6.6.1 Relative Density

Table 6.2 shows the calculation of the relative densities for the five analyzed domains. Notice that for every domain, the relative density is between 6.2% and 7.0%, which lie in the range of typical relative densities for metal foams [96].

89

(a) 1 Kelvin cell   (b) 4 Kelvin cells   (c) 8 Kelvin cells   (d) 12 Kelvin cells
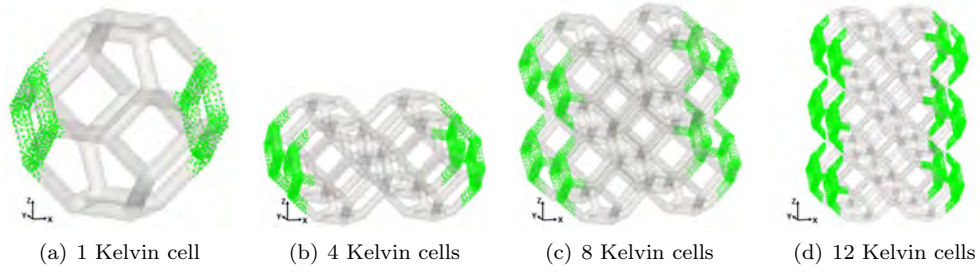
Figure 6.7: Selected region to estimate strain in X direction.

Table 6.2: Relative density of the analyzed domains.

Domain	Relative density (%)
1 cell	6.98%
4 cells	6.73%
8 cells	6.56%
12 cells	6.51%
1000 cells	6.19%

(a) BREP model   (b)   Torque-enabled   (c)   Torque-disabled   (d)   Torque-enabled
Truss model   Truss model   Truss model

(e)   Torque-disabled
Truss model
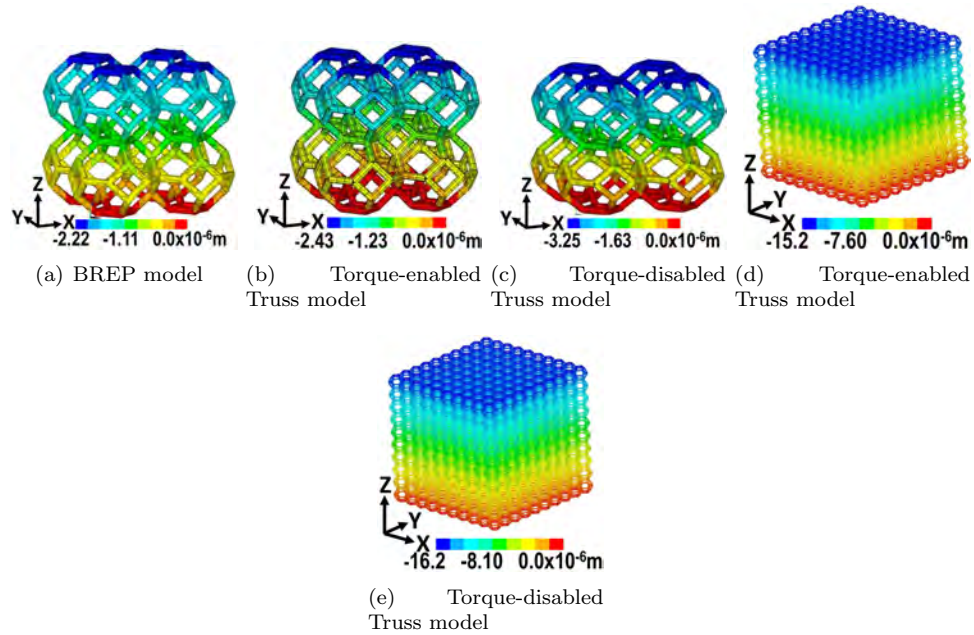
Figure 6.8: Compression test. Nodal displacements in Z direction for the domains of 8 and 1000 cells. Domain deformation is not noticeable in this image.

90

6.6.2 Mechanical Moduli Estimation

Fig. 6.8 shows the resultant nodal displacements in Z direction after the simulation of a compression test. The figure exhibits the response of the BREP and Truss abstractions for the domains of 8 and 1000 Kelvin cells. The reader may observe that the nodal displacements of each studied domain have the same order of magnitude. Likewise, the nodal displacements for the Torque-enabled Truss model are lower than for the Torque-disabled Truss model.

Table 6.3: Graphical version in Figs. 6.9 and 6.10. Mechanical moduli estimation with (a) BREP model, (b) Torque-enabled Truss model, and (c) Torque-disabled Truss model. The BREP model is considered as ground truth. Percentage errors are calculated based on 6 decimal places, while only 2 decimal places appear in this Table.

Modulus	Domain	BREP model	Torque-enabled Truss model. Relative error %	Torque-disabled Truss model. Relative error %
Young (E_Z)	1 cell	182.07 MPa	223.96 MPa (23.01%)	166.57 MPa (8.52%)
	4 cells	200.41 MPa	230.36 MPa (14.94%)	149.00 MPa (25.65%)
	8 cells	223.11 MPa	208.94 MPa (6.35%)	162.42 MPa (27.20%)
	12 cells	234.43 MPa	202.73 MPa (13.52%)	165.74 MPa (29.30%)
	1000 cells	NA^a	165.72 MPa (NA)	158.04 MPa (NA)
Poisson (V_{ZX})	1 cell	0.49	0.45 (8.38%)	0.47 (3.73%)
	4 cells	0.44	0.40 (8.57%)	0.44 (0.47%)
	8 cells	0.44	0.43 (3.31%)	0.45 (1.42%)
	12 cells	0.44	0.43 (1.94%)	0.45 (1.86%)
	1000 cells	NA	0.45 (NA)	0.45 (NA)
Poisson (V_{ZY})	1 cell	0.48	0.45 (6.64%)	0.47 (1.89%)
	4 cells	0.45	0.40 (9.23%)	0.44 (1.19%)
	8 cells	0.44	0.43 (3.06%)	0.45 (1.69%)
	12 cells	0.44	0.43 (2.39%)	0.45 (1.39%)
	1000 cells	NA	0.45 (NA)	0.45 (NA)

^{a}NA: Not available

Based on the nodal deformations, we estimate Young's modulus (E_z), and Poisson's ratio (V_{zx}, V_{zy}) using Eqs. 6.1, and 6.2. Results are listed in Table 6.3 and a comparison of the estimations using the three models is depicted in Fig. 6.9. As expected from the nodal displacements shown in Fig. 6.8, Young's modulus estimations for the Torque-enabled Truss model are greater than for the Torque-disabled Truss model. So, restricting the rotations of the Truss abstraction produces a stiffer model with the advantage that the nodes must not be modeled explicitly, as is the case for the BREP model.

For few (less than 8) Kelvin cells, the Truss model does not correctly mimic the BREP model. However, notice that the computational cost of the BREP model is so large that only 12 Kelvin Cells can be modeled in total. It is worth remarking that for larger domains (8 or more cells), the

Torque-enabled Truss model almost halves the error of the Torque-disabled model in the estimation of the Young's modulus, being indeed a stiffer model than the one used in [88].

The reader may observe in Fig. 6.9 that Young's modulus estimations of the Torque-enabled Truss model tend to decrease when the size of the model increases. Conversely, Young's modulus estimations of the BREP model tend to increase. This fact may compromise the accuracy of the Truss abstraction for larger domains. However, notice that the estimations of the Torque-enabled Truss model are greater that the ones of the Torque-disabled model, even for the domain of 1000 Kelvin cells. So, for this task, the Torque-enabled Truss model is a better option than the traditional Torque-disabled Truss model.

Errors in the estimations of Poisson's ratio (V_{zx}, V_{zy}) using both Truss abstractions are under 10% in all the presented cases, as shown in Fig. 6.10. Moreover, error tends to decrease when the domain becomes larger. This performance confirms that the Truss abstraction is a feasible alternative for the numerical estimation of the Poisson's ratio for large porous domains.

(a) Young's modulus E_Z (b) Poisson's ration V_{ZX} (c) Poisson's ration V_{ZY}
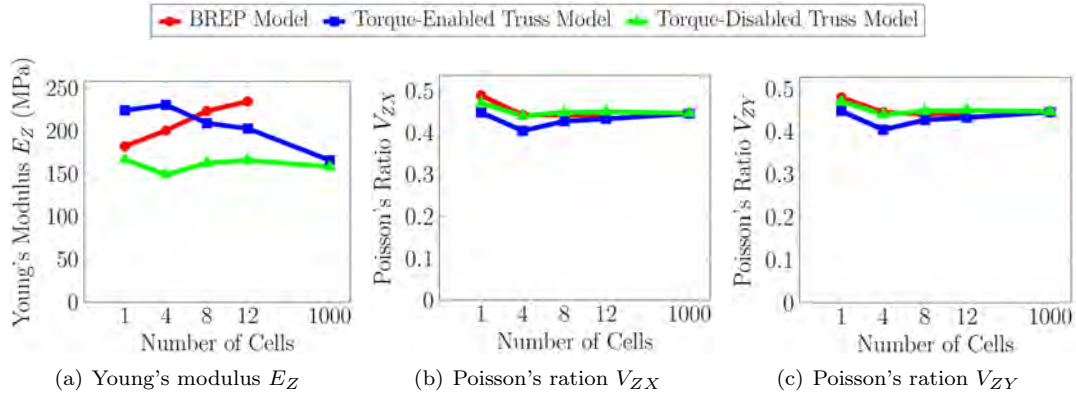
Figure 6.9: Estimations of the Young's modulus and Poisson's ratio using the (a) BREP model, (b) Torque-enabled Truss model and, (c) Torque-disabled Truss model.

(a) Young's modulus E_Z (b) Poisson's ration V_{ZX} (c) Poisson's ration V_{ZY}
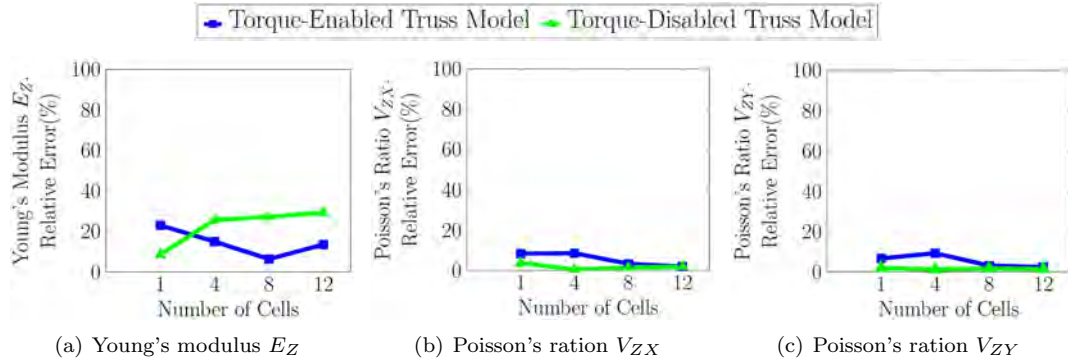
Figure 6.10: Relative error in the estimation of the Young's modulus and Poisson's ratio for the (a) Torque-enabled Truss model and (b) Torque-disabled Truss model. The BREP model is considered as ground truth.

92

6.6.3 Computational Resources

Fig. 6.11 depicts the computational expenses of the BREP and Truss abstractions: (1) the number of elements, (2) the number of equations and (3) the solver allocated memory are presented as functions of the number of ligaments of the studied domains. The computational efficiency of the Truss abstraction is noticeable: the BREP model uses 200 times the number of elements, generates 35 times the number of equations, and spends 20 times the memory of the Truss model.

In order to show that the low computational cost of the Truss abstraction allows the numerical analysis of large domains, we simulate a compression test for a domain composed by 1000 Kelvin cells. The simulation is carried out with the Torque-enabled and Torque-disabled Truss model. Fig. 6.8 shows the resulting nodal displacements in Z direction.

The estimations of the Young's modulus and Poisson's ratio are given in Table 6.3 and Fig 6.9. A comparison against the BREP model is not feasible, due to the large size of the domain. However, the value of the estimations confirm that the Torque-enabled Truss model remains stiffer than the traditional Truss model even for large domains.

(a) Number of elements   (b) Number of equations   (c) Solver allocated memory
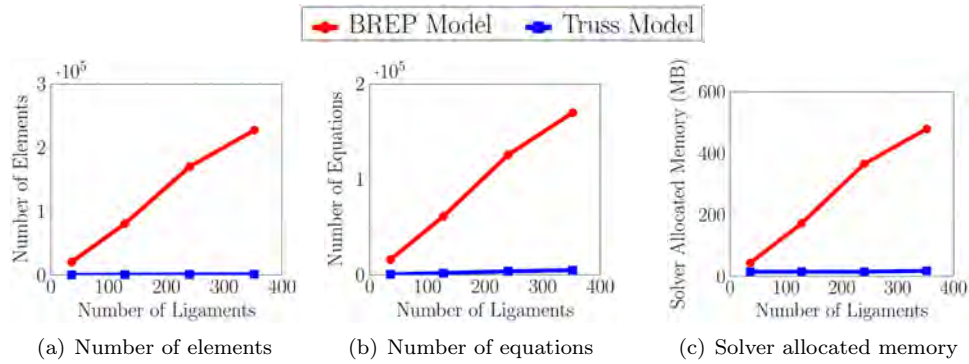
Figure 6.11: Comparison of the computational expenses of the BREP and Truss models.

6.7 Conclusions

In this paper we present a numerical procedure for estimating efficiently macro-mechanical properties of open-cell metal foams with rounded ligaments. We propose and implement a variation of the Truss model that considers torque at the ligament joints of the domain. The performance of this Torque-enabled Truss model is assessed with the estimation of the Young's modulus and Poisson's ratio for domains of 1, 4, 8, 12, and 100 Kelvin cells. The results obtained allow us to assert that the Torque-enabled Truss model (1) is an accurate and more efficient alternative for the computational representation of open-cell porous materials with rounded ligaments when compared with the BREP model, (2) is suitable to carry out estimations of the elastic properties of porous materials using numerical simulations, and (3) is stiffer and more accurate than the Torque-disabled Truss model when large domains are considered.

6.7.1 Future Work

The Kelvin cell considered in this article is isotropic (i.e., both geometric and lattice manufacturing conditions). On the other hand, in spite of geometrical symmetry, anisotropy may be also introduced by construction orientation (e.g. additive methods). This fact shows that anisotropy in lattice materials is a very extensive and complex research area, which we do not intend to undertake in the present work.

It was observed a trend of the Torque-enabled Truss model to become less stiff when the size of the domain increases. This effect may affect the performance of the proposed approach when compared to the BREP model. Therefore, a further analysis of this phenomenon is left as future work.

Chapter 7

Conclusions

This work presents a compilation of publications in applications of Computational Mechanics in which Computational Geometry and Numerical Simulation have a central role. Likewise, tools from mathematics, optimization, graph theory, and data structures and algorithms are fundamental for the developed approaches.

This compendium shows a method for structural optimization in which the material removal is based on the graph modeling of a FEA mesh. This material removal technique is integrated into Evolutionary Structural Optimization, one of the most used algorithms in topology optimization. This method assures the validity (from a structural point of view) of all the intermediate solutions and is well-suited to be used with a external software that performs the FEA calculations.

This document also contributes in the modeling and mechanical characterization of porous and lattice materials. Porous and lattice domains are modeled using 2.5D and 1.5D geometrical entities that can be converted into FEA elements of homologous dimensions. These geometrical simplifications reduce the time and memory expenses of the numerical simulations and allow the estimation of macro-mechanical properties (e.g. Young's modulus and Poisson's ratio) in a more efficient way. Comparisons between the BREP-based models and the geometrical simplified show differences of maximum 16% in the estimation of the Young's modulus for different domains.

Finally, the different contributions presented here can be further extended. Therefore, future research can be focused on: (1) the extension to 3D domains of our tool for topology optimization, (2) the modeling of geometrical and material anisotropy associated with the real porous domains, and (3) the validation through real tests of the numerical results for the estimation of mechanical properties of porous and lattice domains.

Bibliography

[1] MIEL1971. *Millau Viaduct*. 2015. Accessed August 30, 2018.

[2] Spatial Technology Inc. ACIS geometric modeler, 2017.

[3] J. A Hawreliak, J. Lind, B. Maddox, M. Barham, M. Messner, N. Barton, B. J. Jensen, and M. Kumar. Dynamic behavior of engineered lattice materials. *Scientific Reports*, 6:28094, 2016.

[4] Youming Chen, Raj Das, and Mark Battley. Finite element analysis of the compressive and shear responses of structural foams using computed tomography. *Composite Structures*, 159:784 – 799, 2017.

[5] E. Maire, F. Wattebled, J.Y. Buffire, and G. Peix. *Deformation of a Metallic Foam Studied by X-Ray Computed Tomography and Finite Element Calculations*, pages 68–73. Wiley-VCH Verlag GmbH & Co. KGaA, 2006.

[6] J. Nmeek, F. Denk, and P. Zlmal. Numerical modeling of aluminium foam on two scales. *Applied Mathematics and Computation*, 267:506 – 516, 2015. The Fourth European Seminar on Computing (ESCO 2014).

[7] M. Saadatfar, M. Mukherjee, M. Madadi, G.E. Schrder-Turk, F. Garcia-Moreno, F.M. Schaller, S. Hutzler, A.P. Sheppard, J. Banhart, and U. Ramamurty. Structure and deformation correlation of closed-cell aluminium foam subject to uniaxial compression. *Acta Materialia*, 60(8):3604 – 3615, 2012.

[8] Yongle Sun, Q.M. Li, T. Lowe, S.A. McDonald, and P.J. Withers. Investigation of strain-rate effect on the compressive behaviour of closed-cell aluminium foam by 3d image-based modelling. *Materials & Design*, 89:215 – 224, 2016.

[9] M.A. Kader, M.A. Islam, M. Saadatfar, P.J. Hazell, A.D. Brown, S. Ahmed, and J.P. Escobedo. Macro and micro collapse mechanisms of closed-cell aluminium foams during quasi-static compression. *Materials & Design*, 118:11 – 21, 2017.

[10] K. Natesaiyer, C. Chan, S. Sinha-Ray, D. Song, C. L. Lin, J. D. Miller, E. J. Garboczi, and A. M. Forster. X-ray CT imaging and finite element computations of the elastic properties of a rigid organic foam compared to experimental measurements: insights into foam variability. *Journal of Materials Science*, 50(11):4012–4024, Jun 2015.

[11] Shilong Wang, Yuanyuan Ding, Changfeng Wang, Zhijun Zheng, and Jilin Yu. Dynamic material parameters of closed-cell foams under high-velocity impact . *International Journal of Impact Engineering*, 99:111 – 121, 2017.

[12] C.Y. Zhang, L.Q. Tang, B. Yang, L. Zhang, X.Q. Huang, and D.N. Fang. Meso-mechanical study of collapse and fracture behaviors of closed-cell metallic foams . *Computational Materials Science*, 79:45 – 51, 2013.

[13] Xiaoyang Zhang, Liqun Tang, Zejia Liu, Zhenyu Jiang, Yiping Liu, and Yidong Wu. Yield properties of closed-cell aluminum foam under triaxial loadings by a 3D Voronoi model . *Mechanics of Materials*, 104:73 – 84, 2017.

[14] Youming Chen, Raj Das, and Mark Battley. Effects of cell size and cell wall thickness variations on the stiffness of closed-cell foams. *International Journal of Solids and Structures*, 52:150 – 164, 2015.

[15] C. Redenbach, I. Shklyar, and H. Andr. Laguerre tessellations for elastic stiffness simulations of closed foams with strongly varying cell sizes. *International Journal of Engineering Science*, 50(1):70 – 78, 2012.

[16] T. Wejrzanowski, J. Skibinski, J. Szumbarski, and K.J. Kurzydlowski. Structure of foams modeled by laguerrevoronoi tessellations. *Computational Materials Science*, 67:216 – 221, 2013.

[17] M. De Giorgi, A. Carofalo, V. Dattoma, R. Nobile, and F. Palano. Aluminium foams structural modelling . *Computers & Structures*, 88(1-2):25 – 35, 2010.

[18] S.K. Nammi, P. Myler, and G. Edwards. Finite element analysis of closed-cell aluminium foam under quasi-static loading . *Materials & Design*, 31(2):712 – 722, 2010.

[19] S.K. Nammi, G. Edwards, and H. Shirvani. Effect of cell-size on the energy absorption features of closed-cell aluminium foams . *Acta Astronautica*, 128:243 – 250, 2016.

[20] Yanze Song, Zhihua Wang, Longmao Zhao, and Jian Luo. Dynamic crushing behavior of 3D closed-cell foams based on Voronoi random model . *Materials & Design*, 31(9):4281 – 4289, 2010.

[21] Jian yu YUAN and Yan xiang LI. Effects of cell wall property on compressive performance of aluminum foams . *Transactions of Nonferrous Metals Society of China*, 25(5):1619 – 1625, 2015.

[22] R. Emre Erkmen. Multiple-point constraint applications for the finite element analysis of shear deformable composite beams variational multiscale approach to enforce full composite action. *Computers & Structures*, 149:17 – 30, 2015.

[23] R. Emre Erkmen, Mark A. Bradford, and Keith Crews. Variational multiscale approach to enforce perfect bond in multiple-point constraint applications when forming composite beams. *Computational Mechanics*, 49(5):617–628, May 2012.

[24] F.Y. Wang, Y.L. Xu, and W.L. Qu. Mixed-dimensional finite element coupling for structural multi-scale simulation. *Finite Elements in Analysis and Design*, 92:12 – 25, 2014.

[25] Cristian Guillermo Gebhardt and Raimund Rolfes. On the nonlinear dynamics of shell structures: Combining a mixed finite element formulation and a robust integration scheme. *Thin-Walled Structures*, 118:56 – 72, 2017.

[26] Kevin Weiler. The radial edge structure: a topological representation for non-manifold geometric boundary modeling. *Geometric modeling for CAD applications*, pages 3–36, 1988.

[27] Sang-Hun Lee and Kunwoo Lee. Partial Entity Structure: A Compact Boundary Representation for Non-Manifold Geometric Modeling. *J. Comput. Inf. Sci. Eng.*, 1(4):356–365, 2001.

[28] D. Canino, L. De Floriani, and K. Weiss. IA *: An adjacency-based representation for non-manifold simplicial shapes in arbitrary dimensions. *Computers and Graphics (Pergamon)*, 35(3):747–753, 2011. cited By 11.

[29] L. Zeng, Y.-J. Liu, S.H. Lee, and M.M.-F. Yuen. Q-Complex: Efficient non-manifold boundary representation with inclusion topology. *CAD Computer Aided Design*, 44(11):1115–1126, 2012. cited By 6.

[30] V. Dyedov, N. Ray, D. Einstein, X. Jiao, and T.J. Tautges. AHF: array-based half-facet data structure for mixed-dimensional and non-manifold meshes. *Engineering with Computers*, 31(3):389–404, 2015. cited By 0.

[31] Xinglin Zhao, Rebecca Conley, Navamita Ray, Vijay S. Mahadevan, and Xiangmin Jiao. Conformal and Non-conformal Adaptive Mesh Refinement with Hierarchical Array-based Half-Facet Data Structures. *Procedia Engineering*, 124:304 – 316, 2015.

[32] Consortium for Advanced Manufacturing International. Application interface specification (ais) 2.0, r-90-pm-03. Technical report, CAM-I, 1990.

[33] J. Han and A. A. G. Requicha. Modeler independent procedural interfaces for solid modeling. In *Proceedings Computer Graphics International*, pages 76–83, Washington, DC, USA, 1996. IEEE Computer Society. ISBN 0-8186-7518-7.

[34] C. Cortes, M. Osorno, D. Uribe, H. Steeb, O. Ruiz-Salguero, I. Barandiaran, and J. Florez. Geometry simplification of open-cell porous materials for elastic deformation fea. *Engineering with Computers*, pages 1–20, 2018.

[35] Michael D. Spivak. *Calculus On Manifolds: A Modern Approach To Classical Theorems Of Advanced Calculus*. Westview Press, 1971. ISBN-13: 978-0-8053-9021-6, ISBN: 0-8053-9021-9.

[36] Andrea Tagliasacchi, Thomas Delame, Michela Spagnuolo, Nina Amenta, and Alexandru Telea. 3D Skeletons: A State-of-the-Art Report. *Computer Graphics Forum*, 35(2):573–597, may 2016.

[37] Punam K. Saha, Gunilla Borgefors, and Gabriella Sanniti di Baja. A survey on skeletonization algorithms and their applications. *Pattern Recognition Letters*, 76:3–12, 2016.

[38] Tamal K Dey and Jian Sun. Defining and Computing Curve-skeletons with Medial Geodesic Function. *Eurographics Symposium on Geometry Processing*, 2006.

[39] Yu-Shuen Wang and Tong-Yee Lee. Curve-Skeleton Extraction Using Iterative Least Squares Optimization. *IEEE Transactions on Visualization and Computer Graphics*, 14(4):926–936, jul 2008.

[40] Steven J Ruuth and Brian T R Wetton. A Simple Scheme for Volume-Preserving Motion by Mean Curvature. *Journal of Scientific Computing*, 19(3), 2003.

[41] Xuetao Li, Wing Woon, Tiow Seng Tan, and Zhiyong Huang. Decomposing Polygon Meshes for Interactive Applications. *Symp. on Interactive 3D Graphics*, 2001.

[42] Chris Pudney. Distance-Ordered Homotopic Thinning: A Skeletonization Algorithm for 3D Digital Images. *Computer Vision and Image Understanding*, 72(3):404–413, dec 1998.

[43] Kálmán Palágyi and Attila Kuba. Directional 3D Thinning Using 8 Subiterations. *Proc. Discrete Geometry Comput. Imagery*, 1999.

[44] G. Malandain and G. Bertrand. Fast characterization of 3d simple points. In *Proceedings., 11th IAPR International Conference on Pattern Recognition. Vol. III. Conference C: Image, Speech and Signal Analysis,*, volume III, pages 232–235, Aug 1992.

[45] Gilles Bertrand and Grégoire Malandain. A new characterization of three-dimensional simple points. *Pattern Recognition Letters*, 15(2):169–175, feb 1994.

[46] Andrei C. Jalba, Andre Sobiecki, and Alexandru C. Telea. An Unified Multiscale Framework for Planar, Surface, and Curve Skeletonization. *IEEE Transactions on Pattern Analysis and Machine Intelligence*, 38(1):30–45, 2016.

[47] Kaleem Siddiqi, Sylvain Bouix, Allen Tannenbaum, and Steven W Zucker. The Hamilton-Jacobi Skeleton. *Int. J. Comput. Vis*, 48(3):pp. 215–231, 2002.

[48] Mauro Bracconi, Matteo Ambrosetti, Matteo Maestri, Gianpiero Groppi, and Enrico Tronconi. A systematic procedure for the virtual reconstruction of open-cell foams. *Chemical Engineering Journal*, 315:608–620, may 2017.

[49] Peter De Jaeger, Christophe T'Joen, Henk Huisseune, Bernd Ameel, and Michel De Paepe. An experimentally validated and parameterized periodic unit-cell reconstruction of open-cell foams. *Journal of Applied Physics*, 109(10):103519, 2011.

[50] Wen-Yea Jang, Stelios Kyriakides, and Andrew M. Kraynik. On the compressive strength of open-cell metal foams with kelvin and random cell structures. *International Journal of Solids and Structures*, 47(21):2872 – 2883, 2010.

[51] Claudia Lautensack. Fitting three-dimensional Laguerre tessellations to foam structures. *Journal of Applied Statistics*, 35(9):985–995, sep 2008.

[52] E.H. Saenger, D. Uribe, R. Jänicke, O. Ruiz, and H. Steeb. Digital material laboratory: Wave propagation effects in open-cell aluminium foams. *International Journal of Engineering Science*, 58:115 – 123, 2012.

[53] Paola Ranut, Enrico Nobile, and Lucia Mancini. High resolution X-ray microtomography-based CFD simulation for the characterization of flow permeability and effective thermal conductivity of aluminum metal foams. *Experimental Thermal and Fluid Science*, 67:30–36, oct 2015.

[54] N. Michailidis, F. Stergioudi, H. Omar, and D.N. Tsipas. An image-based reconstruction of the 3D geometry of an Al open-cell foam and FEM modeling of the material response. *Mechanics of Materials*, 42(2):142 – 147, 2010.

[55] Dorthe Wildenschild and Adrian P. Sheppard. X-ray imaging and analysis techniques for quantifying pore-scale structure and processes in subsurface porous medium systems. *Advances in Water Resources*, 51:217–246, jan 2013.

[56] William E. Lorensen and Harvey E. Cline. Marching Cubes: A high resolution 3d surface construction algorithm. *SIGGRAPH Comput. Graph.*, 21(4):163–169, August 1987.

[57] Andrea Tagliasacchi, Ibraheem Alhashim, Matt Olson, and Hao Zhang. Mean curvature skeletons. In *Computer Graphics Forum*, volume 31, pages 1735–1744. Wiley Online Library, 2012.

[58] László Neumann, Balázs Csébfalvi, Andreas König, and Eduard Gröller. Gradient Estimation in Volume Data using 4D Linear Regression. *Computer Graphics Forum*, 19(3):351–358, sep 2000.

[59] Calvin R. Maurer, Vijay Raghavan, and Rensheng Qi. A linear time algorithm for computing the euclidean distance transform in arbitrary dimensions. In Michael F. Insana and Richard M. Leahy, editors, *Information Processing in Medical Imaging*, pages 358–364, Berlin, Heidelberg, 2001. Springer Berlin Heidelberg.

[60] M. Saadatfar, C.H. Arns, M.A. Knackstedt, and T. Senden. Mechanical and transport properties of polymeric foams derived from 3d images. *Colloids and Surfaces A: Physicochemical and Engineering Aspects*, 263(1):284 – 289, 2005. A collection of papers presented at the 5th European Conference on Foams, Emulsions, and Applications, EUFOAM 2004, University of Marne-la-Vallee, Champs sur Marne (France), 5-8 July, 2004.

[61] I. Farmaga, P. Shmigelskyi, P. Spiewak, and L. Ciupinski. Evaluation of computational complexity of finite element analysis. In *2011 11th International Conference The Experience of Designing and Application of CAD Systems in Microelectronics (CADSM)*, pages 213–214, Feb 2011.

[62] Y.M. Xie and G.P. Steven. A simple evolutionary procedure for structural optimization. *Computers & Structures*, 49(5):885 – 896, 1993.

[63] O.M. Querin, G.P. Steven, and Y.M. Xie. Evolutionary structural optimisation (eso) using a bidirectional algorithm. *Engineering Computations*, 15(8):1031–1048, 1998.

[64] Kazem Ghabraie. An improved soft-kill beso algorithm for optimal distribution of single or multiple material phases. *Structural and Multidisciplinary Optimization*, 52(4):773–790, Oct 2015.

[65] David J. Munk, Gareth A. Vio, and Grant P. Steven. A Bi-directional Evolutionary Structural Optimisation algorithm with an added connectivity constraint. *Finite Elements in Analysis and Design*, 131:25 – 42, 2017.

[66] Joshua D. Deaton and Ramana V. Grandhi. A survey of structural and multidisciplinary continuum topology optimization: post 2000. *Structural and Multidisciplinary Optimization*, 49(1):1–38, Jan 2014.

[67] David J. Munk, Gareth A. Vio, and Grant P. Steven. Topology and shape optimization methods using evolutionary algorithms: a review. *Structural and Multidisciplinary Optimization*, 52(3):613–631, Sep 2015.

[68] Liang Xia, Qi Xia, Xiaodong Huang, and Yi Min Xie. Bi-directional Evolutionary Structural Optimization on Advanced Structures and Materials: A Comprehensive Review. *Archives of Computational Methods in Engineering*, Nov 2016.

[69] Raj Das and Rhys Jones. Topology optimisation of a bulkhead component used in aircrafts using an evolutionary algorithm. *Procedia Engineering*, 10:2867 – 2872, 2011. 11th International Conference on the Mechanical Behavior of Materials (ICM11).

[70] Yuhang Chen, Michiel Schellekens, Shiwei Zhou, Joseph Cadman, Wei Li, Richard Appleyard, and Qing Li. Design optimization of scaffold microstructures using wall shear stress criterion towards regulated flow-induced erosion. *Journal of Biomechanical Engineering*, 133(8):081008–448, 2011.

[71] X. Huang, Y. M. Xie, B. Jia, Q. Li, and S. W. Zhou. Evolutionary topology optimization of periodic composites for extremal magnetic permeability and electrical permittivity. *Structural and Multidisciplinary Optimization*, 46(3):385–398, Sep 2012.

[72] Junning Chen, Rohana Ahmad, Hanako Suenaga, Wei Li, Keiichi Sasaki, Michael Swain, and Qing Li. Shape Optimization for Additive Manufacturing of Removable Partial Dentures - A New Paradigm for Prosthetic CAD/CAM. *PLOS ONE*, 10(7):1–17, 07 2015.

[73] Y. Tang, G. Dong, Q. Zhou, and Y. F. Zhao. Lattice structure design and optimization with additive manufacturing constraints. *IEEE Transactions on Automation Science and Engineering*, PP(99):1–17, 2017.

[74] Daniel Stojanov, Brian G. Falzon, Xinhua Wu, and Wenyi Yan. Implementing a structural continuity constraint and a halting method for the topology optimization of energy absorbers. *Structural and Multidisciplinary Optimization*, 54(3):429–448, Sep 2016.

[75] Diego Montoya-Zapata, Diego A. Acosta, Oscar Ruiz-Salguero, and David Sanchez-Londono. Fea structural optimization based on metagraphs. In Manuel Graña, José Manuel López-Guede, Oier Etxaniz, Álvaro Herrero, José Antonio Sáez, Héctor Quintián, and Emilio Corchado, editors, *International Joint Conference SOCO'18-CISIS'18-ICEUTE'18*, pages 209–220, Cham, 2019. Springer International Publishing.

[76] M. Giger and P. Ermanni. Evolutionary truss topology optimization using a graph-based parameterization concept. *Structural and Multidisciplinary Optimization*, 32(4):313–326, 10 2006.

[77] J. F. Aguilar Madeira, H. L. Pina, and H. C. Rodrigues. GA topology optimization using random keys for tree encoding of structures. *Structural and Multidisciplinary Optimization*, 40(1):227, 02 2009.

[78] W.S. Hemp. *Optimum Structures (Oxford Engineering Science Series)*. Oxford University Press, 1973.

[79] Michael F. Ashby and Tianjian Lu. Metal foams: A survey. *Science in China Series B: Chemistry*, 46(6):521–532, 2003.

[80] Mustafa Guden, Emrah Celik, Sinan Cetiner, and Alptekin Aydin. *Metals Foams for Biomedical Applications: Processing and Mechanical Properties*, pages 257–266. Springer US, Boston, MA, 2004.

[81] H.X. Zhu, J.F. Knott, and N.J. Mills. Analysis of the elastic properties of open-cell foams with tetrakaidecahedral cells. *Journal of the Mechanics and Physics of Solids*, 45(3):319 – 343, 1997.

[82] Wen-Yea Jang, Andrew M. Kraynik, and Stelios Kyriakides. On the microstructure of open-cell foams and its effect on elastic properties. *International Journal of Solids and Structures*, 45(7-8):1845 – 1875, 2008.

[83] K Boomsma and D Poulikakos. On the effective thermal conductivity of a three-dimensionally structured fluid-saturated metal foam. *International Journal of Heat and Mass Transfer*, 44(4):827–836, 2001.

[84] L. Gong, S. Kyriakides, and W.-Y. Jang. Compressive response of open-cell foams. part i: Morphology and elastic properties. *International Journal of Solids and Structures*, 42(56):1355 – 1379, 2005.

[85] L. Gong and S. Kyriakides. Compressive response of open cell foams part ii: Initiation and evolution of crushing. *International Journal of Solids and Structures*, 42(56):1381 – 1399, 2005.

[86] Myriam Laroussi, Karam Sab, and Amina Alaoui. Foam mechanics: nonlinear response of an elastic 3d-periodic microstructure. *International Journal of Solids and Structures*, 39(1314):3599 – 3623, 2002.

[87] Zi-xing Lu, Qiang Liu, and Xin Chen. Analysis and simulation for tensile behavior of anisotropic open-cell elastic foams. *Applied Mathematics and Mechanics*, 35(11):1437–1446, 2014.

[88] Camilo Cortés, Maria Osorno, David Uribe, Holger Steeb, Oscar Ruiz-Salguero, Iñigo Barandiarán, and Julián Flórez. Geometry simplification of open-cell porous materials for elastic deformation fea. *Engineering with Computers*, Mar 2018.

[89] B. Buffel, F. Desplentere, K. Bracke, and I. Verpoest. Modelling open cell-foams based on the weairephelan unit cell with a minimal surface energy approach. *International Journal of Solids and Structures*, 51(1920):3461 – 3470, 2014.

[90] Claudia Lautensack and Tetyana Sych. 3D Image analysis of open foams using random tessellations. *Image Analysis & Stereology*, 25(2):87–93, 2011.

[91] Jaona Randrianalisoa, Dominique Baillis, Christophe L. Martin, and Rmy Dendievel. Microstructure effects on thermal conductivity of open-cell foams generated from the laguer-revorono tessellation method. *International Journal of Thermal Sciences*, 98:277 – 286, 2015.

[92] Matthew D. Montminy, Allen R. Tannenbaum, and Christopher W. Macosko. The 3d structure of real polymer foams. *Journal of Colloid and Interface Science*, 280(1):202 – 211, 2004.

[93] Youming Chen, Raj Das, and Mark Battley. Finite element analysis of the compressive and shear responses of structural foams using computed tomography. *Composite Structures*, 159:784 – 799, 2017.

[94] M Borovinšek, M Vesenjak, J Matela, and Z Ren. Computational reconstruction of scanned aluminum foams for virtual testing. *Journal of the Serbian Society for Computational Mechanics*, 2:16–28, 2008.

[95] ANSYS, Inc. *ANSYS Mechanical APDL Element Reference, Release 15.0*, 2013.

[96] M. F. Ashby, A. G. Evans, N. A. Fleck, L. J. Gibson, J. W. Hutchinson, and H. N. Wadley. *Metal foams: a design guide*. Butterworth-Heinemann, 2000.